



# Designing Novel Semiconductor Nanowire Structures: Synthesis and Fabrication for Localized Photodetection and Sensing

The Harvard community has made this article openly available. [Please share](#) how this access benefits you. Your story matters

Citation	Gao, Ruixuan. 2015. Designing Novel Semiconductor Nanowire Structures: Synthesis and Fabrication for Localized Photodetection and Sensing. Doctoral dissertation, Harvard University, Graduate School of Arts & Sciences.
Citable link	<a href="http://nrs.harvard.edu/urn-3:HUL.InstRepos:17463963">http://nrs.harvard.edu/urn-3:HUL.InstRepos:17463963</a>
Terms of Use	This article was downloaded from Harvard University's DASH repository, and is made available under the terms and conditions applicable to Other Posted Material, as set forth at <a href="http://nrs.harvard.edu/urn-3:HUL.InstRepos:dash.current.terms-of-use#LAA">http://nrs.harvard.edu/urn-3:HUL.InstRepos:dash.current.terms-of-use#LAA</a>

**Designing novel semiconductor nanowire structures:  
Synthesis and fabrication for localized photodetection and sensing**

A dissertation presented

by

**Ruixuan Gao**

to

The Department of Chemistry and Chemical Biology

in partial fulfillment of the requirements

for the degree of

**Doctor of Philosophy**

in the subject of

**Chemistry**

Harvard University

Cambridge, Massachusetts

January 2015

© 2015 by Ruixuan Gao  
All rights reserved.

**Designing novel semiconductor nanowire structures:  
Synthesis and fabrication for localized photodetection and sensing**

**Abstract**

Semiconductor nanowires display a wide range of structural and functional diversity, and as such provide a platform for nanomaterials research. At present, a number of nanowire structural motifs have been discovered and configured into devices with unique electrical and optical functionalities. For example, a kinked nanowire with a localized axial dopant modulation can record intracellular action potentials when incorporated into a three dimensional device. A radially modulated p-i-n nanowire can function as a nanoscale photovoltaic device to power logic gates and sensors. This thesis focuses on novel electrical and optical device functionalities based on rational design, synthesis and characterization of semiconductor nanowire structures for applications in the physical, chemical and biological sciences.

First, I will present the design, synthesis and fabrication of two nanodevices for intracellular sensing that are based on core/shell and branched nanowire structural motifs. In both types of devices, a nanotube bridge templated by nanowires conducts the intracellular electrical and chemical potentials to the gating regions and the change in potential is recorded as the change of the device conductance. Both nanowire-based devices can sense extra- and intracellular action potentials with high spatial resolution. Furthermore, they can be easily

multiplexed and scaled up to record intracellular action potentials at multiple sites from either a single cell or cellular network.

Second, I will discuss the synthesis of tapered nanowire structures and their electrical and optical characterization. By finely tuning growth temperature, precursor partial pressure, and catalyst size, detailed control of the nanowire tapering angle can be achieved. Moreover, tapered core/shell nanowires can be configured into devices with highly-localized electrical and optical functionalities. I show that control of the tapering angle plays an important role in determining the electrical and optical properties of nanowires.

Finally, I will demonstrate a novel nanowire structural motif, termed tip-modulated nanowire, in which the modulation of material and dopant is localized at the nanowire tip so that a tip-localized device is encoded. I describe rational bottom-up synthesis of tip-localized p-n junctions, which are connected to the p-type nanowire core and isolated n-type nanowire shell. The electrical and optical properties of the tip-modulated nanowires are investigated by configuring them as devices with electrically independent core and shell contacts. Spatially-resolved electrical and optical characterizations show that a potentiometric sensor as well as a highly sensitive p-n diode photodetector can be localized at the nanowire tip. In addition, a top-down strategy for wafer-scale synthesis and fabrication of vertical tip-modulated nanowires and nanowire device arrays is presented. Finally, by combining the tip-modulated nanowire structure with other structural motifs, we can rationally design self-sustained multi-functional nanodevices. The new tip-modulated nanowire structural motif opens up novel applications in the physical, chemical and biological sciences.

## **Acknowledgement**

I would like to first express my deepest gratitude to my advisor Professor Charles M. Lieber. Throughout the course of my PhD, Charlie has shaped me who I am as a scientist and a person. Charlie has always inspired me and taught me to be creative, persistent, diligent and above all scientific during the course of study. I could not be where I am without his guidance in these years.

I would like to thank all the faculties whom I had the honor to have in my committee: Professor Roy G. Gordon, Professor Daniel G. Nocera and Professor X. Sunney Xie. I am truly grateful to receive advice from them during the course of my PhD.

I would like to thank all the help from Kathleen Ledyard, Renee Donlon and Purvang Patel. Kathleen has been pivotal in running the group and has always been there for me. Renee offered great help and smile whenever I asked for assistance. Purvang has been a reliable source of help whenever I needed.

I am thankful to Professor Jeffery R. Long and Professor Eiichi Nakamura for their encouragement and support throughout my PhD. The Japan Student Services Organization graduate fellowship has greatly supported my graduate studies.

Bobby Day and Max Mankin are two great friends and collaborators. I would like to thank them for their friendship throughout the PhD. I was truly lucky to have them around during the course of my PhD.

Dr. You-Shin No is a great friend and collaborator. We have been working together since he joined the group and he has played tremendous role with his knowledge in nanophotonics and exceptional fabrication skills. I also would like to thank Dr. Hong-Gyu Park for all the invaluable advice.

Dr. Xiaojie Duan has been a great mentor and collaborator during the initial phase of my PhD. I learned the basic fabrication skills from her. Above all, she taught me how to tackle a difficult scientific issue and how to stay focused to get things done.

Dr. Steffen Strehle is a great scientist and collaborator from whom I learned a lot in many aspects of research. Ever since we met, he has offered great jokes and friendship.

Dr. Bozhi Tian has influenced me in so many aspects. He kindly offered help and precious advice throughout my PhD (which is impossible to list all) and has served a role model for me as a researcher.

Dr. Tzahi Cohen-Karni taught me many things ranging from the basics of cell culture to the maintenance of fabrication tools including the thermal evaporator. Tzahi is remembered for (not limited to): how to handle chicken embryos and his direct jokes, which left a strong impression to me during the initial days of my PhD.

Dr. Thomas Kempa has always inspired me as a scientist with his creativeness and diligence. He has helped me tremendously with nanowire synthesis and material characterization during the time we overlapped in the group. Above all, he and Tzahi offered great friendship ever since we met.

Dr. Jinlin Huang has been a great mentor and has always been there for instrumentation issues. Without Jinlin, the thermal evaporator system would have been a scrap: he was pivotal in the maintenance and troubleshooting of the tool. Together, we fixed and maintained the water cooling system, the compressor, the ion gauge and the electronics system. In a different aspect, Jinlin constantly challenged me with questions both related to and irrelevant to research. Although most of the time I could not give a satisfactory answer, I very much enjoyed the conversions and all the thinking behind.

I am indebted for all the senior members who offered their valuable advice and help: Dr. Quan Qing, Dr. Or Shemesh, Dr. Jun Yao, Dr. Hwang-Sung Choe, Dr. Xiaocheng Jiang, Dr. Hao Yan. I am grateful for Jia Liu, Zhe Jiang, Xiaochuan Dai and Tianming Fu, with whom I have shared most of the graduate days. I was also very fortunate to work with Dr. Wei Zhou, Dr. Ning Gao, Dr. Jae-Hyun Lee, Dr. Peter Kruskal, Dr. Lin Xu, Dr. Guosong Hong, Dr. Teng Gao, Tao Zhou, Sean Yu, Yunlong Zhao and the newest members of the group, Thomas Schumann, and Anqi Zhang. I would like to thank all the people I have worked with and met during my PhD.

Finally I would like to thank my parents. They have supported me much beyond words. I would also like to thank Clare for her charm and support.



# Table of Contents

<b>Acknowledgement .....</b>	<b>v</b>
<b>List of Abbreviations .....</b>	<b>xii</b>
<b>List of Figures.....</b>	<b>xiv</b>
<b>Chapter 1 Introduction.....</b>	<b>1</b>
1.1 Semiconductor nanowires: a platform for novel syntheses and applications.....	1
1.2 Electrical properties and applications of semiconductor nanowires .....	6
1.3 Optical properties and applications of semiconductor nanowires.....	12
1.4 Overview of thesis.....	17
1.5 Bibliography.....	19
<b>Part I Nanowire structures for intracellular sensing .....</b>	<b>22</b>
<b>Chapter 2 Branched nanowire field-effect transistors as nanoscale intracellular probes.....</b>	<b>22</b>
2.1 Introduction .....	22
2.2 Experimental .....	25
2.2.1 Synthesis of Si/Ge branched nanowires.....	25
2.2.2 Fabrication of branched intracellular nanotube field-effect transistors .....	27
2.2.3 Intracellular measurements of action potentials .....	28
2.3 Results and discussion.....	30
2.3.1 Nanowire synthesis and material characterizations .....	30
2.3.2 Electrical characterizations of the branched intracellular nanotube field-effect transistors .....	32

2.3.3 Intracellular recordings of action potentials with a single device.....	36
2.3.4 Multiplexed intracellular recordings of action potentials .....	40
2.4 Conclusion and outlook.....	43
2.5 Bibliography.....	44
<b>Chapter 3 Ge/Si core/shell nanowire-templated Si nanotube transistors as nanoscale intracellular probes .....</b>	<b>46</b>
3.1 Introduction .....	46
3.2 Experimental .....	49
3.2.1 Synthesis of Ge/Si core/shell nanowires.....	49
3.2.2 Fabrication of active silicon nanotube transistors.....	49
3.2.3 Intracellular measurements of action potentials .....	51
3.3 Results and discussion.....	53
3.3.1 Nanowire synthesis and material characterization.....	53
3.3.2 Electrical characterizations of the device .....	55
3.3.3 Intracellular recordings of action potentials with a single device.....	57
3.3.4 Nanotube size effect on the intracellular recordings.....	59
3.3.5 Multiplexed intracellular recordings of action potentials .....	60
3.4 Conclusion and outlook.....	64
3.5 Bibliography.....	65
<b>Part II Nanowire structures for localized optical and electrical device functionalities .....</b>	<b>67</b>
<b>Chapter 4 Tapered nanowire structures for localized field-effect transistors and light concentration.....</b>	<b>67</b>
4.1 Introduction .....	67

4.2 Experimental .....	69
4.2.1 Synthesis of tapered Ge, Si and core/shell nanowires .....	69
4.2.2 Fabrication of nanocone field-effect transistors .....	70
4.2.3 Electrical characterizations of nanocone field-effect transistors .....	71
4.2.4 Optical characterizations of tapered Ge/Ag core/shell nanowires .....	71
4.3 Results and discussion.....	72
4.3.1 Nanowire synthesis and material characterizations .....	72
4.3.2 Electrical properties of the nanocone field-effect transistors .....	81
4.3.3 Optical properties of tapered Ge/metal core/shell nanowires for guidance and concentration of light .....	83
4.4 Conclusion and outlook.....	85
4.5 Bibliography.....	86
<b>Chapter 5 Tip-modulated nanowire structures for localized electrical and optical functionalities.....</b>	<b>89</b>
5.1 Introduction .....	89
5.2 Experimental .....	91
5.2.1 Synthesis of tip-modulated Si p-n junction nanowires .....	91
5.2.2 Fabrication of tip-modulated nanowire devices.....	92
5.2.3 Generality of tip-modulated nanowire synthesis .....	92
5.2.4 Electrical and optical characterizations of tip-modulated nanowires .....	93
5.2.5 Top-down synthesis and fabrication of tip-modulated nanowires and device arrays .....	94
5.3 Results and discussion.....	96
5.3.1 Nanowire synthesis and material characterization.....	96

5.3.2 Electrical properties of the tip-modulated nanowires .....	100
5.3.3 Optical properties of the tip-modulated nanowires.....	105
5.3.4 Top-down synthesis and vertical nanowire sensor arrays.....	110
5.4 Conclusion and outlook.....	114
5.5 Bibliography.....	115
<b>Part III Nanowire structures for free-standing nanodevices.....</b>	<b>118</b>
<b>Chapter 6 Multi-terminal nanowire structures for self-powered, free-standing nanodevices .....</b>	<b>118</b>
6.1 Introduction .....	118
6.2 Experimental .....	121
6.2.1 Synthesis of two-terminal nanowires.....	121
6.2.2 Fabrication of two-terminal nanowire devices .....	123
6.2.3 Electrical and optical characterizations of two-terminal nanowire devices.....	124
6.3 Results and discussion.....	125
6.3.1 Nanowire synthesis and material characterizations .....	125
6.3.2 Electrical and optical properties of two-terminal nanowire devices.....	126
6.4 Conclusions and outlook .....	130
6.5 Bibliography.....	131

## List of Abbreviations

ALD: atomic layer deposition

ANTT: active nanotube transistor

BHF: buffered hydrofluoric acid

BIT-FET: branched intracellular nanotube field-effect transistor

BOE: buffered oxide etch

BW: bandwidth

CCD: charge-coupled device

CVD: chemical vapor deposition

CW: continuous wave

DAC: digital to analog convertor

DC: direct current

DIC: differential interference contrast

DRIE: deep reactive ion etching

EBL: electron beam lithography

EDS: energy dispersive spectrometry

FET: field-effect transistor

HRTEM: high resolution electron microscope

I-V: current-voltage

KNW: kinked nanowire

LED: light-emitting diode

MMA: methyl methacrylate

MOS-FET: metal-oxide-semiconductor field-effect transistor

PBS: phosphate buffered saline

PECVD: plasma-enhanced chemical vapor deposition

PMMA: polymethyl methacrylate

PVD: physical vapor deposition

RC: resistive-capacitive

S/D: source and drain

S/N: signal-to-noise

SAED: selected area electron diffraction

SEM: scanning electron microscope

TEM: transmission electron microscope

VLS: vapor-liquid-solid

# List of Figures

Figure 1.1 Binary phase diagram of Si and Au.....	3
Figure 1.2 Structural motifs of semiconductor nanowires.....	4
Figure 1.3 Novel structural motifs of semiconductor nanowires.....	5
Figure 1.4 Nanowires as field-effect transistors .....	6
Figure 1.5 Nanowires for programmable nanoelectronics.....	8
Figure 1.6 Nanowires for extracellular and intracellular sensing .....	10
Figure 1.7 Nanowires for waveguides and lasers .....	12
Figure 1.8 Nanowires for photovoltaics and photodetection .....	15
Table 1.1 Bioprobes for cellular sensing .....	19
Figure 2.1 Design and recording principle of branched intracellular nanotube transistors (BIT-FETs).....	24
Figure 2.2 Fabrication of BIT-FETs .....	26
Figure 2.3 SEM characterizations of BIT-FETs .....	31
Figure 2.4 Electrical characterizations of BIT-FETs.....	33
Figure 2.5 Temporal characterizations of BIT-FET gate response.....	35
Figure 2.6 Intracellular recording of action potentials with BIT-FETs .....	39
Figure 2.7 Multiplexed intracellular recording of action potentials from two BIT-FETs .....	41
Figure 2.8 Multiplexed intracellular recording of action potentials from cell networks .....	42
Figure 3.1 Design and recording principle of active nanotube transistors (ANTTs) .....	48
Figure 3.2 Fabrication of ANTTs .....	50
Figure 3.3 SEM and TEM characterizations of the Si nanotube templated by Ge/Si core/shell nanowires.....	54
Figure 3.4 Electrical characterizations of ANTTs .....	56
Figure 3.5 Intracellular recording of action potentials with ANTTs .....	58

Figure 3.6 Nanotube size effect on the intracellular recordings .....	60
Figure 3.7 Multiplexed intracellular recording of action potentials with ANTTs.....	62
Figure 4.1 Design and synthesis of tapered nanowires.....	73
Figure 4.2 Taper angle of Ge nanowires as function of catalyst size .....	74
Figure 4.3 Synthetic control and modulation of Ge nanowire taper angles.....	76
Figure 4.4 Synthetic control and modulation of Si <111> nanowire taper angles .....	78
Figure 4.5 Synthesis of tapered Ge/Si core/shell nanowires.....	80
Figure 4.6 Electrical characterizations of nanocone-FETs (NC-FETs).....	82
Figure 4.7 Synthesis and optical characterizations of tapered Ge/Ag core/shell nanowires .....	84
Figure 5.1 Synthesis of tip-modulated nanowires and material characterizations.....	97
Figure 5.2 Synthetic variations for the tip-modulated nanowire structure .....	99
Figure 5.3 High resolution transmission electron microscope (HRTEM) characterizations of the tip Si p-n junction .....	100
Figure 5.4 Fabrication of tip-modulated nanowire devices .....	101
Figure 5.5 Electrical characterizations of a tip-modulated nanowire device.....	103
Figure 5.6 Dark state semi-log (log(I)-V) plot of a tip-modulated nanowire device .....	104
Figure 5.7 Optical characterizations of a tip-modulated nanowire device .....	107
Figure 5.8 Localized light emission in tip-modulated nanowires with a tip p-Si/CdS heterojunction .....	109
Figure 5.9 Top-down synthesis and fabrication of vertical tip-modulated nanowires and nanowire device arrays.....	112
Figure 6.1 Free-standing, self-powered nanodevices .....	119
Figure 6.2 Multi-terminal nanowires for free-standing nanodevices.....	120
Figure 6.3 Rational synthesis of two-terminal nanowires .....	122
Figure 6.4 Synthesis and SEM characterizations of two-terminal nanowires .....	125
Figure 6.5 Electrical characterizations of two-terminal nanowires .....	127
Figure 6.6 Self-powered single-nanowire chemical sensors.....	129



# Chapter 1 Introduction

## 1.1 Semiconductor nanowires: a platform for novel syntheses and applications

Nanoscience, a branch of science that investigates nanoscale material and phenomenon, has expanded our understanding of how materials are constructed and function. For example, nanoscopic patterning can change macroscopic properties of a surface such as its hydrophobicity: with rational design of nanoscale surface patterns, superhydrophobic and self-cleaning surfaces can be created (3). In a different example, formation of alternating nanoscopic layers of semiconductors can generate a quantum confined system for various applications ranging from lasers to LEDs (4). Furthermore, nanoscale patterning of conductors and insulators has created a new group of materials, termed metamaterials, which display negative refractive indices and unique optical properties (5). Moreover, in recent years, extensive studies have been carried out for nanoscale materials (nanomaterials) of different dimensions, such as quantum dots (0-dimensional nanomaterials) (6), carbon nanotubes (1-dimensional nanomaterials) (7), and graphene (2-dimensional atomic crystals) (8).

Of all types of nanomaterials, nanowires have remained an important material platform in the nanoscience research. In particular, semiconductor nanowires, with their expanding structural complexity and functional diversity, have created a powerful platform for physical, chemical and biological sciences and applications (9). For instance, semiconductor nanowires have wide applications in electronics, such as high-performance field-effect transistors (10), logic gates (11), and nanoprocessors (12). Semiconductor nanowires have also shown great potential for optical

and optoelectrical applications including nanolasers (13), photodetectors (14), waveguides (15), solar cells (16) and LEDs (17).

In the pursuit of structural and functional complexity, rational synthesis of semiconductor nanowires has long been the interest of the field. Currently, there are two approaches to semiconductor nanowire synthesis: top-down and bottom-up. The top-down approach takes advantage of conventional semiconductor processing techniques such as lithography and etching processes. The bottom-up approach uses synthetic techniques of self-assembly and catalyzed growth, of which the most well-known example is the vapor-liquid-solid (VLS) growth of nanowires. In this thesis, nanowires are synthesized mostly with the bottom-up approach.

VLS growth takes advantage of different solubility of precursor materials in metal nanocatalysts. The Au-Si phase diagram (of the bulk materials) is shown in **Fig. 1.1**. When the equilibrium moves from the AuSi (l) to AuSi (l) + Si (s), Si precipitates and grows into a crystalline nanowire structure on one side of the catalyst. The subsequent elongation of the nanowire depends on the continuous supply of Si precursor to the system. Most commonly, chemical vapor deposition (CVD) is used for VLS nanowire growth. In this thesis, most of the bottom-up synthesis of nanowires is carried out in a CVD system using SiH<sub>4</sub>, GeH<sub>4</sub>, B<sub>2</sub>H<sub>6</sub> and PH<sub>3</sub> as the precursor gases. Depending on the growth conditions, such as the precursor partial pressure, flow rate and growth temperature, kinetics and thermodynamics of the nanowire growth can change. For example, when the precursor partial pressure and growth temperature are high, an uncatalyzed deposition mode in the radial direction becomes dominant due to the direct decomposition and

precipitation of precursor gas. In this thesis, most of the nanowire structures were synthesized by a combination of VLS and radial growth mechanisms.

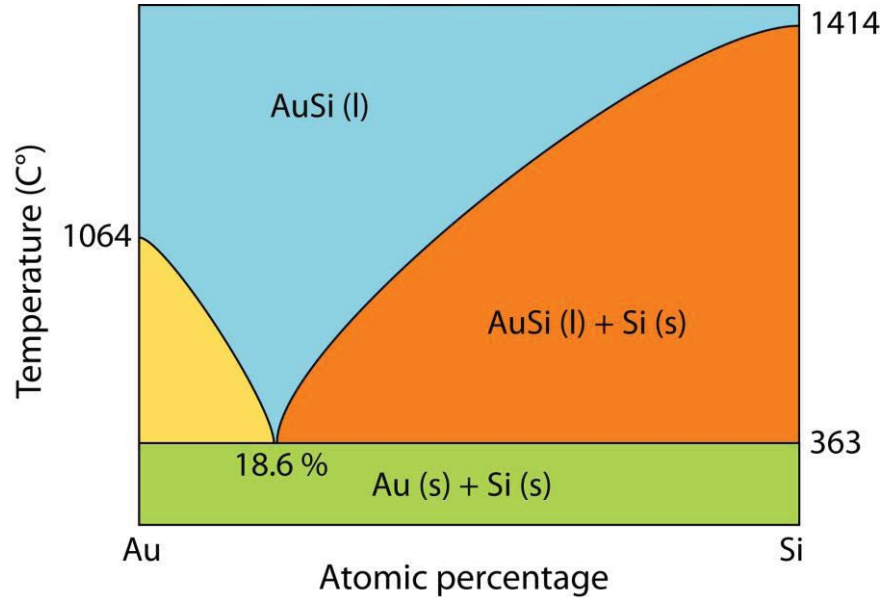


**Figure 1.1 Binary phase diagram of Si and Au.** Si nanowires can be synthesized bottom up by Au nanocluster catalyzed VLS growth.

Structural variations of nanowires have been extensively explored in the field to achieve complex nanostructures for unique electrical and optical functionalities. To date, a handful of structural motifs have been reported for nanowires: uniform, axially modulated, radially modulated, branched, and kinked nanowires (**Fig. 1.2**), with the axial and radial modulations being the two major structural motifs (9). The axially modulated nanowires, for example, localize a junction during the nanowire's axial elongation, in which the material composition or dopant profile is modulated along the nanowire axis. Near the axial junction, various device functionalities, such as that of a photodetector or of a potentiometer, can be localized. In the

radially modulated nanowires, on the other hand, the material composition or dopant profile is modulated concentrically around the nanowire axis and thus the junction extends through the whole nanowire. Therefore, radially modulated nanowires are suitable for applications that require a large junction area. For example, a p-i-n core/shell nanowire can be used as a highly-efficient photovoltaic device to power other nanoscale devices (16). The following sections discuss these structural motifs further in the context of their novel functionalities and applications.

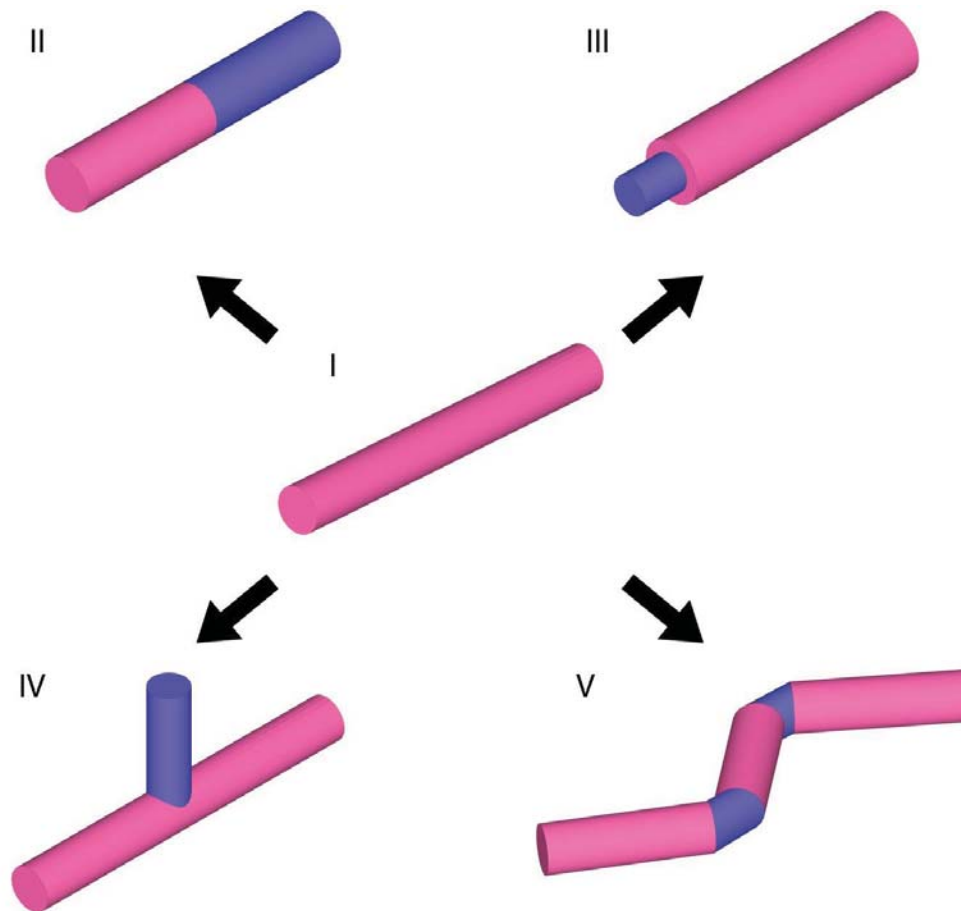


**Figure 1.2 Structural motifs of semiconductor nanowires.** (I) Uniform nanowires; (II) axial nanowires; (III) radial or core/shell nanowires; (IV) branched nanowires; (V) kinked nanowires.

This thesis is focused mainly on two topics: (1) development of novel functionalities using conventional nanowire structural motifs and (2) design and rational synthesis of novel nanowire structure motifs. In particular, I show that the branched and core/shell nanowire structures can be configured into three-dimensional field-effect transistor (FET) devices and be used as intracellular probes to detect electrical and chemical signals. I also present that through rational design novel nanowire structural motifs, such as the tapered and tip-modulated nanowires (**Fig. 1.3**), can be synthesized and configured into nanodevices. Notably, these new nanowire structures and devices show unique electrical and optical functionalities for a wide range of applications in physics, chemistry and biology.

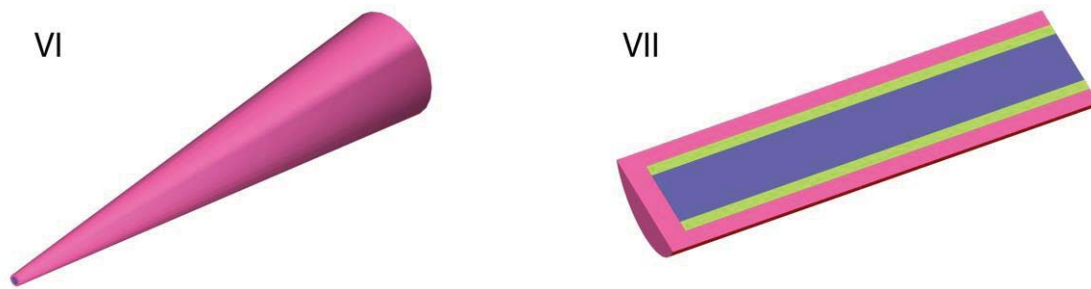


**Figure 1.3 Novel structural motifs of semiconductor nanowires.** (VI) Tapered nanowires; (VII) tip-modulated nanowires (the nanowire is half-cut along the axis).

## 1.2 Electrical properties and applications of semiconductor nanowires

Nanowires can be fabricated into electrical devices by, for example, defining two metal contacts as source/drain contacts and depositing oxide layers as the gate insulation layer (10, 18). For instance, the channel between the two contacts functions as a p-type FET when the source/drain contacts are defined on a uniformly doped p-type Si nanowire. **Fig. 1.4** shows typical I-V characteristics and gate responses (back-gate) of a p-type Si nanowire FET device. The I-V curve of the nanowire device shows a linear relationship, suggesting that the metal contacts and the semiconductor nanowire have formed an ohmic contact. The back-gate experiment shows that the conductance (or the resistivity) of the nanowire depends on the ambient electrical potential. Taken together, the p-type nanowire device serves as a FET device that can detect the ambient electrical potential change.

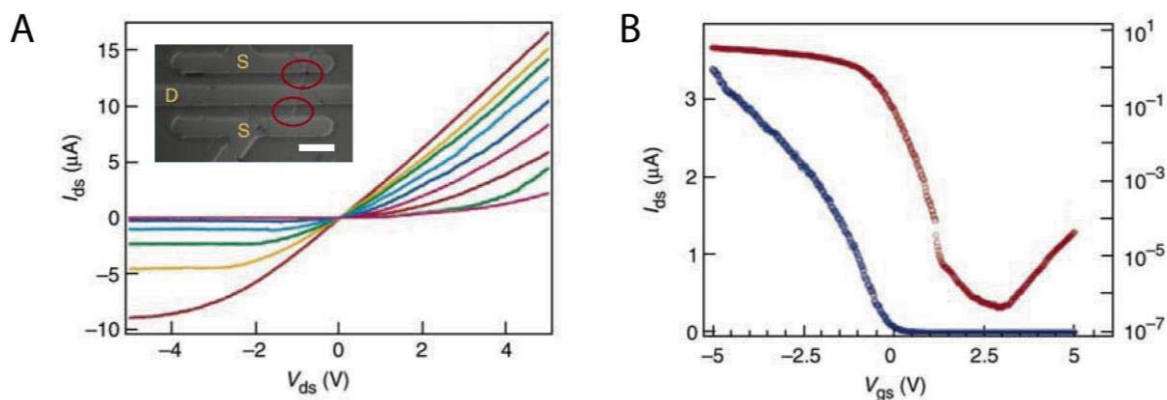


**Figure 1.4 Nanowires as field-effect transistors.** (A) I-V curve of a p-type Si nanowire FET device. Family of source-drain current ( $I_{ds}$ ) vs. source-drain voltage ( $V_{ds}$ ) were recorded at different back-gate voltages ( $V_g$ ) for a typical p-type Si nanowire FET. The red, orange, green, cyan, blue, magenta, red, green and magenta curves correspond to gate voltage values of  $-5$ ,  $-4$ ,  $-3$ ,  $-2$ ,  $-1$ ,  $0$ ,  $1$ ,  $2$ , and  $3$  V, respectively. Inset, SEM image of typical Si nanowire FET devices

**Figure 1.4 (Continued):** with source and drain (S/D) contacts defined by photolithography. The red circles indicate the two devices defined on the same nanowire. Scale bar, 4.5  $\mu\text{m}$ . Adapted from reference (18). **(B)**  $I_{\text{ds}}$  vs.  $V_{\text{g}}$  recorded for the same p-type Si nanowire FET device plotted on linear (blue) and logarithmic (red) scales at a  $V_{\text{ds}}$  of 1 V. Adapted from reference (18).

By combining nanowire FET devices with switchable gate nodes, more complex nanocircuits can be fabricated to achieve higher level of functionalities (**Fig. 1.5A**). For instance, nanowire FETs can be used as building blocks to create a nanoprocessor that function as, for example, a full adder and a multiplexer (**Fig. 1.5B-E**) (11).

Furthermore, nanowire FETs can be gated in biological environments such as extracellular and intracellular mediums. When a p-type nanowire FET is submerged in electrolyte, the FET device shows gate response to the voltage applied to the electrolyte through a reference electrode (**Fig. 1.6A**) (18). This gating phenomenon is conventionally called the “water-gate” as the electrolyte (or the “water”) serves as the top-gate similar to that in the traditional metal-oxide-semiconductor field-effect transistors (MOS-FETs).

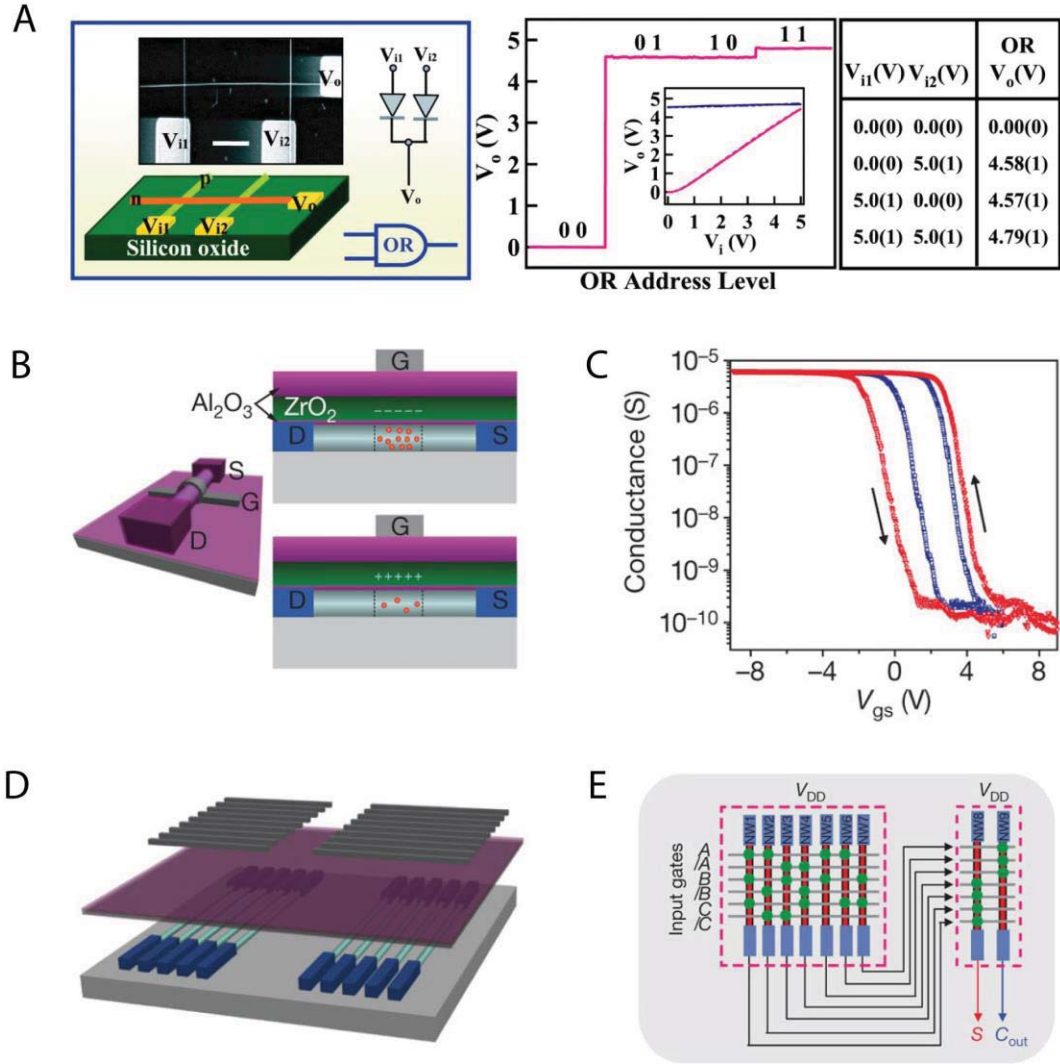


**Figure 1.5 Nanowires for programmable nanoelectronics.** (A) Schematic illustration of nanowire nano-logic gates. Output voltage ( $V_o$ ) of logic OR gate is constructed from a 2 (p-type) by 1 (n-type) crossed nanowire p-n junction. Inset, SEM image of the assembled “OR” gate and symbolic electronic circuit. Scale bar, 1  $\mu\text{m}$ . Adapted from reference (11). (B-E) Programmable nanowire circuits. Adapted from reference (12). (B) Schematic illustration of a Ge/Si nanowire FET device with a programmable top-gate (left). S, D and G correspond to source, drain and gate, respectively. Representative hole concentration in a p-type Ge/Si nanowire FET for two charge-trapping states illustrates carrier accumulation for a negative trapped charge (top right) and



**Figure 1.5 (Continued):** depletion for a positive trapped charge (bottom right) in the  $\text{ZrO}_2$  layer. (C) Semi-logarithmic plot of conductance vs. gate voltage ( $V_{\text{gs}}$ ) for the top-gated Ge/Si nanowire FET device recorded for  $\pm 6$  V (blue) and  $\pm 9$  V (red) sweeps at  $V_{\text{ds}} = 0.5$  V; arrows represent sweep/hysteresis direction. (D) Schematic illustration of key components of the two programmable and non-volatile nanowire transistor array block tiles, including assembled and patterned Ge/Si nanowires (cyan) with source and drain electrodes (blue), and charge-trapping trilayer gate dielectric (purple) and metal gate lines (grey). The fabricated structure consists of two blocks of nanowire FETs, block 1 (left) and block 2 (right). (E) Circuit design implementing a one-bit full adder. /A, /B and /C denote the complementary inputs of A, B and C, respectively. The left- and right-hand dashed boxes outline block 1 and block 2, respectively.

When a biological cell is in proximity of the nanowire FET, the change in membrane voltage can gate the device. In particular, cultured cardiomyocytes, which show periodic action potentials, can gate nanowire FET arrays on a substrate when they are brought into proximity (**Fig. 1.6B and C**) (19). When the nanowire FET devices are configured into a three-dimensional device, the gating area can protrude into a biological cell and record intracellular action potentials. A kinked nanowire (KNW), for instance, with the gating region encoded near the kink by axial dopant modulations, can be fabricated into a three-dimensional configuration by bending-up the metal/resist support (**Fig. 1.6D and E**) (20). Consequently, the kinked nanowire FET (KNW-FET) devices can protrude into a cell and record intracellular action potentials (**Fig. 1.6F**).

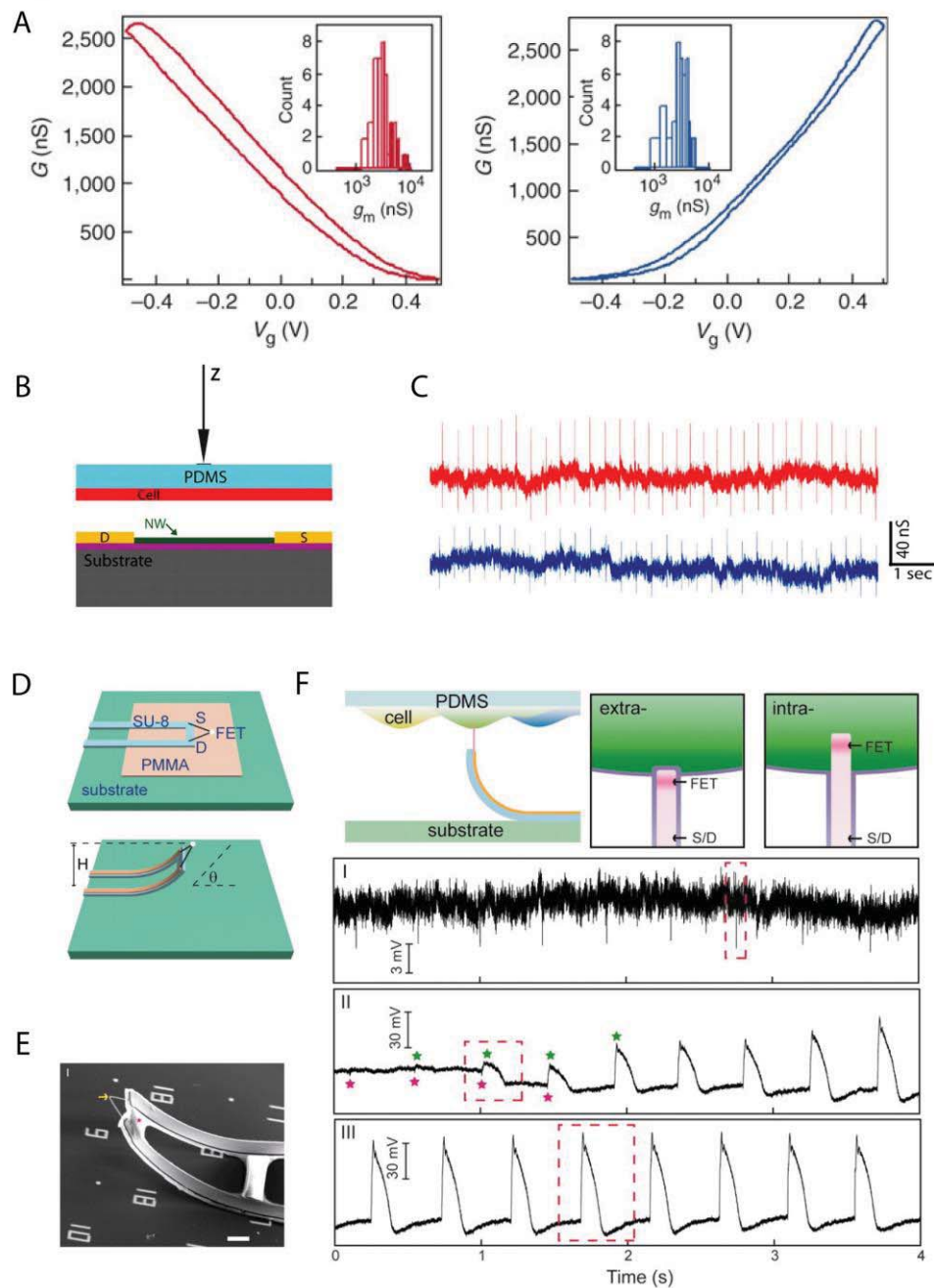


**Figure 1.6 Nanowires for extracellular and intracellular sensing.** (A) Water-gate transconductance of p-type (left) and n-type (right) nanowire FET devices. Insets, histogram of transconductance values of more than 50 p-type or n-type devices. Adapted from reference (18). (B, C) Extracellular action potential recordings from cardiomyocytes with nanowire FET devices.

**Figure 1.6 (Continued):** Adapted from reference (19). **(B)** Schematic illustration of the measurement with displacement ( $Z$ ) of the polydimethylsiloxane (PDMS)/cardiomyocytes substrate with respect to a nanowire FET device; PDMS displacement is accomplished with micromanipulator-controlled glass pipette. **(C)** Two representative traces recorded with  $\Delta Z$  values of 8.2  $\mu\text{m}$  (blue) and 18.0  $\mu\text{m}$  (red) yield signal amplitudes of  $44 \pm 3$  and  $72 \pm 4$  nS, respectively. The same device was used to record both traces. **(D-F)** Intracellular action potential recordings from cardiomyocytes with bent-up kinked nanowire FET (KNW-FET) devices. Adapted from reference (20). **(D)** Schematic illustration of device fabrication. Patterned polymethyl methacrylate (PMMA) and SU-8 microribbons serve as a sacrificial layer and flexible device support, respectively. The dimensions of the lightly doped n-type silicon segment (white dots) are  $\sim 80$  by  $80$  by  $200$  nm<sup>3</sup>.  $H$  and  $\theta$  are the tip height and orientation, respectively, and  $S$  and  $D$  designate the source and drain connections to the nanoscale FET. **(E)** SEM images of an as-fabricated device. The yellow arrow and pink star denote the nanoscale FET and SU-8. Scale bar, 5  $\mu\text{m}$ . **(F)** Top: schematic illustration of cellular recording from the cardiomyocyte monolayer on PDMS (left) and highlight of extracellular (middle) and intracellular (right) nanowire/cell interfaces. The cell membrane and nanowire lipid coatings are marked with purple lines. Bottom: electrical recording from beating cardiomyocytes: (I) extracellular recording, (II) transition from extracellular to intracellular recordings during cellular entrance, and (III) steady-state intracellular recording. Green and pink stars denote the peak positions of intracellular and extracellular signal components, respectively.

### 1.3 Optical properties and applications of semiconductor nanowires

Synthetic control of semiconductor nanowires has enabled diverse optical and optoelectrical functionalities to be encoded in the nanowire structure. For example, researchers have found that nanowires can serve as a low-loss, highly efficient waveguide for nano-optoelectronic circuits (Fig. 1.7A-C) (15). Moreover, nanowires are able to support optical modes and to display a strong lasing effect and function as nanoscale lasers (Fig. 1.7D and E) (13).

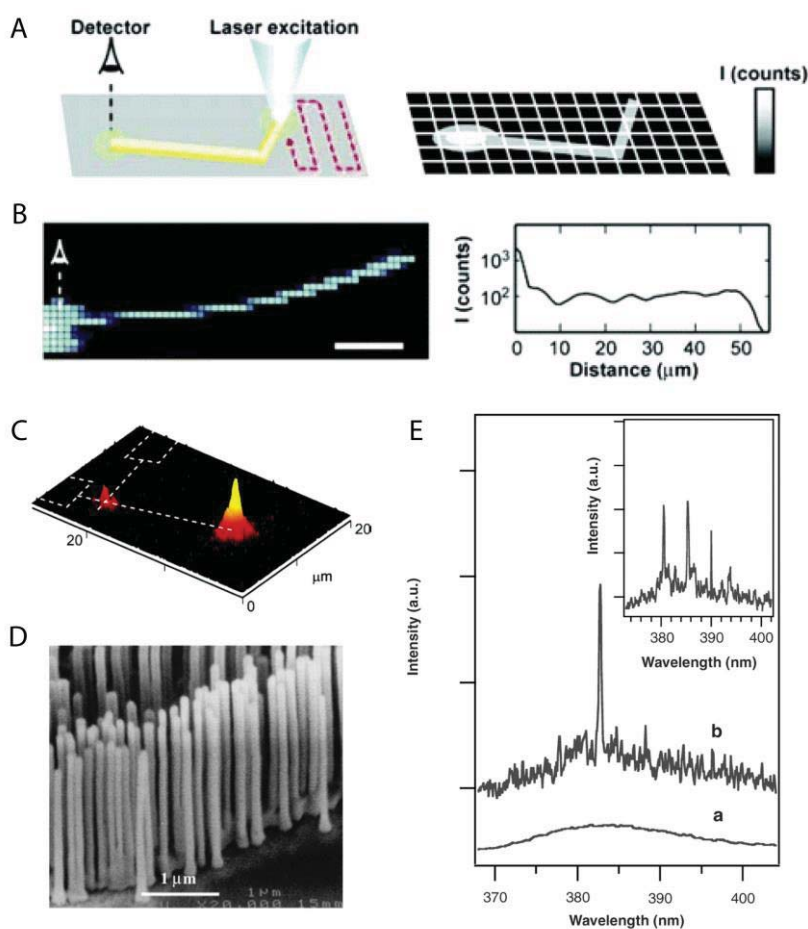


**Figure 1.7 Nanowires for waveguides and lasers.** (A-C) Optical waveguiding in semiconductor nanowires. Adapted from reference (15). (A) Schematics illustration of scanning

**Figure 1.7 (Continued):** optical microscopy as a focused laser spot is scanned over the sample while monitoring light emission from one end of the nanowire. The intensity at the end indicated by the detector is plotted on a color scale as a function of laser position to generate scanning optical microscopy images. **(B)** Scanning optical microscopy image of a single CdS nanowire (left) and the dependence of the end intensity on the distance between the laser spot and the end of the wire for a path that follows the wire (right). The reference end is indicated with detector. Lighter colors correspond to greater end intensity. Scale bar, 10  $\mu\text{m}$ . **(C)** Electrical injection of light into nanowire waveguides. Intensity map of a light-emitting diode made by assembling one n-type CdS nanowire and one p-type Si nanowire in a crossed geometry. The white dashed lines highlight the positions of the CdS ( $\sim$ horizontal) and Si ( $\sim$ vertical) nanowires. The image was recorded with a forward bias of 11 V. Titanium metal electrodes were used to contact both nanowires. **(D, E)** ZnO nanowires for ultraviolet nanolasers. Adapted from reference (13). **(D)** SEM images of ZnO nanowire arrays grown on sapphire substrates. Scale bar, 1  $\mu\text{m}$ . **(E)** Emission spectra from nanowire arrays below (a) and above (b and inset) the lasing threshold. The pump power for these spectra are 20, 100, and 150  $\text{kW}/\text{cm}^2$ , respectively.

For another example, semiconductor nanowires with a p-n junction can function as a photodiode for photodetection and power generation. For example, a p-i-n axially modulated Si nanowire can be used as an avalanche photodiode for high-performance photodetection (14). In addition, a core/shell p-n junction Si nanowire can be configured as a nano-scale solar generator and serve as a nanoscale power-supply to operate other nanodevices on the same chip (**Fig. 1.8A-D**) (16, 21). All these optical devices can achieve high external quantum efficiency due into the light-concentration to the high-refractive index nanostructure, making nanowires an advantageous platform for optical applications compared with conventional planar structures.

Notably, the optical property of the nanowire heavily depends on the morphology of the nanowire structure (crystallinity, doping profiles, diameters, shapes of cross-section, etc.). Tuning crystallinity and doping profiles, for instance, can improve efficiency of a nanowire-based solar cell. The cross-sectional dimension and shape also strongly influence the absorption spectra of the nanowire optical devices and thus can be exploited to enhance or generate new optical functionalities (**Fig. 1.8E**) (22).

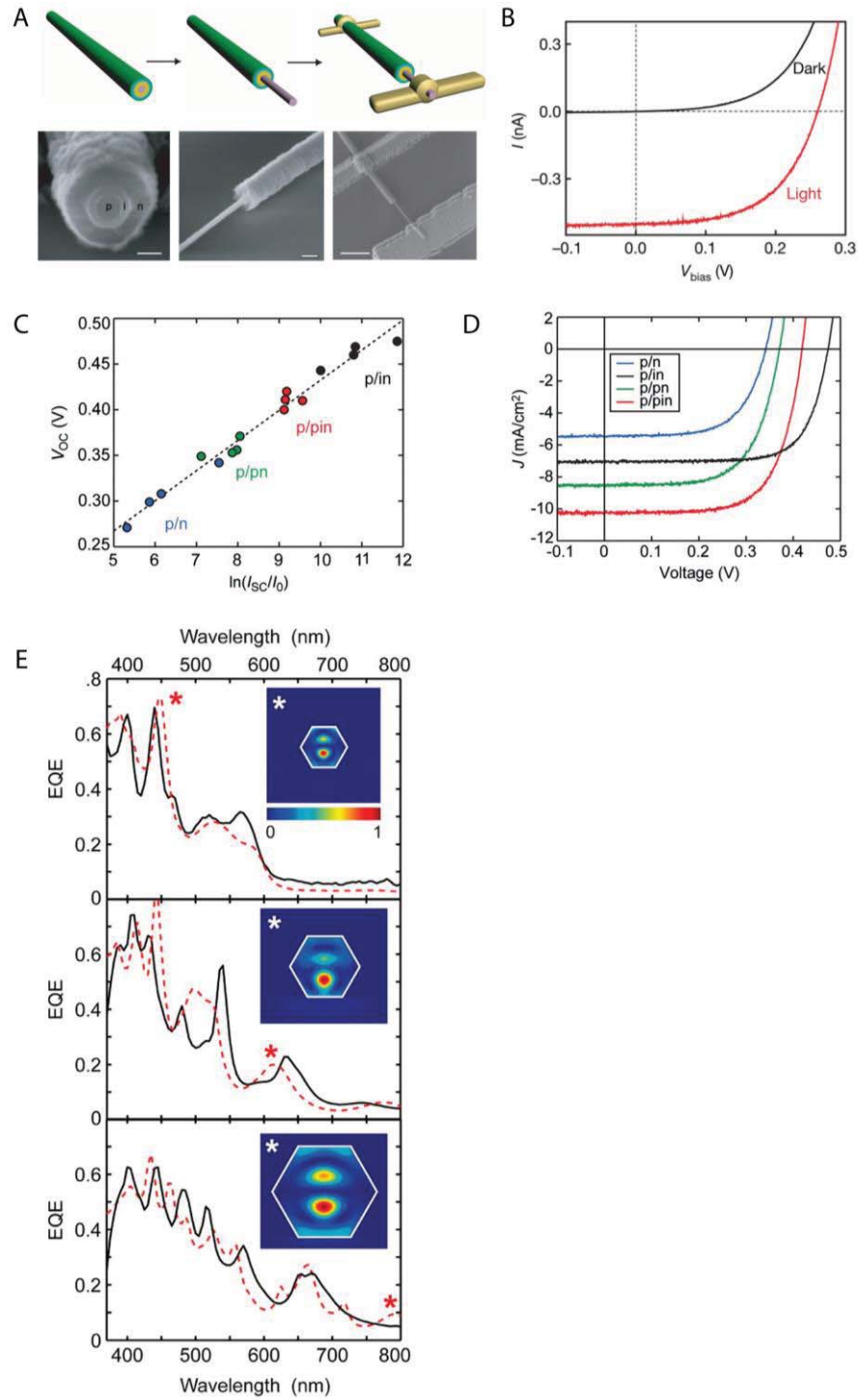


**Figure 1.8 Nanowires for photovoltaics and photodetection.** (A) Top: schematic illustration of device fabrication of a radially modulated p-i-n nanowire photovoltaic device. Pink, yellow, cyan

**Figure 1.8 (Continued):** and green layers correspond to the p-core, i-shell, n-shell and PECVD-coated  $\text{SiO}_2$ , respectively. Metal contacts are deposited on the p-core and n-shell. Bottom, SEM images of device. Scale bars are 100 nm (left), 200 nm (middle) and 1.5  $\mu\text{m}$  (right). Adapted from reference (16). **(B)** Dark and light I-V curves of a radially modulated p-i-n nanowire photovoltaic device. Adapted from reference (16). **(C)** Open-circuit voltage ( $V_{oc}$ ) vs. the logarithm of the ratio of short-circuit current ( $I_{sc}$ ) to dark saturation current ( $I_0$ ) for the four best devices from each diode geometry. Adapted from reference (21). **(D)** Current density-voltage (J-V) characteristics of single-nanowire solar cells composed of four distinct diode geometries. Adapted from reference (21). **(E)** Size-dependent properties of hexagonal radially modulated p-i-n Si nanowires. Experimental (solid black) and simulated (dashed red) external quantum efficiency spectra for nanowires with diameters of 170 (top), 280 (middle), and 380 nm (bottom). Insets: normalized Fabry–Perot absorption mode profiles calculated by 3-D finite element domain simulations for a hexagonal nanowire of the corresponding diameter. These modes correspond to the peaks marked by an asterisk. Adapted from reference (22).



## 1.4 Overview of thesis

In what follows in this thesis, Chapters 2 and 3 are focused on the branched and core/shell nanowire structural motifs and their applications for intracellular probes. More specifically, in Chapter 2, I discuss the rational design and synthesis of branched Si/Ge nanowires and the subsequent fabrication into three-dimensional intracellular probes, which can function as in-cell electrical and chemical sensors. In Chapter 3, I present the rational design and synthesis of Ge/Si core/shell nanowires and fabrication of intracellular probes based on the core/shell nanowire structure. Taking advantage of the conductance of the nanofluidic channel between the cell and active transistor region, the fabricated intracellular probes can record intracellular electrical and chemical signals.



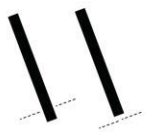
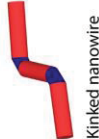
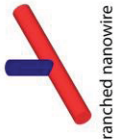
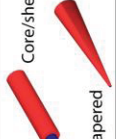

In Chapters 4 and 5, I explore design and synthesis of two novel nanowire structural motifs, tapered and tip-modulated nanowires. Chapter 4, in particular, describes how to finely tune and modulate nanowire tapering by varying synthetic conditions such as growth temperature and precursor partial pressure. Using tapered nanowires as template, I show that a tapered Ge/Si core/shell nanowires can be configured into a localized FET device with high temporal resolutions. I also show that a tapered Ge/Ag core/shell nanowire can waveguide and concentrate light to the nanowire tip. In Chapter 5, I present the design, synthesis and characterization of a tip-modulated nanowire structure, in which the material compositions or dopant profiles are modulated only at the nanowire tip. I show that the tip-modulated nanowires can be used as localized potentiometer and photodetector. Moreover, the general structure of tip-modulated

nanowires can be expanded to tip-heterojunction, which can function as localized LED. Finally, I present a large-scale synthesis based on the top-down approach.

To conclude this thesis, in Chapter 6, I introduce a new nanowire structure which can function as a free-standing and self-powered nanodevice. To this end, I present some preliminary results for the synthesis as well as for the electrical and optical characterizations.

A detailed comparison between conventional cellular recording techniques and nanowire-based bioprobes is shown in **Table 1.1** (1, 2). While patchclamp techniques and multi-electrode arrays allow for reliable intracellular and extracellular sensing, nanowire-based bioprobes show advantages in a number of aspects such as the small tip size, easy scale-up for multiplexed recording, and multi-functionality. In addition, represented by the KW-FET, BIT-FET, ANTT and the tip-modulated nanowire structures, the structural diversity of nanowires enables design and fabrication of different device geometries for different biological systems. Moreover, the novel bio-mimetic cell-entrance mechanism demonstrated by the nanowire-based probes makes them an attractive candidate for long-term and non-invasive recordings. However, future works still remain in, for example, long-term (chronic) recordings, device multifunctionality for simultaneous electrical and optical recording and simulation, further scale-up of fabrication for multiplexed recordings and three-dimensional incorporation in tissues.

**Table 1.1 Bioprobes for cellular sensing.** Part of the table adapted from references (1, 2).

Bioprobes	Size (nm)	Calibrations	Invasiveness	Cellular Entrance	Duration of stable recording	Capabilities
Glass micropipette (patchclamp)	 ~1000-5000	Amplitude and Shape	Electrochemical and mechanical	Mechanical	hours	Can record both current and voltage; challenging for multiplexed recording
Sharp glass micropipette (intracellular glass microelectrode)	 ~50-100	Amplitude and Shape	Electrochemical and mechanical	Mechanical	hours	Small tip size for insertion; challenging for multiplexed recording
Metal/carbon micro-(nano-) electrode	 ~100-1000 (limited by impedance)	Amplitude and Shape	Electrochemical and mechanical	Mechanical or electrical	mins-hours	Can record both current and voltage; multiplexed recording
Kinked nanowire field-effect transistor (KNW-FET)	 ~10-100	Amplitude	Minimal	Biological (phospholipid)	mins (research on-going for long term recording)	Can record voltage; multiplexed recording; high spatiotemporal resolution
Branched intracellular nanotube field-effect transistor (BIT-FET) Chapter 2	 ~10-100	Amplitude	Minimal	Biological (phospholipid)	mins-1h (research on-going for long term recording)	Can record voltage; multiplexed recording; high spatiotemporal resolution
Active nanotube field-effect transistor (ANTT) Chapter 3 & 4	 ~30-100	Amplitude	Minimal	Biological (phospholipid)	mins (research on-going for long term recording)	Can record voltage; multiplexed recording; high spatiotemporal resolution
Tip-modulated nanowire Chapter 5	 ~100-200 (can be further reduced)	Amplitude	NA	NA	NA	Can record voltage; multiplexed recording; high spatiotemporal resolution; multi-functional probetip (potentiometer, photodetector, photovoltaic, etc.)

## 1.5 Bibliography

1. B. Tian, C. M. Lieber, Synthetic nanoelectronic probes for biological cells and tissues. *Annu. Rev. Anal. Chem.* **6**, 31-51 (2013).
2. M. E. Spira, A. Hai, Multi-electrode array technologies for neuroscience and cardiology. *Nat. Nanotechnol.* **8**, 83-94 (2013).
3. T. S. Wong, S. H. Kang, S. K. Y. Tang, E. J. Smythe, B. D. Hatton, A. Grinthal, J. Aizenberg, Bioinspired self-repairing slippery surfaces with pressure-stable omniphobicity. *Nature* **477**, 443-447 (2011).
4. S. Nakamura, M. Senoh, S. Nagahama, N. Iwasa, T. Yamada, T. Matsushita, H. Kiyoku, Y. Sugimoto, Ingan-based multi-quantum-well-structure laser diodes. *Jpn. J. Appl. Phys.* **2**, **35**, L74-L76 (1996).
5. D. R. Smith, J. B. Pendry, M. C. Wiltshire, Metamaterials and negative refractive index. *Science* **305**, 788-792 (2004).
6. I. L. Medintz, H. T. Uyeda, E. R. Goldman, H. Mattoussi, Quantum dot bioconjugates for imaging, labelling and sensing. *Nat. Mater.* **4**, 435-446 (2005).
7. M. Terrones, Science and technology of the twenty-first century: Synthesis, properties and applications of carbon nanotubes. *Annu. Rev. Mater. Res.* **33**, 419-501 (2003).
8. A. K. Geim, K. S. Novoselov, The rise of graphene. *Nat. Mater.* **6**, 183-191 (2007).
9. C. M. Lieber, Semiconductor nanowires: A platform for nanoscience and nanotechnology. *MRS Bulletin* **36**, 1052-1063 (2011).
10. Y. Cui, Z. Zhong, D. Wang, W. U. Wang, C. M. Lieber, High performance silicon nanowire field effect transistors. *Nano Lett.* **3**, 149-152 (2003).
11. Y. Huang, X. Duan, Y. Cui, L. J. Lauhon, K. H. Kim, C. M. Lieber, Logic gates and computation from assembled nanowire building blocks. *Science* **294**, 1313-1317 (2001).
12. H. Yan, H. S. Choe, S. Nam, Y. Hu, S. Das, J. F. Klemic, J. C. Ellenbogen, C. M. Lieber, Programmable nanowire circuits for nanoprocessors. *Nature* **470**, 240-244 (2011).
13. M. H. Huang, S. Mao, H. Feick, H. Yan, Y. Wu, H. Kind, E. Weber, R. Russo, P. Yang, Room-temperature ultraviolet nanowire nanolasers. *Science* **292**, 1897-1899 (2001).
14. C. Yang, C. J. Barrelet, F. Capasso, C. M. Lieber, Single p-type/intrinsic/n-type silicon nanowires as nanoscale avalanche photodetectors. *Nano Lett.* **6**, 2929-2934 (2006).

15. C. J. Barrelet, A. B. Greytak, C. M. Lieber, Nanowire photonic circuit elements. *Nano Lett.* **4**, 1981-1985 (2004).
16. B. Z. Tian, X. L. Zheng, T. J. Kempa, Y. Fang, N. F. Yu, G. H. Yu, J. L. Huang, C. M. Lieber, Coaxial silicon nanowires as solar cells and nanoelectronic power sources. *Nature* **449**, 885-889 (2007).
17. F. Qian, S. Gradečak, Y. Li, C.-Y. Wen, C. M. Lieber, Core/multishell nanowire heterostructures as multicolor, high-efficiency light-emitting diodes. *Nano Lett.* **5**, 2287-2291 (2005).
18. F. Patolsky, G. Zheng, C. M. Lieber, Fabrication of silicon nanowire devices for ultrasensitive, label-free, real-time detection of biological and chemical species. *Nat. Protoc.* **1**, 1711-1724 (2006).
19. T. Cohen-Karni, B. P. Timko, L. E. Weiss, C. M. Lieber, Flexible electrical recording from cells using nanowire transistor arrays. *Proc. Natl. Acad. Sci. U.S.A.* **106**, 7309-7313 (2009).
20. B. Tian, T. Cohen-Karni, Q. Qing, X. Duan, P. Xie, C. M. Lieber, Three-dimensional, flexible nanoscale field-effect transistors as localized bioprobes. *Science* **329**, 830-834 (2010).
21. T. J. Kempa, J. F. Cahoon, S. K. Kim, R. W. Day, D. C. Bell, H. G. Park, C. M. Lieber, Coaxial multishell nanowires with high-quality electronic interfaces and tunable optical cavities for ultrathin photovoltaics. *Proc. Natl. Acad. Sci. U.S.A.* **109**, 1407-1412 (2012).
22. S. K. Kim, R. W. Day, J. F. Cahoon, T. J. Kempa, K. D. Song, H. G. Park, C. M. Lieber, Tuning light absorption in core/shell silicon nanowire photovoltaic devices through morphological design. *Nano Lett.* **12**, 4971-4976 (2012).

## **Part I Nanowire structures for intracellular sensing**

### **Chapter 2 Branched nanowire field-effect transistors as nanoscale intracellular probes**

#### **2.1 Introduction**

The ability to make electrical measurements inside cells has led to many important advances in electrophysiology (1-6). The patch clamp technique, in which a glass micropipette filled with electrolyte is inserted into a cell, offers both high signal-to-noise (S/N) ratio and temporal resolution (1, 2). Ideally, the micropipette should be as small as possible to increase the spatial resolution and reduce the invasiveness of the measurement, but the overall performance of the technique depends on the impedance of the interface between the micropipette and the cell interior (1, 2), which limits how small the micropipette can be. Techniques that involve inserting metal or carbon micro-electrodes into cells are subject to similar constraints (4, 7-9). Field-effect transistors (FETs) can also record electric potentials inside cells (10), and because their performance does not depend on impedance (11, 12), they can be made much smaller than micropipettes and microelectrodes. Moreover, FET arrays are better suited for multiplexed measurements. Previously, FET-based intracellular recording with kinked nanowire structures have been demonstrated (10), but the kink configuration and device design places limits on the probe size and the potential for multiplexing. In this chapter, a new approach based on branched nanowire structures, in which a SiO<sub>2</sub> nanotube is synthetically integrated on top of a nanoscale

FET, is reported. The fabricated nanotube branch can penetrate the cell membrane, bringing the cell cytosol into contact with the FET, which is then able to record the intracellular transmembrane potential (**Fig. 2.1**). Simulations show that the bandwidth of this branched intracellular nanotube FET (BIT-FET) is high enough for it to record fast action potentials even when the nanotube diameter is decreased to 3 nm, a length scale well below that accessible with other methods (*1, 2, 4*). Studies of cardiomyocyte cells demonstrate that when phospholipid-modified BIT-FETs are brought close to cells, the nanotubes can spontaneously penetrate the cell membrane to allow the full-amplitude intracellular action potential to be recorded, thus showing that a stable and tight seal forms between the nanotube and cell membrane. Multiplexed intracellular signals recorded from both single cells and networks of cells with multiple BIT-FETs are also demonstrated.

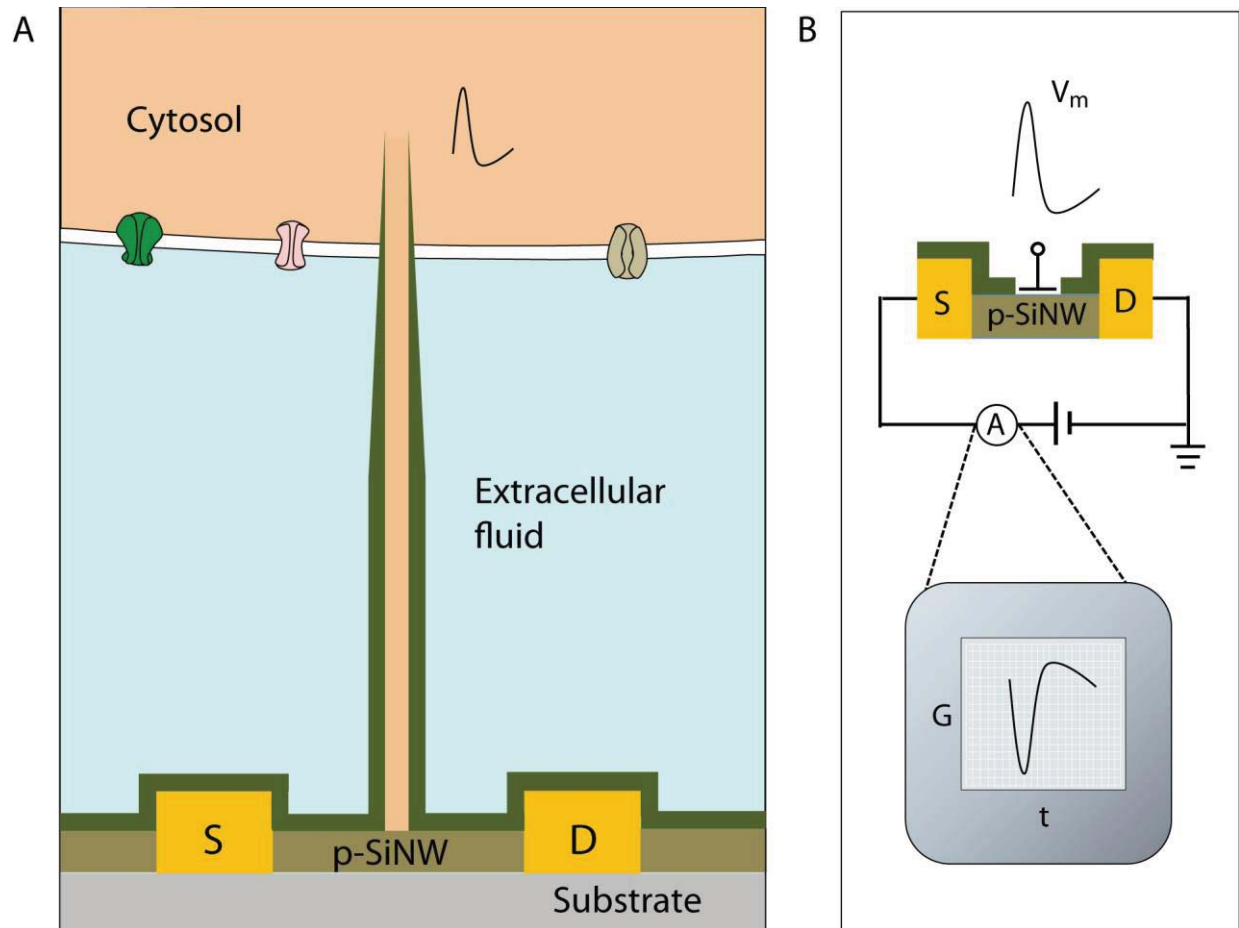


**Figure 2.1 Design and recording principle of branched intracellular nanotube transistors (BIT-FETs).** Schematic illustration of (A) a cell coupled to a BIT-FET and (B) the variation in device conductance  $G$  with time  $t$  during an action potential  $V_m$ . S and D indicate source and drain electrodes. The SiO<sub>2</sub> nanotube connects the cytosol (orange) to the p-type Si nanowire FET and, together with the SiO<sub>2</sub> passivation (green), excludes the extracellular medium (light blue) from the active device channel. The structures on the membrane represent different ion channels, and are not scaled to the true size of the BIT-FET device.



## 2.2 Experimental

### 2.2.1 Synthesis of Si/Ge branched nanowires

Single crystal p-type Si nanowires were synthesized by the Au nanocluster catalyzed VLS process as described previously (12). 100 nm diameter Au nanoclusters (Ted Pella) were dispersed on SiO<sub>2</sub>/Si growth substrates (Nova Electronic Materials), and growth was carried out using SiH<sub>4</sub> (2.5 sccm), B<sub>2</sub>H<sub>6</sub> (3 sccm, 100 ppm in He) and Ar carrier (10 sccm) for 20~30 mins at a total pressure of 25 Torr and temperature of 450–460 °C. The synthesized ca. 100 nm diameter p-type Si nanowires were deposited from an isopropanol dispersion onto SiN<sub>x</sub> surface of silicon wafers (100 nm thermal SiO<sub>2</sub>, 200 nm SiN<sub>x</sub>, n-type, 0.005 V·cm, Nova Electronic Materials). Ge nanowire branches, which serve as the template for the final nanotube structures, were also synthesized by the Au nanocluster catalyzed VLS process. A modification of the sequential branch growth process described previously was used (13) (**Fig. 2.2, i-iii**). First, Au nanodots were defined by electron-beam lithography (EBL, JEOL JSM-7000F) and metal evaporation on the top surfaces of the dispersed Si nanowires, the chip was placed in the growth reactor, and then Ge nanowire branches were grown with an initial nucleation step using GeH<sub>4</sub> (10 sccm, 10% in H<sub>2</sub>) and H<sub>2</sub> (200 sccm) at total pressure of 100 Torr and growth temperature of 305–315 °C for 5 min and with an elongation step (gas flow and pressure same as for nucleation at 280–295 °C for 20 min. The Ge nanowire branch diameter, which defines the final SiO<sub>2</sub> nanotube inner diameter, is controlled through the size and thickness of the deposited Au nanodots. Growth with Au nanodots of 80 nm diameter and 40 nm thickness yielded average 50 nm Ge nanowire branches on top of Si nanowire backbones. The Ge nanowire lengths are determined by

the growth time with typical values of 2-4  $\mu\text{m}$ . The specific orientation of the Ge nanowires was not controlled in these studies because the penetration of the nanotubes into cells does not require them to be vertical. For this reason, we selected and used Ge nanowires within  $30^\circ$  with respect to the surface normal for BIT-FET devices.

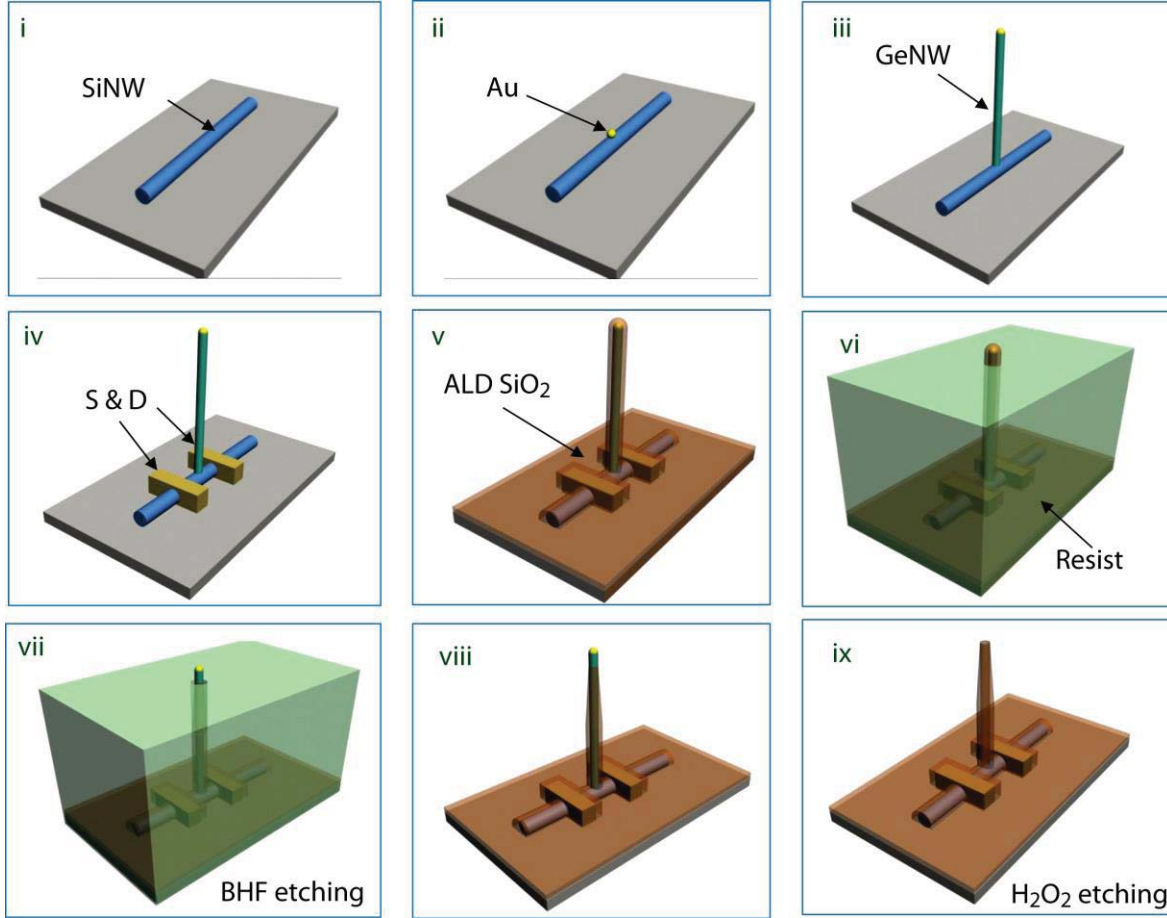


**Figure 2.2 Fabrication of BIT-FETs.** (i) Si nanowire is dispersed on substrate; (ii) Au nanodot is defined on the Si nanowire using EBL and thermal evaporation; (iii) Ge nanowire is grown on top of the Si nanowire through Au nanocluster catalyzed VLS process; (iv) EBL is used to define metal contacts on the Si nanowire at each side of the Ge nanowire branch; (v) SiO<sub>2</sub> is deposited by ALD to yield a conformal coating over the entire device; (vi) photoresist with thickness smaller than the Ge nanowire branch height is coated on the chip; (vii) Buffered hydrofluoric

**Figure 2.2 (Continued):** acid (BHF) is used to etch the SiO<sub>2</sub> at the tip of the Ge nanowire branch; (viii) isotropic BHF etching of SiO<sub>2</sub> yields tapered nanotube with smaller SiO<sub>2</sub> thickness and outer diameter at the upper part of the nanotube; (ix) the Ge nanowire branch is removed to yield a SiO<sub>2</sub> nanotube connected to the Si nanowire FET.

### 2.2.2 Fabrication of branched intracellular nanotube field-effect transistors

Following Ge nanowire branch growth, resist was coated on the chip (~2  $\mu\text{m}$  copolymer MMA (EL11) and ~0.5  $\mu\text{m}$  PMMA (950 C5), MicroChem Corp.), baked at 180 °C for 10 min. Then EBL and thermal evaporation were used to define Ti/Pd/Ti (1.5/120/10 nm) S/D contacts on each side of selected Ge nanowire branches, which are within 30° with respect to the surface normal, on the corresponding Si nanowire backbones (**Fig. 2.2, iv**). The typical separation between S/D contacts was 300-700 nm. Critical point drying (Auto Samdri 815 Series A, Tousimis) was used during lift-off and rinse steps to minimize collapse of the Ge nanowire branches. A uniform layer of SiO<sub>2</sub> (~50 nm) was deposited by atomic layer deposition (ALD, Savannah-S200, Cambridge NanoTech) at 250 °C (14), and annealed in the ALD system at 250 °C for 15 min. The conformal SiO<sub>2</sub> layer (**Fig. 2.2, v**) serves both as the nanotube wall (after removal of Ge) and passivation of the metal electrodes. The Ge nanowire core is removed by a sequence of steps to yield the final nanotube device (**Fig. 2.2, vi-ix**). First, a photoresist protection layer (Shipley S1813 or S1818, MicroChem Corp.) was coated to a thickness smaller than the Ge nanowires height, baked at 115 °C for 5 min, and then the exposed SiO<sub>2</sub> of the Ge/SiO<sub>2</sub> core/shell structure was removed by BHF (Buffered HF Improved, Transene) (20~25 s for ~50 nm ALD SiO<sub>2</sub>). The BHF etching goes along both the radial and axial direction, which results in a tapered SiO<sub>2</sub> shell. Following

photoresist lift-off, hydrogen peroxide ( $\text{H}_2\text{O}_2$ , 30%, Sigma) was used to selectively etch the Ge (50 °C, 45-60 min). The final  $\text{SiO}_2$  nanotube height is defined by the thickness of the photoresist protection layer. Unless specifically mentioned, all devices used, including those for device characterization and cell measurements etc., use nanotube inner diameter and ALD  $\text{SiO}_2$  thickness of ca. 50 nm, nanotube length of 1-1.5  $\mu\text{m}$ , p-type Si nanowires with diameter of ca. 100 nm.

### **2.2.3 Intracellular measurements of action potentials**

#### **2.2.3.1 Electrical characterizations of the device**

To characterize the gate response of the BIT-FET devices in aqueous solution, a 2 mm thick PDMS sheet with a 15 mm  $\times$  10 mm window was put on the device chip, and the open region was filled with 1 $\times$  phosphate buffered saline (PBS, Mediatech, Inc.); a Ag/AgCl electrode was inserted into the solution and the FET conductance vs. water gate voltage ( $V_{\text{wg}}$ ) measurements were carried out by sweeping the voltage while simultaneously recording the FET current with a current preamplifier (1211, DL Instruments). The voltage sweep output and the preamplifier output were generated and recorded with a DAC card (PCI-6030E, National Instruments, Inc.) under computer control, with typical ramp speed of 50 mV/s. To assess the temporal response of the BIT-FET devices, a pulsed  $V_{\text{wg}}$  with variable rise time (0.1-50 ms) was generated (Axon Digidata 1440A Data Acquisition System, Molecular Devices Inc.) and the current of the FET was amplified with a home-built current preamplifier, filtered (CyberAmp 380, Molecular Devices, Inc.), and then digitized (Axon Digidata 1440A Data Acquisition System, Molecular Devices, Inc.). Conductance values recorded for BIT-FET devices vary between ca. 1-70  $\mu\text{S}$ .

This variation reflects differences in the Si nanowires and device configuration, but has no effect on calculated potentials since the sensitivity of each device was determined prior to cell measurements.

#### **2.2.3.2 Intracellular recordings of action potentials**

Embryonic chicken cardiomyocytes were cultured using published protocols on thin PDMS films (10, 15). Device chips were incubated with lipid vesicles of 1,2-dimyristoyl-sn-glycero-3-phosphocholine (DMPC, Avanti Polar Lipids Inc.) containing 1% 1-myristoyl-2-[12-[(7-nitro-2-1,3-benzoxadiazol-4-yl) amino] dodecanoyl]-sn-glycero-3-phosphocholine (NBDlipid, Avanti Polar Lipids Inc.) as fluorescent reporter to form supported lipid layers on devices including nanotube surfaces, using a procedure described earlier (10). The cell recording measurements were carried out in Tyrode solution (pH ~ 7.3) at 30-37 °C using a 100 mV DC source voltage for the BIT-FET devices. The current was amplified with a home-built multi-channel current preamplifier, filtered with a 6 kHz low pass filter (CyberAmp 380), and digitized at 50-250 kHz sampling rate (Axon Digi1440A). Ag/AgCl reference electrodes were used to fix the extracellular solution potential in all recording experiments (10, 15). The PDMS/cell sheets were manipulated using glass micropipettes to control the relative position between the cells and the nanotubes.

## 2.3 Results and discussion

### 2.3.1 Nanowire synthesis and material characterizations

Our BIT-FET is a combination of a silicon nanowire FET detector and an electrically insulating SiO<sub>2</sub> nanotube that connects the FET to the intracellular fluid (the cytosol) (**Fig. 2.1A**). When there is a change in transmembrane potential  $V_m$ , such as that during an action potential, the varying potential of the cytosol inside the nanotube gives rise to a change in the conductance  $G$  of the FET in a manner equivalent to applying a time-varying potential to the gate electrode in a traditional FET (**Fig. 2.1B**). For a p-type FET under constant source/drain (S/D) bias the polarity of the change in  $G$  is inverted with respect to that in  $V_m$ . Since the BIT-FET design uses the tip of a size-controllable nanotube to interface with the cells, it can achieve the smallest ultimate probe size (which is also enabled by the use of the FET sensor). In addition because the nanotube is built on top of a planar FET, BIT-FET arrays can fully take advantage of the high density of planar nanoFETs, in contrast to previous work (10).

The BIT-FET devices were prepared through a sequence of growth and fabrication steps described earlier, which enable control of key individual device parameters as well as the density of multiple devices (**Fig. 2.2**). Ge nanowire branches grown on top of Si nanowires using a Au nanocluster catalysed VLS mechanism (13) were used as sacrificial templates for the nanotubes (**Fig. 2.3A**). Representative scanning electron microscopy (SEM) images show a Au nanodot and the resulting Ge nanowire branch ‘standing up’ on the Si nanowire and oriented nearly normal to the substrate surface (**Fig. 2.3B**). After defining S/D contacts on each side of selected Ge nanowires, a conformal, controlled-thickness SiO<sub>2</sub> layer deposited by atomic layer deposition

(ALD) (14) provided the nanotube wall and S/D passivation. Representative SEM images of the resulting structure clearly show this conformal  $\text{SiO}_2$  shell and the Ge core (**Fig. 2.3C**).

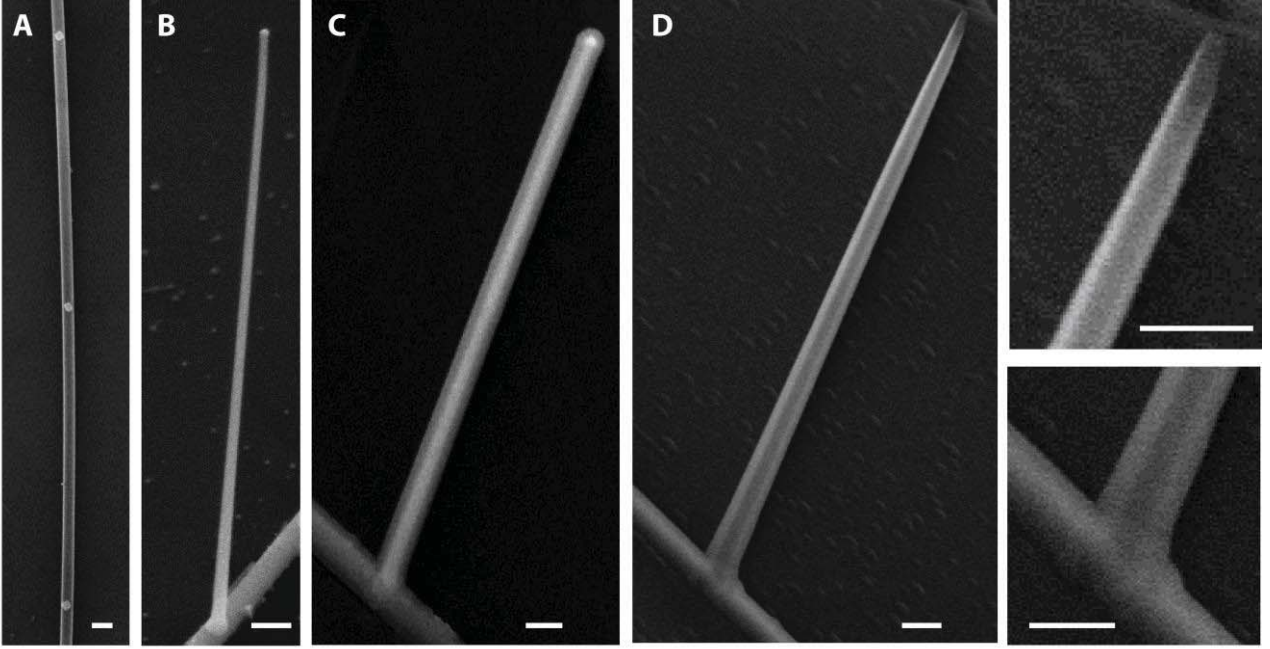


**Figure 2.3 SEM characterizations of BIT-FETs.** (A) SEM image of a Si nanowire with multiple Au nanodots defined on the surface. (B) SEM image of a Ge nanowire branch on a Si nanowire oriented close to the surface normal. (C) SEM image of a Ge nanowire branch on a Si nanowire coated with ALD  $\text{SiO}_2$ . (D) SEM image of a final nanotube on a Si nanowire (left) and magnified images of the tip (top right) and base (bottom right) of the nanotube. Scale bars: 200 nm.

Fabrication of the BIT-FET device was completed by two etching steps. In the first etching process, the topmost part of the  $\text{SiO}_2$  shell was selectively removed with BHF to expose the Ge core; in the second, the Ge nanowire was etched away to leave a hollow  $\text{SiO}_2$  nanotube on a Si nanowire. SEM images confirm that the end of the nanotube is open (**Fig. 2.3D**). Comparison of



images before and after etching further shows that the nanotube structure is open to the Si nanowire surface, as indicated by the bright to dark change in image contrast associated with removal of the Ge. These images also demonstrate that the very tip of the nanotube has an outer diameter of  $\sim 55$  nm, which increases to a maximum of 150 nm at a distance of  $\sim 2.2$   $\mu\text{m}$  from the tip (**Fig. 2.3D**). This tapering effect results from isotropic etching by the BHF, and we believe this is a particularly advantageous feature in that it leads to a decrease in probe size.

### **2.3.2 Electrical characterizations of the branched intracellular nanotube field-effect transistors**

We characterized the electrical properties of the BIT-FETs and several control devices in solution to elucidate the behavior of this new device architecture. The SEM image in **Fig. 2.4A** shows a representative two-FET structure, where a BIT-FET and a conventional nanowire FET with similar channel length were fabricated with a common source electrode on the same Si nanowire. In both devices, the Si nanowire and electrodes exposed to solution were passivated with  $\sim 50$  nm ALD  $\text{SiO}_2$  as described above. Before etching the Ge core of the BIT-FET, measurements of  $G$  for both devices as a function of water-gate voltage ( $V_{\text{wg}}$ ) (**Fig. 2.4B**) show very little variation (with a sensitivity of approximately 2170 nS/V). Significantly, measurements made on the same devices after removal of the Ge nanowire core (to yield an open nanotube structure) demonstrate a large increase in the sensitivity of the BIT-FET to 24,530 nS/V, whereas the control FET shows no change (**Fig. 2.4C**). Taken together, these results confirm that BIT-FET devices respond selectively and with high sensitivity to the solution inside the nanotubes rather than that outside, and thus meet the requirements for intracellular recording outlined schematically in **Fig. 2.1**. The difference in sensitivity of the BIT-FET devices to solution inside



rather than outside the nanotubes originates primarily from the gate capacitance difference (11, 12). Specifically, Ge over-coating on the Si nanowire may lead to a larger contact area between the Si nanowire and the internal solution of the nanotube (the active FET area) than defined by the nanotube inner diameter, which can increase this difference in sensitivity.

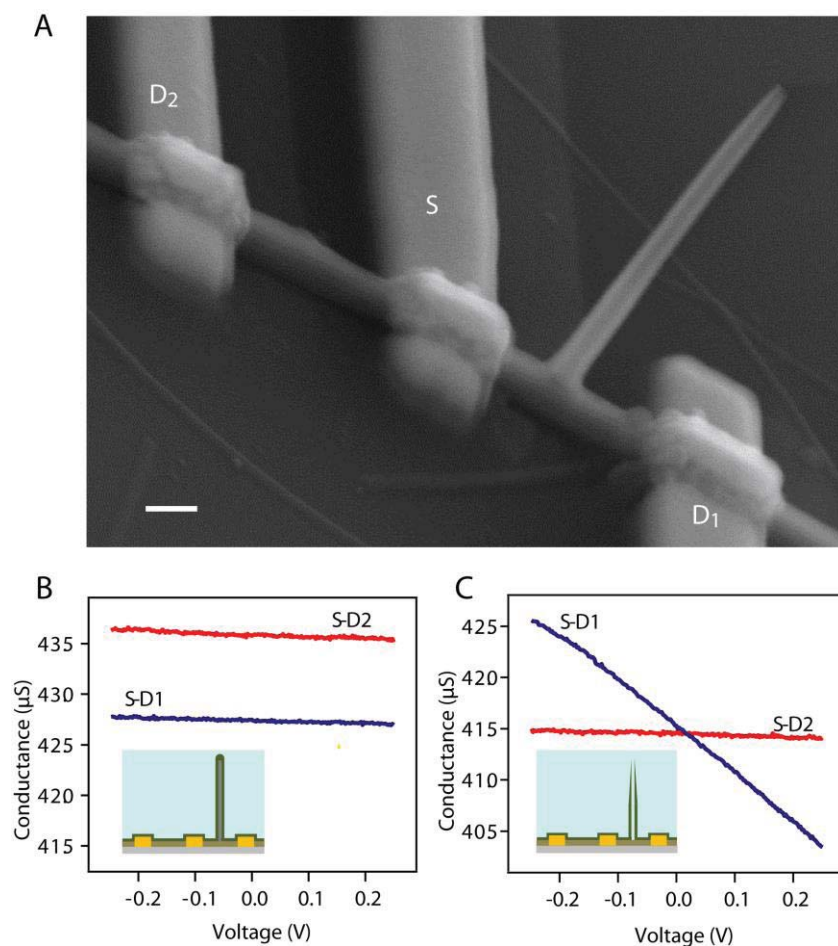


**Figure 2.4 Electrical characterizations of BIT-FETs.** (A) SEM image of a BIT-FET device (S-D1) and a control device (S-D2). Scale bar, 200 nm (B, C) Conductance vs. water-gate voltage before (B) and after (C) etching of the Ge nanowire core for the BIT-FET (blue) and control device (red).

We also characterized the temporal response of BIT-FET devices to assess their ability to record fast cellular processes. Accordingly, a pulsed  $V_{wg}$  with a rise/fall time of 0.1 ms, duration of 1 ms and amplitude of 100 mV was applied to approximate an action potential. The conductance exhibited a peak (dip) coincident with the 0.1 ms rise (fall) of the pulse, and a plateau step down during the constant 100 mV portion of the pulse (**Fig. 2.5A**). With rise/fall times ranging from 0.1 to 50 ms for the pulsed  $V_{wg}$ , the conductance change associated with the baseline to plateau was found to be independent of the pulse rise time; this change is consistent with the device sensitivity determined from quasi-static measurements. The peak and dip features in the pulsed  $V_{wg}$  results correspond to the expected capacitive charging (16) of the passivated metal electrodes and are not intrinsic to the BIT-FET. These capacitive features can be readily removed from the BIT-FET and control device data to yield the pure FET response (**Fig. 2.5A, red curve**). The results demonstrate that the BIT-FET can faithfully record potential changes with a time resolution of at least 0.1 ms. We note that these capacitive features would not be expected in cellular measurements because (1) the metal electrodes are only coupled to extracellular media, where the potential changes are quite small (15), and (2) these changes will be localized on the size scale of a cell, which is much smaller than the electrode area exposed to solution ( $\sim\text{cm}^2$ ) in the pulsed  $V_{wg}$  experiments here.

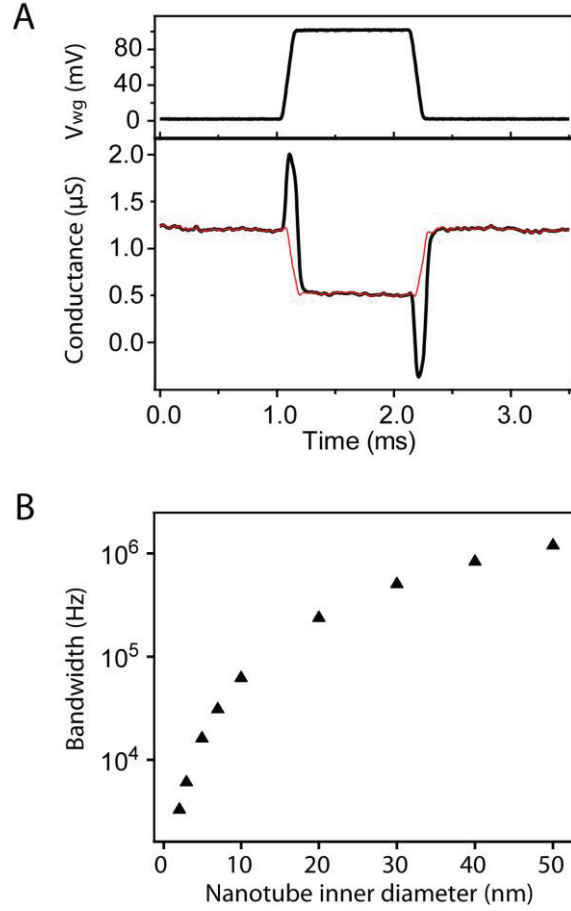


**Figure 2.5 Temporal characterizations of BIT-FET gate response.** (A) A  $V_{wg}$  pulse (top) with an amplitude of 100 mV and duration of 1 ms (rise and fall times of 0.1 ms), and the corresponding plot of conductance vs. time for a BIT-FET device (black trace, bottom). The red trace is the pure field-effect response after removing the capacitive signals of the passivated metal electrodes. (B) Calculated bandwidth (upper limit) of the BIT-FET device vs. the inner diameter of the nanotube (with the nanotube length fixed at 1.5  $\mu m$ ).

We also modelled the BIT-FET device to estimate the bandwidth (which is beyond our current measurement limit) and its dependence on nanotube diameter. The signal transduction in the BIT-FET device can be readily solved by the classical transmission line model (16). In our

analysis, we determined the change in potential at the silicon-nanowire FET surface ( $V_n$ ) as a function of time following a step change in the transmembrane potential at the nanotube opening to  $V_0$ . For a typical nanotube (inner diameter, 50 nm; ALD  $\text{SiO}_2$  thickness, 50 nm; length, 1.5  $\mu\text{m}$ ), the calculated response yields a bandwidth of  $\sim 1.2$  MHz (**Fig. 2.5B**). This represents an upper limit assuming that the active FET area and relevant device capacitance  $C_{\text{NW}}$  are defined only by the nanotube inner diameter, and could be reduced to 0.2 MHz if we assume the entire Si nanowire surface is active due to Ge over-coating. A summary of the results shows that the BIT-FET can achieve a bandwidth of  $\geq 6$  kHz (which is sufficient for recording a rapid neuronal action potential (1, 2)) for nanotube inner diameters as small as 3 nm (fixed length, 1.5 mm) (**Fig. 2.5B**). The high bandwidth determined for the BIT-FET devices results in large part from the small device capacitance, despite the increasingly large solution resistance within the nanotube with decreasing inner diameter. The small diameters accessible with the BIT-FET suggest that it could be minimally invasive and capable of probing the smallest cellular structures, including neuron dendrites and dendritic spines, which is difficult using conventional electrical-based techniques (17, 18).

### 2.3.3 Intracellular recordings of action potentials with a single device

We investigated the capability of the BIT-FET to record intracellular signals using spontaneously beating embryonic chicken cardiomyocyte cells, which were cultured on thin pieces of PDMS as described previously (15). After modifying the devices with phospholipids (10) to facilitate the internalization of the nanotubes into cells, the PDMS-cell sheet was manipulated to put a cell into gentle contact with the nanotube of a BIT-FET under a standard electrophysiology

microscope. Approximately 45 s after gentle contact was made and in the absence of an applied force on the cell substrate, the recorded data showed a dramatic change (**Fig. 2.6A**). Before the transition to intracellular signal, the signal exhibits a relatively flat baseline with small biphasic peaks (amplitude,  $\sim 5\text{--}8$  mV; duration,  $\sim 1$   $\mu\text{s}$ ) with a frequency of  $\sim 1$  Hz (**Fig. 2.6B and C**). These peaks are coincident with cell beating and consistent with extracellular recording reported previously (15). The baseline then shifts approximately 235 mV, and new peaks with amplitude of 75-100 mV and duration of  $\sim 200$   $\mu\text{s}$  are observed (**Fig. 2.6A and D**). The recorded conductance data give inverted peaks for the p-type silicon nanowire FETs used here, although the calibrated potentials are consistent with standard peak polarity and the shape of intracellular action potentials. These intracellular peaks have the shape and features characteristic of the intracellular action potential of cardiomyocyte cells (10, 19, 20), including fast depolarization at the beginning of the peak, a plateau region, fast repolarization and hyperpolarization, and a return to baseline (**Fig. 2.6D**). The signal transition from extra- to intracellular indicates penetration of the cell by the nanotube. The baseline shift is similar to that measured recently using kinked-nanowire probes (10), but smaller than the standard resting potential for cardiomyocytes (19, 20). Our reproducible and stable recording of full-amplitude action potentials, which is a central result of our work, suggests that this baseline difference is not due to poor sealing during nanotube internalization. We propose that the discrepancy in the resting potentials could be attributed to a stronger suspension effect introduced by the intracellular polyelectrolytes at the junction (21, 22) owing to the order-of magnitude smaller size of the  $\text{SiO}_2$  nanotube opening than in a typical patch-clamp pipette. More detailed studies will be required to quantitatively understand the origin of this effect. Although the nanotube dimensions routinely

used in our intracellular recording studies (inner diameter, 50 nm; tip outer diameter, 55 nm) are larger than the smallest achievable for BIT-FETs (**Fig. 2.5B**), they are still much smaller than the typical glass micropipettes (1, 2) and metal microelectrodes (3, 4, 7) used in intracellular studies. The change from the extracellular signal to intracellular signal without applying external force to the cell suggests the spontaneous penetration of the cell membrane by the nanotube rather than mechanical insertion. We speculate that lipid fusion (23, 24) may play an important role in this penetration, similar to our previous observations (10), and that the small nanotube size is probably beneficial both for this lipid fusion process and for the formation of a tight seal. There are several attractive consequences arising from this spontaneous penetration. First, it typically leads to full amplitude recording of the action potential, without the need for circuitry to compensate for probe-membrane leakage, thus suggesting tight sealing between the nanotube and cell membrane. Indeed, control experiments carried out without phospholipid modification of the BIT-FETs required external forces to achieve the transition to intracellular action potential signals, and the smaller amplitude of these signals (10-30 mV) suggests leakage at the nanotube-membrane interface (3). Second, we find that spontaneous penetration occurs in the same way for a broad range of nanotube orientations (that is, within 30° of the surface normal), in contrast to mechanical insertion. Third, we believe that the tight nanotube-membrane seal and the very small nanotube internal volume, ~3 aL, help to preserve cell viability and a stable signal over time. In general, we find that the termination of signal recording by the BIT-FET is due to random separation of the nanotube as a result of the motion of the beating cardiomyocyte cell, and not to cell death or degradation of the nanotube/cell membrane interface (the latter is normally the case when recording with glass micropipettes (1, 2)). In addition, and unlike a glass micropipette,

when the BIT-FET nanotube is separated from a cell (on purpose, as shown in the following, or as a result of the beating motion), the nanotube can re-penetrates the same cell multiple times at approximately the same position without affecting the cell or the recorded signal. Finally, the total recording time from multiple penetrations with the BIT-FET at a given position on a cell can exceed an hour.

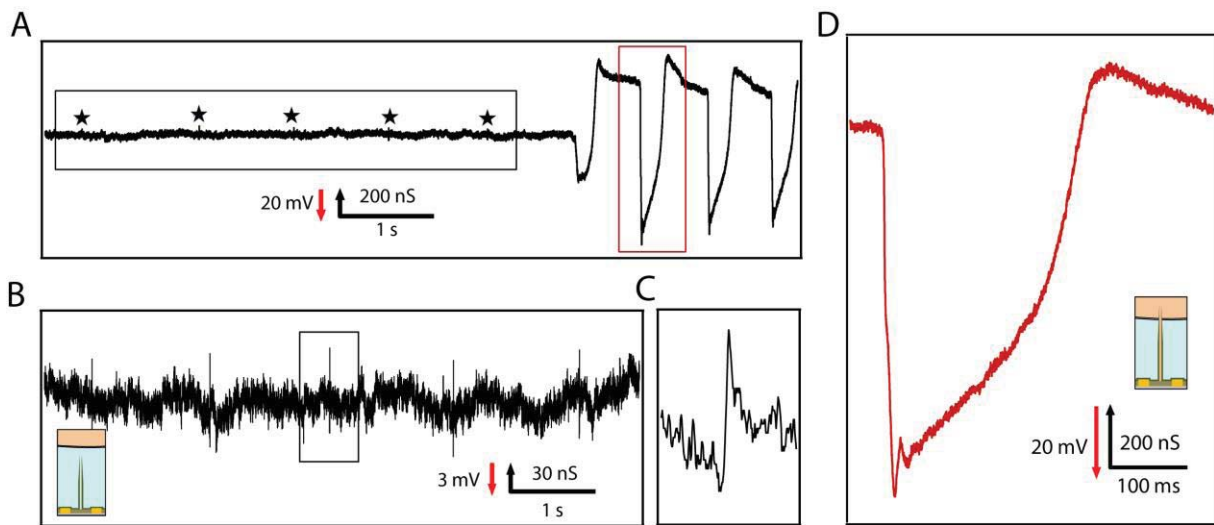


**Figure 2.6 Intracellular recording of action potentials with BIT-FETs.** (A) Representative trace (conductance vs. time) reflecting the transition from extracellular to intracellular recording. (B) Magnified view of the trace inside the black dashed rectangle in A. (C) Magnified view of the trace inside the black rectangle in B. The stars in A mark the positions of extracellular spikes. (D) Magnified view of the peak inside the red dashed rectangle in A. The potential was calibrated using the sensitivity values measured on phospholipid modified devices by quasi-static  $V_{wg}$  measurement and pulsed  $V_{wg}$  measurement with a rise/fall time of 0.1 ms. The sensitivity obtained from these two measurements is the same.

The BIT-FET devices are also robust and reusable. Specifically, following retraction of the cell substrate from the device, which results in the conductance returning to the extracellular baseline, subsequent gentle contact of the nanotube to the same cell without changing position leads once again to the development of stable intracellular action potential signals. We have repeated the gentle contact/intracellular recording/retraction cycle up to five times with the same BIT-FET nanotube near the same position on the cell without any observable change in the beating frequency and action potential features. A SEM image of the BIT-FET device following these repeated cycles shows that the nanotube remains intact with some residue on the upper outer surface. In addition, we did not see evidence of blockage of the nanotube during these cycles, which we attribute to the spontaneous penetration mechanism rather than suction or mechanical insertion. Note that the devices can even be reused after being dried. Taken together, these results demonstrate the reliability and robustness of the BIT-FETs and strongly suggest that this is a minimally invasive intracellular recording technique.

#### **2.3.4 Multiplexed intracellular recordings of action potentials**

A feature of our BIT-FET design is its facility for the straightforward fabrication of multiple, independent devices to enable multiplexed recording from single cells and cell networks. For example, we have readily aligned two phospholipid-modified BIT-FET devices, separated by  $\sim 20\ \mu\text{m}$ , with a single, beating cardiomyocyte cell (**Fig. 2.7A**). Following gentle contact, conductance vs. time measurements made simultaneously using both devices show that device 1 first bridged the cell membrane to yield clear intracellular signals (**Fig. 2.7B**). Approximately 10 s later, we observed the development of intracellular peaks from device 2. Subsequently, intracellular signals were recorded from both devices. We can glean several important points



from these data. First, the sequential nature with which the intracellular signals develop, in the absence of an applied force, strongly supports the suggestion above that penetration of the cell membrane by the phospholipid-modified nanotubes is a spontaneous biomimetic process that does not adversely affect the cell. Second, the intracellular peaks recorded simultaneously by devices 1 and 2 (full amplitude, 75–100 mV) and stable cell beating over time are consistent with a tight seal being established between the cell membrane and the nanotubes in both devices. In addition, we have also demonstrated that multiplexed measurements with BIT-FETs can be extended to cell networks (**Fig. 2.8**). We have recorded intracellular action potentials simultaneously from different sites in a monolayer of beating cardiomyocyte cells. In the future, we suggest that this BIT-FET design will be implementable on high-density integrated planar nanoFETs, either large arrays of nanowire FETs (25) or conventional top-down nanoFET arrays (26), to enable multiplexed recording at a far higher density than demonstrated in these initial studies.

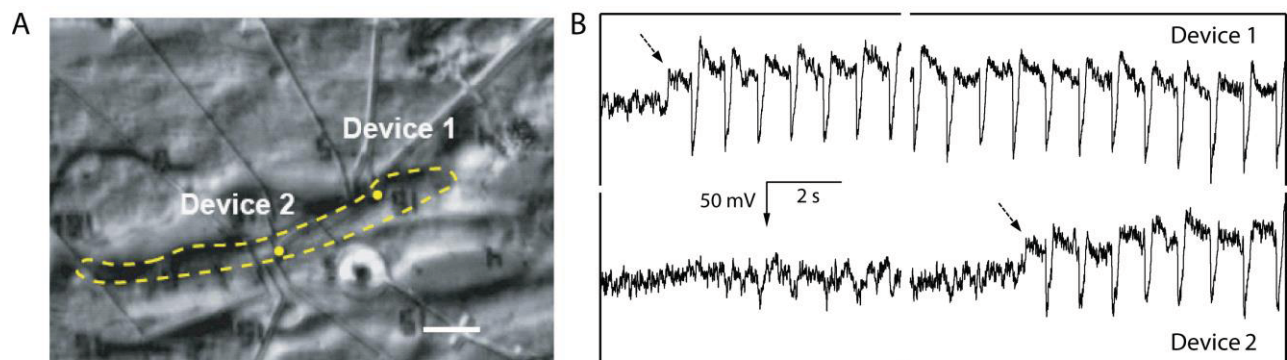


**Figure 2.7 Multiplexed intracellular recording of action potentials from two BIT-FETs.** (A) Differential interference contrast (DIC) microscopy image of two BIT-FET devices (positions marked with dots) coupled to a single cardiomyocyte cell, with the cell boundary marked by the

**Figure 2.7 (Continued):** yellow dashed line. Scale bar, 10  $\mu\text{m}$ . **(B)** Simultaneously recorded traces from the two devices in **A**, corresponding to the transition from extracellular to intracellular recording. The transition happened in a sequential manner. The break mark labels the  $\sim 1$  s discontinuity between the two adjacent traces.

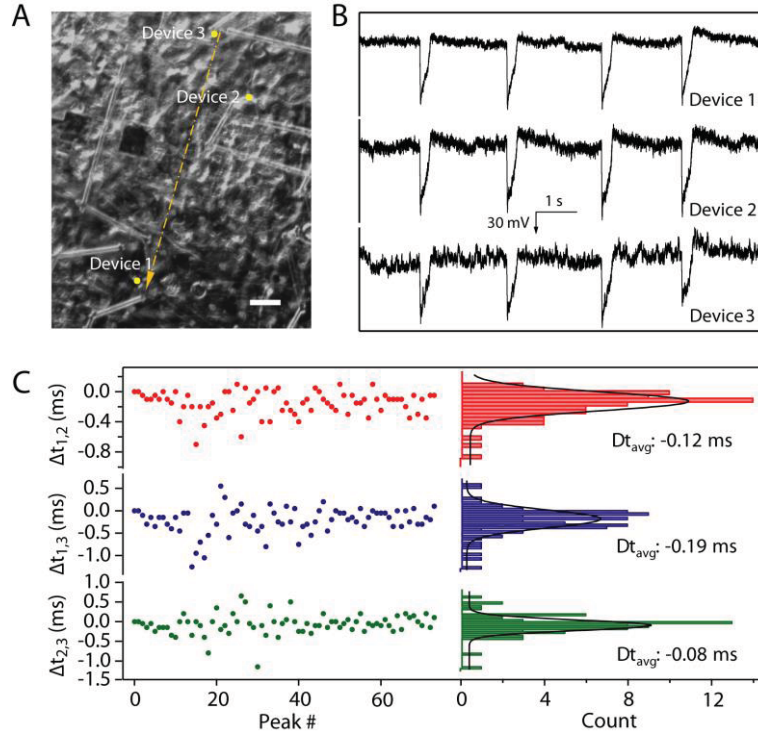


**Figure 2.8 Multiplexed intracellular recording of action potentials from cell networks.** **(A)** DIC image of three BIT-FET devices coupled to a beating cardiomyocyte cell network. Scale bar, 30  $\mu\text{m}$ . **(B)** Representative traces recorded simultaneously from the devices shown in **A**. The three devices measure intracellular action potential signals from different cells in the cell network. The potential was calibrated using the sensitivity values measured for each individual device, and all devices yield corresponding intracellular action potential values with full amplitude of 75-100 mV (independent of the conductance and sensitivity variation). **(C)** Time differences between action potential signals between device 1 and 2 ( $t_{1,2}$ ), device 1 and 3 ( $t_{1,3}$ ), and device 2 and 3 ( $t_{2,3}$ ).

## **2.4 Conclusion and outlook**

Additional work remains to be done to improve further the BIT-FET-based intracellular measurement technique. The S/N ratio is still lower than that of glass micropipettes. Implementing the capability for cell stimulation in addition to recording will also be important for intracellular studies. However, we believe that the advantages of the BIT-FET already demonstrated in this work, including the capability to realize sub-5 nm probes, the formation of tight nanotube-cell membrane seals and the potential for large-scale, high-density, multiplexed recording, make it an attractive new measurement tool that will extend substantially the scope of fundamental and applied electrophysiology studies to regimes hard to access by current methods.

## 2.5 Bibliography

1. B. Sakmann, E. Neher, Patch clamp techniques for studying ionic channels in excitable membranes. *Annu. Rev. Physiol.* **46**, 455-472 (1984).
2. A. Molleman, *Patch clamping: An introductory guide to patch clamp electrophysiology*. (2003).
3. W. L. Rutten, Selective electrical interfaces with the nervous system. *Annu. Rev. Biomed. Eng.* **4**, 407-452 (2002).
4. R. D. Purves, *Microelectrode methods for intracellular recording and iontophoresis*. (1981).
5. E. Chorev, J. Epsztein, A. R. Houweling, A. K. Lee, M. Brecht, Electrophysiological recordings from behaving animals--going beyond spikes. *Curr. Opin. Neurobiol.* **19**, 513-519 (2009).
6. J. Dunlop, M. Bowlby, R. Peri, D. Vasilyev, R. Arias, High-throughput electrophysiology: An emerging paradigm for ion-channel screening and physiology. *Nat. Rev. Drug Discov.* **7**, 358-368 (2008).
7. A. Hai, J. Shappir, M. E. Spira, In-cell recordings by extracellular microelectrodes. *Nat. Methods* **7**, 200-202 (2010).
8. M. G. Schrlau, N. J. Dun, H. H. Bau, Cell electrophysiology with carbon nanopipettes. *ACS Nano* **3**, 563-568 (2009).
9. E. D. De Asis, J. Leung, S. Wood, C. V. Nguyen, High spatial resolution single multiwalled carbon nanotube electrode for stimulation, recording, and whole cell voltage clamping of electrically active cells. *Appl. Phys. Lett.* **95**, 153701 (2009).
10. B. Tian, T. Cohen-Karni, Q. Qing, X. Duan, P. Xie, C. M. Lieber, Three-dimensional, flexible nanoscale field-effect transistors as localized bioprobes. *Science* **329**, 830-834 (2010).
11. S. M. Sze, K. K. Ng, *Physics of semiconductor devices*. (2006).
12. F. Patolsky, G. Zheng, C. M. Lieber, Nanowire-based biosensors. *Anal. Chem.* **78**, 4260-4269 (2006).
13. X. Jiang, B. Tian, J. Xiang, F. Qian, G. Zheng, H. Wang, L. Mai, C. M. Lieber, Rational growth of branched nanowire heterostructures with synthetically encoded properties and function. *Proc. Natl. Acad. Sci. U.S.A.* **108**, 12212-12216 (2011).

14. D. Hausmann, J. Becker, S. Wang, R. G. Gordon, Rapid vapor deposition of highly conformal silica nanolaminates. *Science* **298**, 402-406 (2002).
15. T. Cohen-Karni, B. P. Timko, L. E. Weiss, C. M. Lieber, Flexible electrical recording from cells using nanowire transistor arrays. *Proc. Natl. Acad. Sci. U.S.A.* **106**, 7309-7313 (2009).
16. M. N. O. Sadiku, *Elements of electromagnetics*. (2000).
17. M. Scanziani, M. Hausser, Electrophysiology in the age of light. *Nature* **461**, 930-939 (2009).
18. J. T. Davie, M. H. Kole, J. J. Letzkus, E. A. Rancz, N. Spruston, G. J. Stuart, M. Hausser, Dendritic patch-clamp recording. *Nat. Protoc.* **1**, 1235-1247 (2006).
19. D. M. Bers, Cardiac excitation-contraction coupling. *Nature* **415**, 198-205 (2002).
20. D. P. Zipes, J. Jalife, *Cardiac electrophysiology: From cell to bedside*. (2009).
21. R. P. Buck, E. S. Grabbe, Electrostatic and thermodynamic analysis of suspension effect potentiometry. *Anal. Chem.* **58**, 1938-1941 (1986).
22. I. Tasaki, I. Singer, Some problems involved in electric measurements of biological systems. *Ann. NY Acad. Sci.* **148**, 36-53 (1968).
23. L. V. Chernomordik, M. M. Kozlov, Mechanics of membrane fusion. *Nat. Struct. Mol. Biol.* **15**, 675-683 (2008).
24. B. D. Almquist, N. A. Melosh, Fusion of biomimetic stealth probes into lipid bilayer cores. *Proc. Natl. Acad. Sci. U.S.A.* **107**, 5815-5820 (2010).
25. H. Yan, H. S. Choe, S. Nam, Y. Hu, S. Das, J. F. Klemic, J. C. Ellenbogen, C. M. Lieber, Programmable nanowire circuits for nanoprocessors. *Nature* **470**, 240-244 (2011).
26. *International technology roadmap for semiconductors*. (<http://www.itrs.net>, 2009; Downloaded in October, 2011).

# **Chapter 3 Ge/Si core/shell nanowire-templated Si nanotube transistors as nanoscale intracellular probes**

## **3.1 Introduction**

An electronic device that can interface to the intracellular region of a live cell has several important constraints, including (1) small size, which can minimize invasiveness and potentially allow contact to subcellular structures, (2) high sensitivity with decreasing size, and (3) capability to multiplex at both single cell and cell network levels (1, 2). Well-established electrophysiological techniques for cellular recording, such as patchclamp micropipettes (3), metal microelectrodes (4) and intracellular glass microelectrodes (5, 6), have advanced the understanding of electrogenic cells, although they also have limitations in terms of (1) decreasing signal and signal-to-noise (S/N) with decreasing probe size in the submicron regime and (2) capabilities for multiplexed measurements on single cells as well as larger-scale multiplexing for cell networks. Recently, researchers have been addressing these issues with the development of novel transistor-based probes (7-9) and improved designs for micro/nanoelectrodes (10-12). The micro/nanoelectrodes exploit structures projecting from chip plane to enable invagination of cultured cell membranes and measurements of intracellular-like action potentials (10-12), although as passive recording electrodes they are limited in terms of their potential for miniaturization. On the other hand, transistor-based probes can be reduced in size to at least the 10nm scale (1, 13). However, an active transistor requires two contacts for operation, and until recently this constraint has made intracellular recording devices difficult to achieve. Two

solutions have been reported to address this difficulty involving the synthesis of (1) kinked nanowire FETs (KNW-FETs) with a transistor or diode at the tip, where the nonlinear nanowire structure enables ready insertion into cells (7, 9), and (2) branched intracellular nanotube FETs (BIT-FETs, see Chapter 2), where the transistor remains outside of the cell but senses the intracellular potential via the solution inside the passive nanotube bridge (8).

In this chapter, a conceptually new and practically simple field-effect transistor based probe is reported that consists of a single semiconductor nanotube. The underlying principle of the active nanotube transistor, ANTT, intracellular probe (**Fig. 3.1**) involves the fabrication of S/D contacts to one end of a silicon or other semiconductor nanotube and electrical isolation of these S/D contacts from surrounding medium such that the solution filling the interior of the nanotube can gate the transistor and the variation of interior electrochemical potential is then recorded as a change in device conductance. Hence, if the free end of an ANTT probe is inserted into the interior of an electrogenic cell, the time-dependent changes associated with an action potential spike will give rise to time-varying conductance signal that maps the intracellular action potential. However, if a similarly configured solid silicon (or other semiconductor) nanowire is inserted into the cell, no signal would be observed since it would not be possible to ‘gate’ the transistor. We note that for p-type silicon nanotubes as used in our proof-of-concept studies, a positive change of intracellular potential yields a negative change in device conductance, although the conductance can be quantitatively converted to potential using water-gate calibration measurements (1, 7-9).

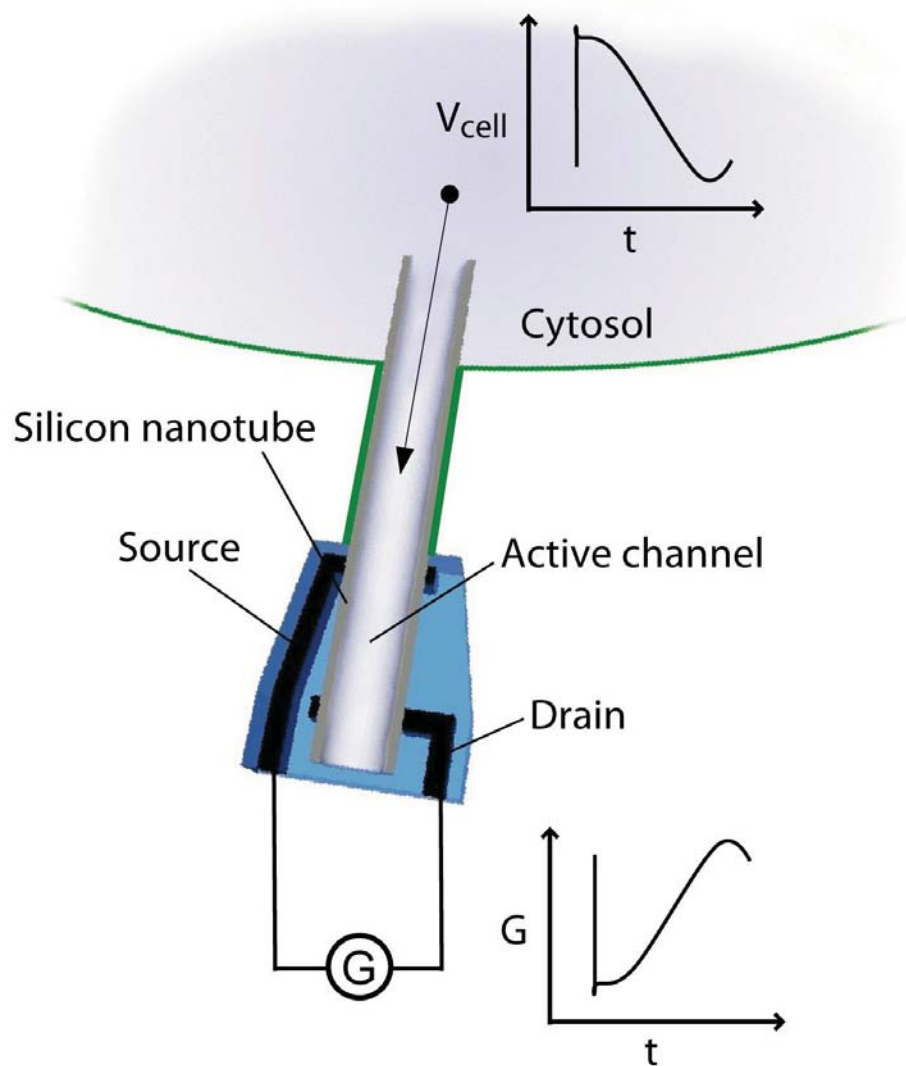


**Figure 3.1 Design and recording principle of active nanotube transistors (ANTTs).** Schematic illustration of an ANTT probe inserted into a cell and recording an intracellular action potential ( $V_{\text{cell}}$  vs. time,  $t$ ) as a conductance ( $G$ ) change in the p-type active FET region between S/D contacts. Sensitivity to voltage changes from the external extracellular environment is effectively eliminated by SU-8 passivation of the nanotube region around the S/D contacts. The nanotube is shown as a half-cylinder for clarity.



## 3.2 Experimental

### 3.2.1 Synthesis of Ge/Si core/shell nanowires

The Ge/Si core/shell nanowires were synthesized by Au nanocluster catalyzed VLS process as described previously (14, 15). 50 or 15 nm diameter Au nanoclusters (Ted Pella) were dispersed on Si/SiO<sub>2</sub> substrates (Nova Electronic Materials). The Ge core growth was carried out using GeH<sub>4</sub> (20-30 sccm, 10% in H<sub>2</sub>) and H<sub>2</sub> (200 sccm) for 30 min at a total pressure of 300-400 Torr and temperature of 270-310 °C. The p-type Si shell (ca. 25 nm in thickness) was subsequently grown on the 50 nm Ge core by uncatalyzed decomposition of SiH<sub>4</sub> (1 sccm) and B<sub>2</sub>H<sub>6</sub> (10 sccm, 100 ppm in H<sub>2</sub>) at a total pressure of 20 Torr and temperature of 475 °C for 30 min. We note that p-type Si shell (15-20 nm) growth on the 15 nm Ge core was carried out at a reduced deposition rate: 3 sccm SiH<sub>4</sub>, 15 sccm B<sub>2</sub>H<sub>6</sub> (100 ppm in H<sub>2</sub>) and 50 sccm H<sub>2</sub> at a total pressure of 9 Torr and temperature of 450 °C for 40 min. A final annealing step at 600 °C for 1.5 h under vacuum ( $2.8 \times 10^{-3}$  Torr) gave the crystalline Ge/Si core/shell nanowires.

### 3.2.2 Fabrication of active silicon nanotube transistors

ANTT probes were fabricated on the SiN<sub>x</sub> surface of Si substrates (100 nm thermal SiO<sub>2</sub>, 200 nm SiN<sub>x</sub>, n-type, 0.005 V·cm, Nova Electronic Materials). A Ni sacrificial layer (80 nm) was first defined by electron beam lithography (EBL) and thermal evaporation. The substrate was then coated with SU-8 resist (2000.5, MicroChem Corp.), on which the as-synthesized Ge/Si core/shell nanowires were deposited by either of two methods (**Fig. 3.2, i**): (1) nanowires suspended in isopropyl alcohol were deposited from solution; (2) nanowires were directly contact-printed as described previously (16). After definition of the bottom SU-8 support layer

by EBL (**Fig. 3.2, ii**), source/drain (S/D) metal contacts were defined by EBL and metalized by thermal evaporation of Cr/Pd/Cr (1.5/75/50 nm). Typically, the S/D contact separation was 0.5-1  $\mu\text{m}$  and the free end of the nanowire extended 3-4  $\mu\text{m}$  from the source contact (**Fig. 3.2, iii**). The top SU-8 layer was subsequently defined by EBL for passivation (**Fig. 3.2, iv**). Etching of the Ni sacrificial layer (1.5 h) in nickel etchant (TFB, Transene Company, Inc.) and the Ge core of the core/shell nanowire (65  $^{\circ}\text{C}$ , 30-60 min) in hydrogen peroxide ( $\text{H}_2\text{O}_2$ , 30%, Sigma) yielded the ANTT probes (**Fig. 3.2, v**).

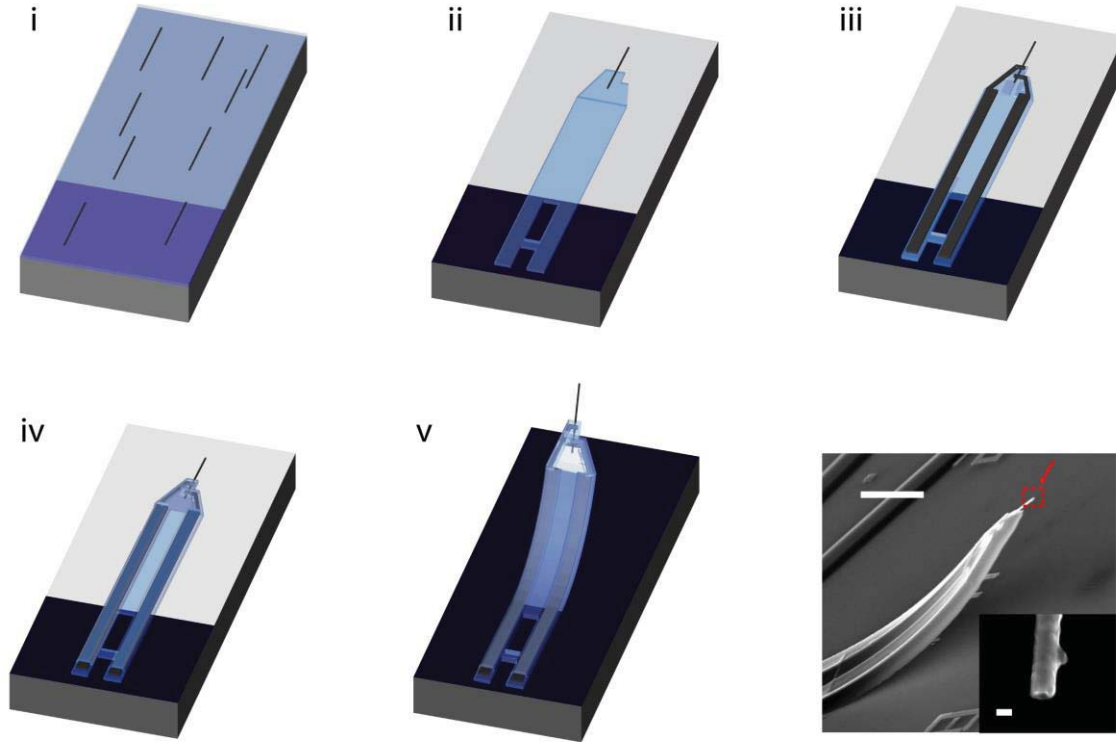


**Figure 3.2 Fabrication of ANTTs.** (i) Transfer of Ge/Si core/shell nanowires (Ge/Si nanowires) to a SU-8 layer which was deposited and prebaked on a sacrificial Ni layer (colored silver); (ii) registration of positions of Ge/Si nanowires and definition of the bottom SU-8 layer by EBL and hard-bake; (iii) definition of S/D metal contacts by EBL and thermal evaporation; (iv) definition

**Figure 3.2 (Continued):** of the top SU-8 passivation layer by EBL and hard-bake; (v) etching of the sacrificial layer and Ge nanowire core (left) and the scanning electron microscopy (SEM) image of the final ANTT probe (right). Scale bar, 10  $\mu\text{m}$ . Inset, zoom of the probe tip from the dashed red box. Scale bar, 100 nm.

### 3.2.3 Intracellular measurements of action potentials

#### 3.2.3.1 Electrical characterizations of the device

ANTT device sensitivity was defined as S/D conductance change in response to gate voltage ( $V_{\text{wg}}$ ) applied by Ag/AgCl reference electrode.  $V_{\text{wg}}$  was typically swept at a rate of 80 mV/s from -0.4 V to +0.4 V. The S/D current, driven by 100 mV source voltage, was amplified by a current preamplifier (1211, DL Instruments) at sensitivity of  $10^{-6}$  or  $10^{-7}$  A/V, filtered (0-3 kHz, CyberAmp 380, Molecular Devices, Inc.) and digitized at 50-250 kHz sampling rate (Axon Digidata 1440A Data Acquisition System, Molecular Devices, Inc.).

#### 3.2.3.2 Intracellular recordings of action potentials

Embryonic chicken cardiomyocytes on PDMS were prepared using published protocols (17). Before intracellular recording, probe chips were incubated with lipid vesicles of 1,2-dimyristoyl-sn-glycero-3-phosphocholine (DMPC, Avanti Polar Lipids Inc.) containing 1% 1-myristoyl-2-{12-[(7-nitro-2-1,3-benzoxadiazol-4-yl) amino] dodecanoyl}-sn-glycero-3-phosphocholine (NBD-lipid, Avanti Polar Lipids Inc.) as fluorescence reporter using a procedure described earlier (7). The recordings were carried out in  $1\times$  Tyrode solution (pH 7.3) at 37 °C using a 100 mV DC source voltage for ANTTs. The S/D current was converted to voltage with a current

preamplifier, low-pass filtered and digitized as described previously. A pulled glass micropipette was used for manipulation of the cardiomyocytes/PDMS sheet (17).

### 3.3 Results and discussion

#### 3.3.1 Nanowire synthesis and material characterization

We first characterized the Si nanotubes synthesized by etching of the Ge nanowire core of Ge/Si nanowires with SEM and TEM (**Fig. 3.3**). The inner diameter of the nanotube was determined by the Ge core and thus the Au catalyst size for the core growth. Furthermore, the shell thickness depended on the shell growth time. Therefore, through the synthetic control of the core and shell growth, the nanotube dimensions can be finely tuned (**Fig. 3.3A**). The Si nanotubes were then transferred to a TEM grid and imaged in different magnifications under bright/dark field imaging conditions. High resolution image of the Si nanotube wall shows that it is crystalline and the electron diffraction pattern of a section of the nanotube further confirms its crystallinity (**Fig. 3.3B-E**). However, we note that in some of the samples, defects and grain boundaries were observed in the TEM image, suggesting a poly-crystalline nature of the Si nanotubes.

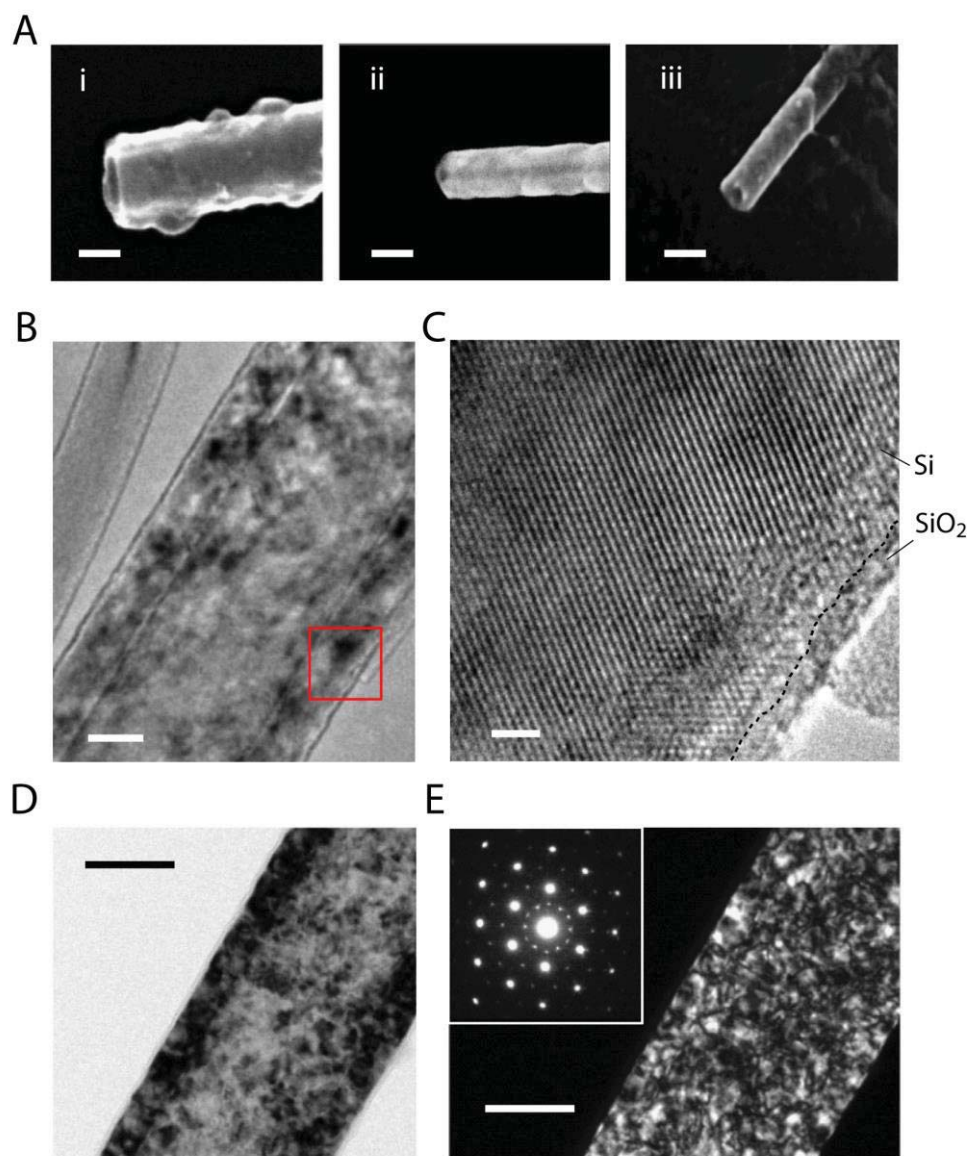


**Figure 3.3 SEM and TEM characterizations of the Si nanotube templated by Ge/Si core/shell nanowires.** (A) SEM images of Si nanotubes templated by Ge/Si core/shell nanowires with (i) ~50 nm Ge core and ~25 nm Si shell, (ii) ~15 nm Ge core and ~15 nm Si shell and (iii) ~10 nm Ge shell and ~10 nm Si shell. The Ge cores were etched with H<sub>2</sub>O<sub>2</sub> aqueous solution. Scale bars: 50 nm. (B) TEM image of a section of the Si nanotube. The Ge core was etched with H<sub>2</sub>O<sub>2</sub> aqueous solution. Scale bar, 20 nm. (C) High resolution TEM image of the Si nanotube wall (red box in B). Scale bar, 2 nm. (D) Bright-field TEM image of a section of the Si nanotube.

**Figure 3.3 (Continued):** Scale bar, 50 nm. (E) Dark-field TEM image of the section of the Si nanotube. Scale bar, 50 nm. Inset, electron diffraction pattern recorded from the entire Si nanotube section.

### 3.3.2 Electrical characterizations of the device

We investigated the electrical properties of the probe structures in aqueous solution before and after etching the Ge nanowire cores. Prior to Ge-etching, conductance ( $G$ ) vs. water-gate potential ( $V_{wg}$ ) data show only a small change with a sensitivity of  $\sim 0.10 \mu\text{S/V}$  (**Fig. 3.4A**). Notably, after etching the Ge core to form the ANTT device the water-gate data exhibits a  $30\times$  sensitivity increase to  $3.0 \mu\text{S/V}$ . These results are consistent with the increased gate coupling afforded by solution access to the Si-nanotube interior. To rule out the possibility that the Ge-etching process degrades the SU-8 passivation, we carried out control experiments on an i-Si/p-Si core/shell nanowire structure, where the shell is similar to the Ge/Si core/shell nanowires used to make ANTT devices. Significantly, the Si/Si control device with SU-8 passivated S/D contacts showed similar sensitivity to the Ge/Si device and little or no sensitivity change following the same etching conditions used to remove Ge and yield the ANTT device. Taken together these results show that (1) the top/bottom SU-8 passivation effectively isolates the FET channel from external solution potential changes, and (2) the ANTT structure has good sensitivity to potential changes coupled through solution in the nanotube interior.

In addition, we have explored the capability of the ANTTs to detect chemical changes in pH sensing experiments. Measurements of the device conductance as a function of stepwise increasing pH showed a systematic increase with the increasing negative charge on the  $\text{SiO}_2$

surface (18) of the p-type nanotube interior (**Fig. 3.4B**). These data plotted as change in potential vs. solution pH yield a device pH sensitivity of up to 37 mV/pH, a value that is consistent with previous results reported for Si nanowire devices (7). Measurements made before and after closing the nanotube device end with SU-8 (**Fig. 3.4B, inset**) confirm that this change is indeed due to pH detection from the solution inside the nanotube as no variation in device conductance was observed after blocking solution exchange. These results show the potential of the ANTT probe to detect chemical and biochemical changes as previously demonstrated by nanowire FET sensors (7, 18), although we note that necessity for diffusion of analytes within the nanotube will reduce the temporal resolution compared to external surface binding.

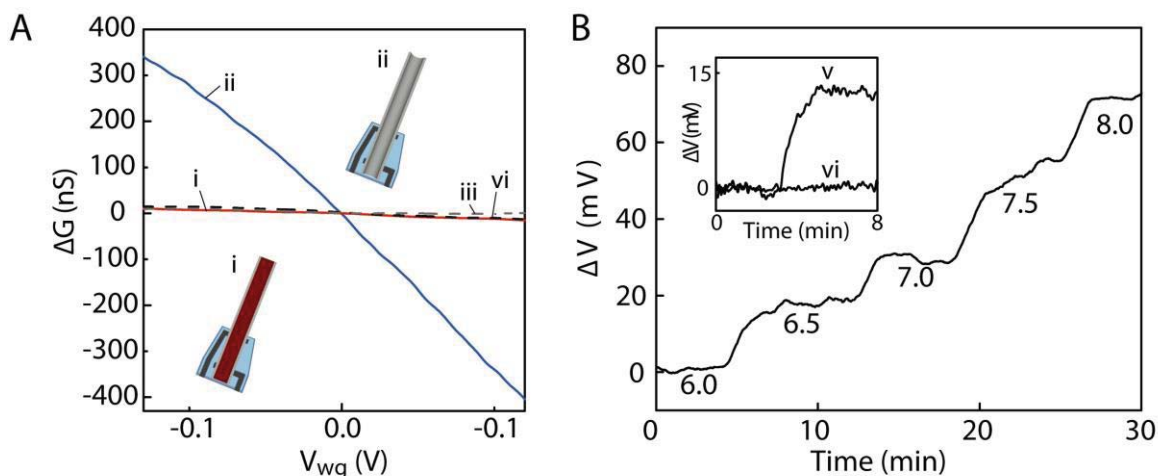


**Figure 3.4 Electrical characterizations of ANTTs.** (A) Change of conductance,  $\Delta G$ , vs. water-gate potential,  $V_{wg}$ , prior to (i) and after (ii)  $H_2O_2$  etching of the Ge nanowire core. Plots (iii) and (iv) correspond to  $\Delta G$  vs.  $V_{wg}$  for an i-Si/p-Si core/shell nanowire device before and after, respectively, etching using the same conditions as for the Ge nanowire core etching. All measurements were made in  $1\times$  phosphate-buffered saline ( $1\times$  PBS) with a Ag/AgCl reference gate electrode. Insets, schematic illustration of an ANTT device prior to (i) and after (ii)  $H_2O_2$  etching of the Ge nanowire core (deep red). (B) Change in potential,  $\Delta V$ , in response to step



**Figure 3.4 (Continued):** changes in solution pH. The potential values were calibrated by the water-gate sensitivity of  $2.0 \mu\text{S/V}$ . Inset,  $\Delta V$  as the pH is increased stepwise from 7.0 to 8.0 for an ANTT device (v) and for the same device after closing the tip with SU-8 resist to prevent solution access to the interior of the nanotube (vi).

### 3.3.3 Intracellular recordings of action potentials with a single device

We explored the possibility of recording intracellular action potential with the ANTT probes using spontaneously firing chicken cardiomyocytes similarly to Chapter 2. In these experiments, ANTT probes relieved from the surface were modified with a phospholipid layer (7-9), and the cardiomyocytes were cultured on flexible sheets of polydimethylsiloxane (PDMS) as described previously (17). Next, the PDMS/cell sheet was moved to orient a single cell over an ANTT probe tip with an optical microscope. After contact with the cell, we initially observed regularly spaced spikes with a frequency of 1.8 Hz and correlated with cell beating (**Fig. 3.5A**). These peaks detected initially after contact had widths of  $\sim 0.7$  ms and amplitudes up to 10 mV that are consistent with extracellular cardiomyocyte action potentials reported previously (1, 8, 17).

Notably, over a period of ca. 100 seconds following contact between the ANTT probe tip and PDMS-supported cell the recorded periodic signals change substantially (**Fig. 3.5B**) with an increase in amplitude and duration to 40-50 mV and ca. 200 ms respectively. Over a period of several minutes the peak amplitude continues to increase until stable periodic peaks are observed with amplitude and duration of ca. 80 mV and 200 ms, respectively (**Fig. 3.5C**). The peak duration and shape were similar to values reported for cardiomyocyte intracellular action potentials (19-21), and thus we can associate these data with intracellular action potential

recording by the ANTT probe. Indeed, closer examination of a representative steady-state recorded peak shows five phases that can be associated with (1) resting state, (2) rapid depolarization, (3) plateau, (4) rapid repolarization, and (5) hyperpolarization, as discussed previously (**Fig. 3.5D**) (7).

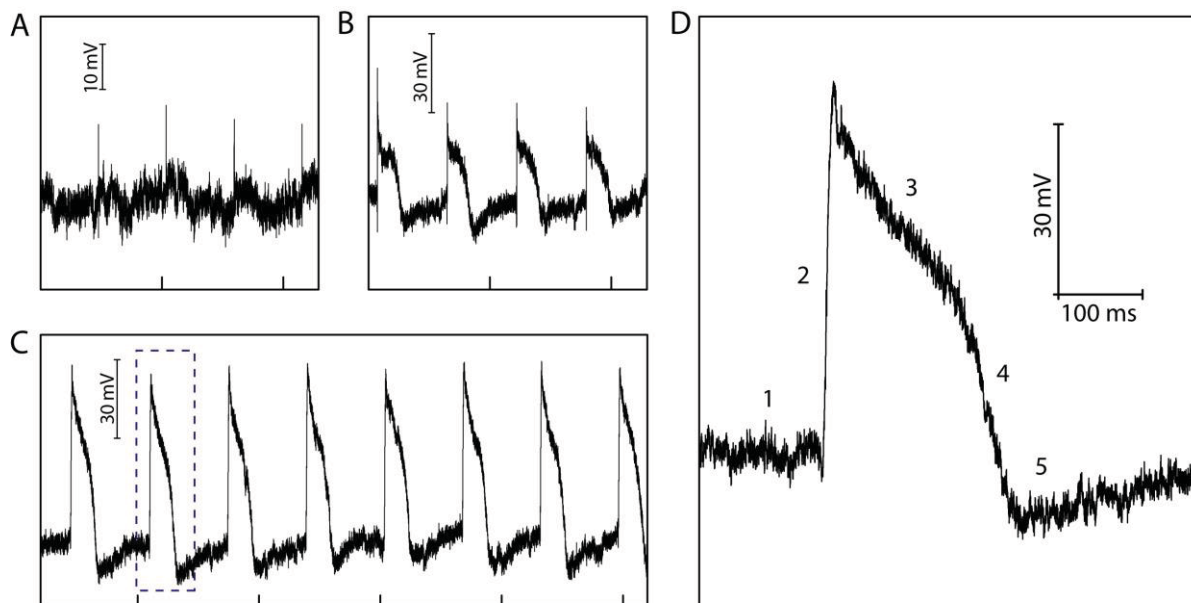


**Figure 3.5 Intracellular recording of action potentials with ANTTs.** (A) Representative potential vs. time data recorded immediately following contact between the ANTT probe and a single cardiomyocyte. (B) Representative potential vs. time data recorded ca. 100 s following the initial contact between the ANTT probe and a single cardiomyocyte in trace A. (C) Stable potential vs. time data recorded ca. 5 min following trace B. The tick marks in A-C correspond to 1 s. (D) Zoom of the single intracellular action potential peak in trace C highlighted with the dashed box. The five characteristic phases of the action potential peak, denoted by 1-5, are defined in text. In all the traces, the recorded device conductance was calibrated with the measured water-gate sensitivity to yield the plotted voltage signal.

### 3.3.4 Nanotube size effect on the intracellular recordings

We note that intracellular recording experiments carried out with ANTT probes of smaller nanotube diameters showed similar intracellular action potential peaks (**Fig. 3.6**). Intracellular action potentials recorded from 15/50 and 10/30 nm (inner/outer diameters) Si nanotubes showed a couple of features in the recorded signals, consistent with the size-scaling predicted for the related BIT-FET: (1) lower temporal resolution and (2) smaller maximum amplitude of recorded action potentials compared with probes with 50/100 nm Si nanotubes (8). As the nanotube inner diameter decreases, the resistive-capacitive (RC) effect of the electrolyte inside the nanotube becomes more significant and serves a low-pass filter for the recorded signals. Similar to the bandwidth calculation and analysis of BIT-FET devices in Chapter 2, the bandwidths of the ANTT devices can be modeled by finite element analysis and calculated for different inner diameters. The modeling shows that as the inner diameter of the Si nanotube decreases, the bandwidths of the ANTT devices show a nearly linear decrease. Therefore, in order to increase the device bandwidth, a tapered inner diameter is ideal to reduce the RC effect and thus improve the device temporal resolution while maintaining the small tip size. This experiment would be discussed in more details in the next chapter.

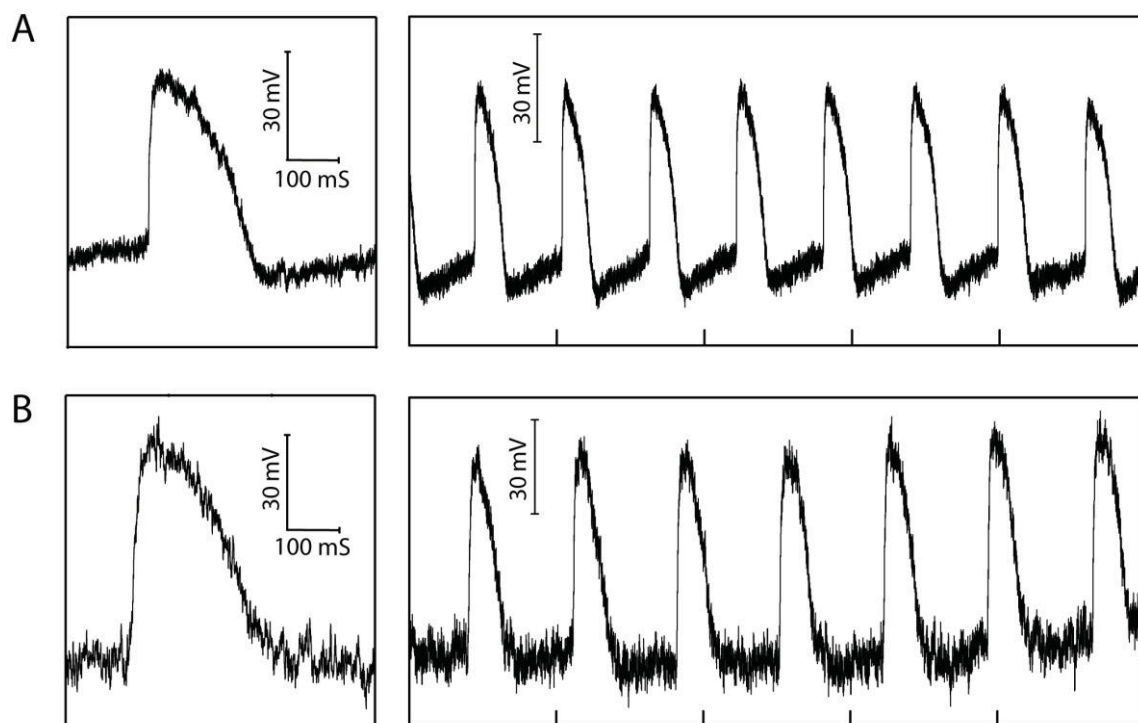


**Figure 3.6 Nanotube size effect on the intracellular recordings.** (A) Representative potential vs. time (left: single peak; right: 5 s long trace) data recorded from ANTT probe with a ~15/50 nm inner/outer diameter Si nanotube immediately following contact between the ANTT probe with and a single cardiomyocyte. (B) Representative potential vs. time (left: single peak; right: 5 s long trace) data recorded from ANTT probe with a ~10/30 nm inner/outer diameter Si nanotube immediately following contact between the ANTT probe with and a single cardiomyocyte. The tick marks in A and B correspond to 1 s.

### 3.3.5 Multiplexed intracellular recordings of action potentials

In addition, we have investigated two directions in multiplexed recording with the ANTT probe, including (1) multiplexed ANTT devices on a single probe and (2) arrays of ANTT probes. First, we fabricated probes with two ANTT devices as shown schematically in **Fig. 3.7A**. Key steps in

the fabrication involved contact-printing (16) of the Ge/Si core/shell nanowires to produce parallel nanowires, and the use of a common source contact for both devices; the remainder of the fabrication process was similar to that described above. A representative SEM image shows clearly two ANTT devices on the single 3-D probe with a nanotube tip-to-tip separation of ca. 7.6  $\mu\text{m}$  (**Fig. 3.7A, right**). Notably, measurements made from two ANTT devices on a single probe following contact with one beating cardiomyocyte (**Fig. 3.7B**) demonstrated regular intracellular action potential peaks from both devices. At steady-state the peaks recorded by both ANTT devices exhibited potential changes of about 80 mV consistent with intracellular action potentials and results reported recently for a two-element BIT-FET (8). Examination of the data recorded by both devices shows other important features. First, the noise in both channels is not correlated, and thus we can conclude that there is no significant electrical crosstalk between the dual-device/single-probe configuration even when recording from the same cell. Second, the S/N for one device (**Fig. 3.7B, top trace**) is lower than that for the second device on the probe, which represents a limitation that will need to be improved in future for exploiting the potential of high spatial resolution recording using these multiplexed ANTT probes.

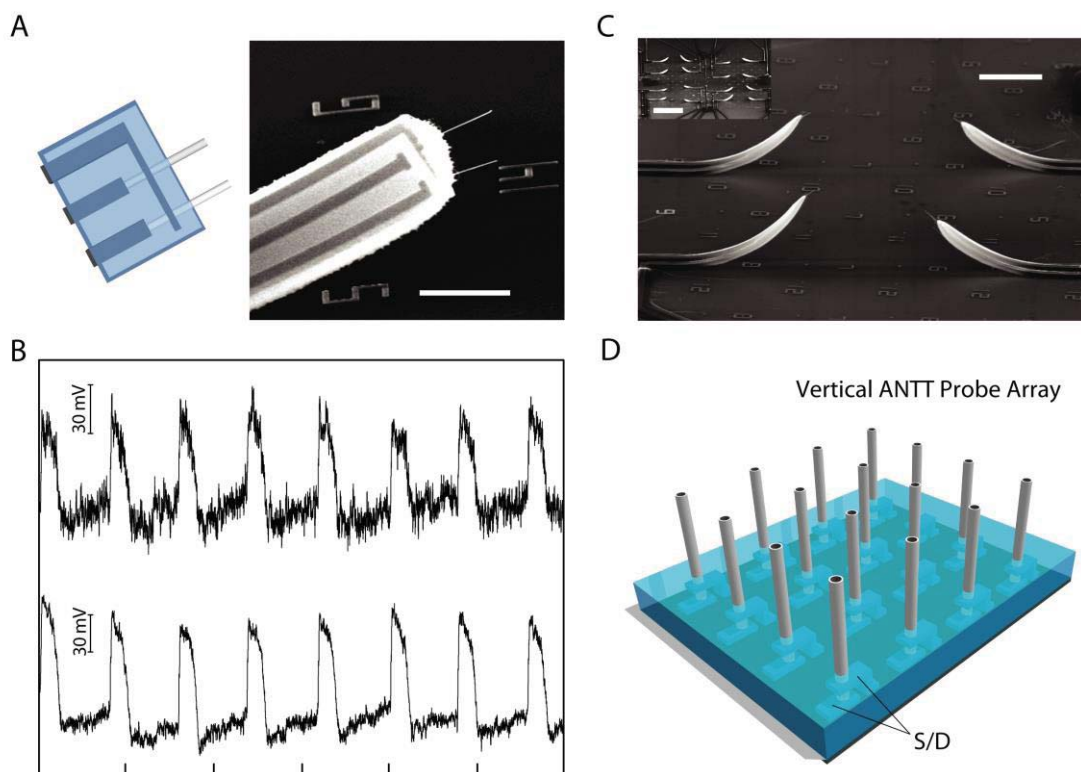


**Figure 3.7 Multiplexed intracellular recording of action potentials with ANTTs.** (A) Schematic illustration (left) and SEM image (right) of a probe with two independent ANTT devices sharing a common source contact. Horizontal scale bar, 5  $\mu\text{m}$ . (B) Intracellular recording from a single cardiomyocyte using a probe with two independent ANTT devices. The interval between tick marks corresponds to 1 s. (C) SEM image of part of an ANTT probe array fabricated from contact printed Ge/Si nanowires. Scale bar, 20  $\mu\text{m}$ . Inset, lower magnification SEM image of the  $4 \times 4$  probe array. Scale bar, 100  $\mu\text{m}$ . Probe interval is about 80  $\mu\text{m}$ . (D) Schematic illustration of chip-based vertical ANTT probe arrays fabricated using epitaxial Ge/Si core/shell nanowires and 3-D definition of S/D contacts.

Lastly, we have extended our approach to fabricate arrays of ANTT probes. For example, a  $4 \times 4$  array of single ANTT probes, with an average probe spacing of 80  $\mu\text{m}$ , was fabricated from

contact-printed Ge/Si nanowires (**Fig. 3.7C**). Denser ANTT probe arrays could be fabricated by varying the printing conditions (22). In addition, we are also exploring a strategy that involves epitaxial growth of ca. vertical Ge/Si core/shell nanowires to produce high-density ANTT probe arrays (**Fig, 3.7D**). In this approach, S/D contacts are defined vertically to the vertical semiconductor nanotubes in a manner similar to work on vertical nanowire FETs (23, 24).

### 3.4 Conclusion and outlook

In conclusion, we have demonstrated the design, synthesis, fabrication and testing of a new hollow needle-shaped nanoprobe based on an active silicon nanotube transistor termed the ANTT device. Measurements of conductance vs. water-gate potential in aqueous solution have shown that the ANTT probe is selectively gated by potential changes within the silicon nanotube, thus demonstrating the basic operating principle of the ANTT device. Studies interfacing ANTT probes with spontaneously beating cardiomyocytes demonstrated the recording of stable full-amplitude intracellular action potentials, and moreover, showed that full-amplitude action potentials could be recorded with inner tube diameters as small as 10~15 nm. In addition, the straightforward fabrication of ANTT devices was exploited to prepare multiple ANTTs at the end of single probes, which enabled multiplexed recording of full-amplitude intracellular action potentials from single cells, and multiplexed arrays of single ANTT device probes. These studies open up unique opportunities for multisite recordings from individual cells through cellular networks, including the potential for intracellular chemical sensing through modification of the inner tube surface (25). Future works remain in fabrication of vertical ANTT probe arrays as well as large-scale intracellular recordings from cellular networks.



### 3.5 Bibliography

1. B. P. Timko, T. Cohen-Karni, Q. Qing, B. Tian, C. M. Lieber, Design and implementation of functional nanoelectronic interfaces with biomolecules, cells, and tissue using nanowire device arrays. *IEEE Trans. Nanotechnol.* **9**, 269-280 (2010).
2. C. M. Lieber, Semiconductor nanowires: A platform for nanoscience and nanotechnology. *MRS Bulletin* **36**, 1052-1063 (2011).
3. B. Sakmann, E. Neher, Patch clamp techniques for studying ionic channels in excitable membranes. *Annu. Rev. Physiol.* **46**, 455-472 (1984).
4. W. L. Rutten, Selective electrical interfaces with the nervous system. *Annu. Rev. Biomed. Eng.* **4**, 407-452 (2002).
5. R. D. Purves, *Microelectrode methods for intracellular recording and iontophoresis*. (1981).
6. E. Chorev, J. Epsztein, A. R. Houweling, A. K. Lee, M. Brecht, Electrophysiological recordings from behaving animals--going beyond spikes. *Curr. Opin. Neurobiol.* **19**, 513-519 (2009).
7. B. Tian, T. Cohen-Karni, Q. Qing, X. Duan, P. Xie, C. M. Lieber, Three-dimensional, flexible nanoscale field-effect transistors as localized bioprobes. *Science* **329**, 830-834 (2010).
8. X. Duan, R. Gao, P. Xie, T. Cohen-Karni, Q. Qing, H. S. Choe, B. Tian, X. Jiang, C. M. Lieber, Intracellular recordings of action potentials by an extracellular nanoscale field-effect transistor. *Nat. Nanotechnol.* **7**, 174-179 (2012).
9. Z. Jiang, Q. Qing, P. Xie, R. Gao, C. M. Lieber, Kinked p-n junction nanowire probes for high spatial resolution sensing and intracellular recording. *Nano Lett.* **12**, 1711-1716 (2012).
10. A. Hai, J. Shappir, M. E. Spira, In-cell recordings by extracellular microelectrodes. *Nat. Methods* **7**, 200-202 (2010).
11. C. Xie, Z. Lin, L. Hanson, Y. Cui, B. Cui, Intracellular recording of action potentials by nanopillar electroporation. *Nat. Nanotechnol.* **7**, 185-190 (2012).
12. J. T. Robinson, M. Jorgolli, A. K. Shalek, M. H. Yoon, R. S. Gertner, H. Park, Vertical nanowire electrode arrays as a scalable platform for intracellular interfacing to neuronal circuits. *Nat. Nanotechnol.* **7**, 180-184 (2012).

13. T. Cohen-Karni, D. Casanova, J. F. Cahoon, Q. Qing, D. C. Bell, C. M. Lieber, Synthetically encoded ultrashort-channel nanowire transistors for fast, pointlike cellular signal detection. *Nano Lett.* **12**, 2639-2644 (2012).
14. L. J. Lauhon, M. S. Gudiksen, D. Wang, C. M. Lieber, Epitaxial core-shell and core-multishell nanowire heterostructures. *Nature* **420**, 57-61 (2002).
15. M. Ben Ishai, F. Patolsky, Shape- and dimension-controlled single-crystalline silicon and sige nanotubes: Toward nanofluidic fet devices. *J. Am. Chem. Soc.* **131**, 3679-3689 (2009).
16. A. Javey, S. Nam, R. S. Friedman, H. Yan, C. M. Lieber, Layer-by-layer assembly of nanowires for three-dimensional, multifunctional electronics. *Nano Lett.* **7**, 773-777 (2007).
17. T. Cohen-Karni, B. P. Timko, L. E. Weiss, C. M. Lieber, Flexible electrical recording from cells using nanowire transistor arrays. *Proc. Natl. Acad. Sci. U.S.A.* **106**, 7309-7313 (2009).
18. Y. Cui, Q. Wei, H. Park, C. M. Lieber, Nanowire nanosensors for highly sensitive and selective detection of biological and chemical species. *Science* **293**, 1289-1292 (2001).
19. D. P. Zipes, J. Jalife, *Cardiac electrophysiology: From cell to bedside.* (2009).
20. D. M. Bers, Cardiac excitation-contraction coupling. *Nature* **415**, 198-205 (2002).
21. P. Connolly, P. Clark, A. S. Curtis, J. A. Dow, C. D. Wilkinson, An extracellular microelectrode array for monitoring electrogenic cells in culture. *Biosens. Bioelectron.* **5**, 223-234 (1990).
22. H. Yan, H. S. Choe, S. Nam, Y. Hu, S. Das, J. F. Klemic, J. C. Ellenbogen, C. M. Lieber, Programmable nanowire circuits for nanoprocessors. *Nature* **470**, 240-244 (2011).
23. J. Goldberger, A. I. Hochbaum, R. Fan, P. Yang, Silicon vertically integrated nanowire field effect transistors. *Nano Lett.* **6**, 973-977 (2006).
24. T. Bryllert, L. Wemersson, L. E. Froberg, L. Samuelson, Vertical high-mobility wrap-gated inas nanowire transistor. *IEEE Electron Device Lett.* **27**, 323-325 (2006).
25. M. Ben-Ishai, F. Patolsky, Wall-selective chemical alteration of silicon nanotube molecular carriers. *J. Am. Chem. Soc.* **133**, 1545-1552 (2011).

## **Part II Nanowire structures for localized optical and electrical device functionalities**

### **Chapter 4 Tapered nanowire structures for localized field-effect transistors and light concentration**

#### **4.1 Introduction**

Precise control of nanowire morphology has spawned novel applications such as nanosensors for biosensing (1-3) and nanoscale power generators for solar energy harvesting (4, 5). Previously, I demonstrated that kinked (1), branched (2), and hollow (6) nanowires can be configured as localized intracellular probes (Chapters 2 and 3). To date, fine control of nanowire morphology, such as the cross-sectional shape, size and aspect ratio, has also been demonstrated to affect optical properties of nanowires (4, 5, 7). For example, by finely tuning the nanowire morphology, absorption spectra of nanowire-based photovoltaic device can be tuned. In this chapter, we report design and controlled synthesis of tapered nanowire structures, with a focus on tapered Ge and core/shell nanowires. We show that the nanoscale modulation of tapering structure affects macroscopic properties of a nanodevice and can be exploited to create novel device functionalities. In particular, we present a comprehensive study of nanowire taper angles at various synthetic conditions in addition to the previously reported studies on the group IV nanowires (8-12). Furthermore, an effort of actively exploiting tapered nanowire structures for novel device functionalities is presented in this chapter, whereas radial over-

coating has been long avoided to maintain uniform electrical and optical properties along the nanowire axis and among devices in previous studies (13-16).

In this chapter, we show that (1) the taper angle of a nanowire is a function of growth temperature, precursor partial pressure and VLS catalyst size and can be precisely controlled and modulated by tuning these parameters; (2) the taper angle affects temporal resolution of nanocone field-effect transistors (NC-FETs) gate-response; (3) tapered Ge/Ag nanowires can be used as waveguide to transport and focus light to the nanowire tip. We demonstrate that fine synthetic control over tapered nanowire structures has the potential to open up new applications in electronics and optics.

## 4.2 Experimental

### 4.2.1 Synthesis of tapered Ge, Si and core/shell nanowires

Tapered Ge nanowires were synthesized by the simultaneous Au nanocluster catalyzed VLS process (17-19) and uncatalyzed radial deposition. First, 10 nm diameter Au nanoclusters (Ted Pella) were dispersed on a Si/SiO<sub>2</sub> substrate (Nova Electronic Materials). For the epitaxial growth, 10 nm diameter Au nanoclusters (Ted Pella) were suspended in a 10% aqueous HF solution and were dispersed on a Si <111> substrate (p-type, Nova Electronic Materials) which was pretreated with BHF (BOE 7:1, J.T. Baker) to remove the native oxide. Next, the nanowire growth was carried out using GeH<sub>4</sub> (20 sccm, 10% in H<sub>2</sub>) with no additional carrier gas for 15-30 min. The total pressures and growth temperatures were set from 10 to 120 Torr and 320 to 400 °C, respectively. The taper angle-modulated structures were synthesized by in-situ modulation of the total pressure or the growth temperature. 10, 30, 50, and 100 nm diameter Au nanoclusters (Ted Pella) were used to determine the effect of catalyst size on the taper angle.

Tapered Si [111] nanowires were synthesized by the simultaneous VLS growth and radial deposition on Si <111> substrates (p-type, Nova Electronic Materials) (8, 20). 50 nm diameter Au nanoclusters (Ted Pella) were suspended in a 10% aqueous HF solution and dispersed on Si <111> substrates pretreated with BHF (BOE 7:1, J.T. Baker) to remove the native oxide. The epitaxial nanowire growth was carried out using SiH<sub>4</sub> (1-2 sccm), B<sub>2</sub>H<sub>6</sub> (7-14 sccm) and H<sub>2</sub> (2-4 sccm) for 20 min (with a constant ratio of reactant and carrier gases for all the growths). The total pressure and growth temperature ranged from 5 to 40 Torr and 450 to 530 °C, respectively (with a 30 s nucleation step at 500 °C when the growth temperature is below 500 °C).

For the tapered core/shell nanowires, tapered Ge/Si nanowires were synthesized in situ by growing epitaxial Si shell on the tapered Ge core by uncatalyzed decomposition of SiH<sub>4</sub> (1 sccm) and B<sub>2</sub>H<sub>6</sub> (10 sccm, 100 ppm in H<sub>2</sub>) at a total pressure of 20 Torr and temperature of 475°C for 17 min, followed by an annealing step at 600 °C for 1h under vacuum ( $5.5 \times 10^{-3}$  Torr). Tapered Ge/Ag nanowires were synthesized by deposition of Ag (100 nm) to the epitaxially-grown tapered Ge [111] nanowires on Si <111> substrate using sputter deposition (AJA International).

Taper angle of Ge nanowires was modeled based on previously reported kinetic models for VLS growths and reaction-rate-limited shell growths.(21, 22) The modeled taper angles were approximated with  $\theta/2 \approx \tan(\theta/2) = R_r/R_a$  assuming  $\theta$  is small.  $R_r$  and  $R_a$  are the radial growth rate ( $R_r = A \cdot \exp(-E_a/RT)$ ;  $E_a$ : activation energy;  $R$ : the gas constant) and the axial VLS growth rate ( $R_a = B \cdot P_{\text{GeH}_4}^2 / (P_{\text{GeH}_4} + C) \cdot T^{-1/2}$ ;  $B$ ,  $C$ : constants), respectively.

#### **4.2.2 Fabrication of nanocone field-effect transistors**

The nanocone field-effect transistors (NC-FETs) were fabricated on Si/SiO<sub>2</sub> substrates (n-type, 0.005 V·cm, Nova Electronic Materials). Tapered Ge/Si core/shell nanowires were sonicated off the growth substrate and were suspended in isopropyl alcohol. The silicon substrate was then coated with SU-8 resist (2000.5, MicroChem Corp.), on which the nanowire suspension was drop-cast as previously described (6). After exposure with electron beam lithography (EBL) and curing of the SU-8 resist layer, source/drain (S/D) metal contacts were defined by EBL and thermal evaporation of Ti/Pd (2/500 nm). The top SU-8 passivation layer (2002, MicroChem Corp.) was subsequently defined by EBL and cured. Etching of the tapered Ge core in hydrogen peroxide (30% H<sub>2</sub>O<sub>2</sub>, Sigma, 65 °C, 60 min) yielded NC-FETs.

#### **4.2.3 Electrical characterizations of nanocone field-effect transistors**

Water-gate voltage ( $V_{wg}$ ) was applied to NC-FETs by a Ag/AgCl reference electrode in  $1\times$  PBS solution. The S/D current, driven by 100 mV source voltage, was amplified by a current preamplifier (1211, DL Instruments) at sensitivity of  $10^{-6}$  or  $10^{-7}$  A/V, filtered (30 kHz, CyberAmp 380, Molecular Devices, Inc.), and digitized at 250 kHz sampling rate (Axon Digidata 1440A Data Acquisition System, Molecular Devices, Inc.). Bandwidths of the NC-FET devices were calculated from the step response to an input  $V_{wg}$  step-function (0 V to +0.1 V, 0.02-0.1 ms rise time). In particular, the device bandwidth (BW) is calculated by  $BW \cdot t_r = 0.35$  where  $t_r$  is the rise time (10% to 90%) of the device response.

#### **4.2.4 Optical characterizations of tapered Ge/Ag core/shell nanowires**

As-synthesized tapered Ge/Ag nanowires were shear-transferred to a  $\text{SiO}_2$  substrate (600 nm thermal oxide). Base-ends of the nanowires were pumped by a focused continuous wave (CW) diode laser (670 nm) with a  $\sim 3.8$   $\mu\text{m}$  spot size using a  $\times 40$  microscope objective lens with a numerical aperture (N.A.) of 0.65. Optical images of the nanowires were collected and recorded by a CCD camera.

## 4.3 Results and discussion

### 4.3.1 Nanowire synthesis and material characterizations

Tapered Ge nanowires were synthesized with control of the taper angle ( $\theta$ ), which is determined by ratio of the radial growth rate to the axial growth rate (VLS growth mechanism) (**Fig. 4.1A**). SEM characterization of an as-synthesized tapered Ge nanowire shows the nanowire is tapered ( $\theta = 5.02^\circ$ ) and has clear surface facets (**Fig. 4.1B**). Angled-view SEM image of the nanowire base shows the nanowire has a hexagonal cross-section (**Fig. 4.1B, inset**). As the axial and radial growth rates depend on growth temperature and precursor partial pressure, fine control of the taper angle can be achieved by tuning these growth conditions (**Fig. 4.1C and D**). In particular, the taper angle increased as the growth temperature was increased, whereas it decreased as the precursor partial pressure was increased. We note that the taper angle also depends on the catalyst size, a trend that is consistent with previous reports of larger VLS growth rate for larger Au catalysts (**Fig. 4.2**) (23).



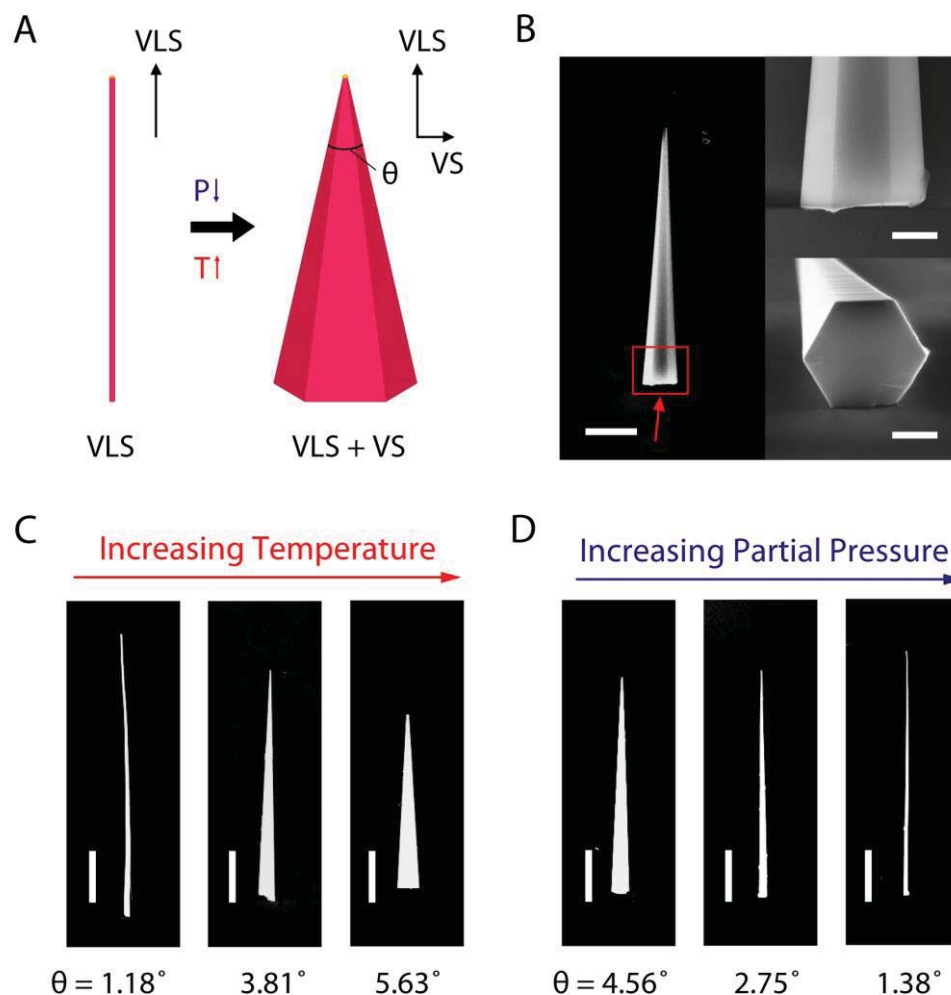


**Figure 4.1 Design and synthesis of tapered nanowires.** (A) Schematics illustration of the synthesis of the tapered nanowire structures where the relative rates of axial vs. radial growth determines the taper angle  $\theta$ . (B) Plan view SEM image of a tapered Ge nanowire shear transferred to a silicon substrate. Scale bar, 2  $\mu\text{m}$ . Insets, high magnification plan view (top) and end-on view (bottom; viewing angle specified by the red arrow) SEM images of the nanowire base enclosed by the red box. Scale bars, 500 nm for both insets. (C) Plan view SEM images of tapered Ge nanowires with increasing growth temperature (left to right: 330 °C, 385 °C and 400 °C; constant GeH<sub>4</sub> partial pressure at 8 Torr). Scale bars, 2  $\mu\text{m}$ . (D) Plan view SEM images of tapered Ge nanowires with increasing precursor partial pressure (left to right: GeH<sub>4</sub> partial pressure 1 Torr, 2 Torr, 8 Torr; constant growth temp at 345 °C). Scale bars, 2  $\mu\text{m}$ .

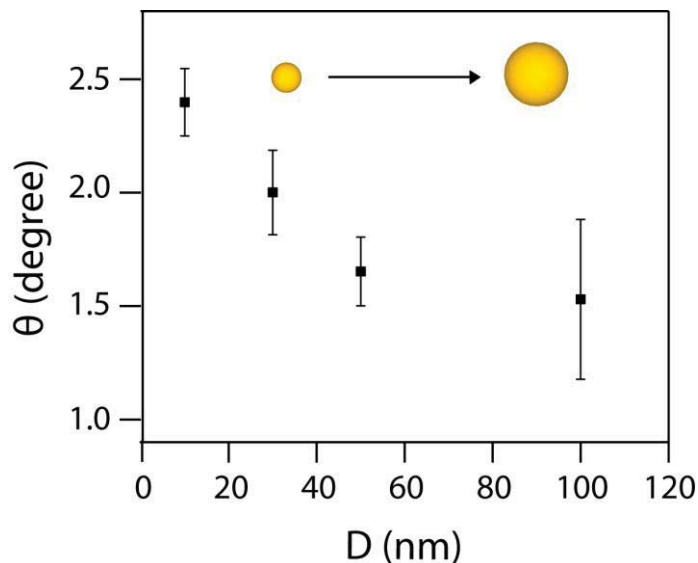


**Figure 4.2 Taper angle of Ge nanowires as function of catalyst size.** Taper angle ( $\theta$ ) of Ge nanowires as a function of Au catalyst size ( $D$ ). Error bars denote one standard deviation from the average. The growth temperature and  $\text{GeH}_4$  partial pressure were maintained at 345 °C and 8 Torr, respectively.

As a function of growth temperature and precursor partial pressure, the taper angle of Ge nanowires can be predicted by a model for axial/radial growth rates. As describe earlier, we calculated the taper angles using kinetic models for the axial and radial growth rates. As a general trend, higher temperature and lower precursor partial pressure are predicted to increase the taper angle, matching our experimental observations (**Fig. 4.3A**). At relatively low temperature (<370 °C) and high precursor partial pressure (>40 Torr), the averaged experimental taper angle values generally fall into a  $\pm 20\%$  range from the predicted values. However, at high temperature (> 400 °C) and low precursor pressure (<20 Torr), we see a

larger deviation from the model. At these conditions, precursors are rapidly depleted as they flow along the growth chamber and growth substrate, suggesting a transition to the mass-transport regime from the reaction rate limited one (21). Thus, we hypothesize that deviations from the model at high temperature and low precursor partial pressure are due to that the radial growth moves into mass transport limited regime while our model assumes the radial growth to be reaction rate limited.

Exploiting the ability to precisely control the taper angles based on the various growth parameters as just described, we can synthesize nanowires of axially modulated taper angle with in-situ variation of growth temperature and precursor pressure. For example, an in-situ decrease of growth temperature (350 to 260 °C with 40 min ramp time) forms a thin nanowire tip due to the decreasing taper angle (1.65° to about 0°, **Fig. 4.3B**). On the other hand, an in-situ decrease of the precursor partial pressure (8 Torr to 1 Torr with 1 min ramp time) forms a tip of larger tapering due to increasing taper angle (1.36° to 4.28°, **Fig. 4.3C**). With the final control of nanowire diameters along the growth direction, these modulated structures could be exploited for unique electronic and optical properties.

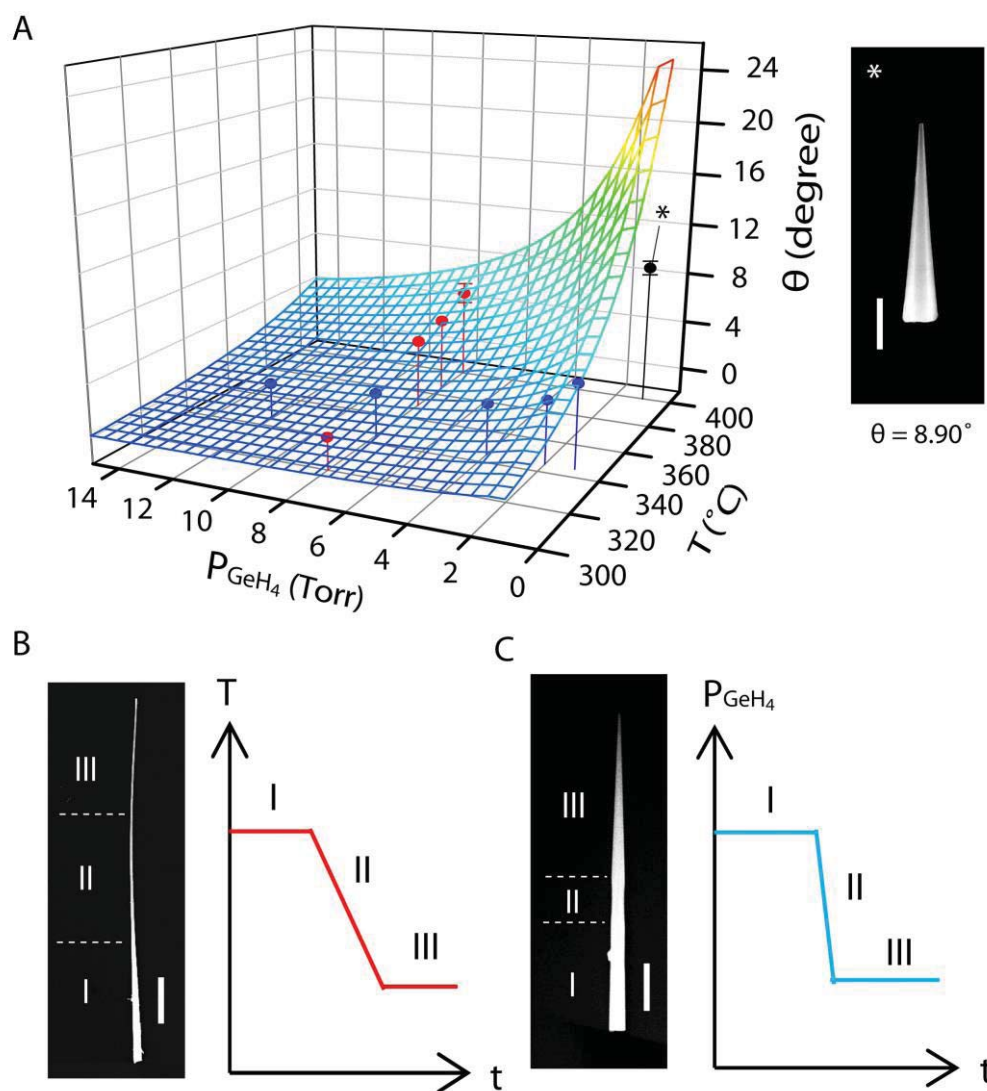


**Figure 4.3 Synthetic control and modulation of Ge nanowire taper angles.** (A) Left, 3-D plot of experimental and modeled taper angles as a function of growth temperature ( $T$ ) and  $\text{GeH}_4$  partial pressure ( $\text{P}_{\text{GeH}_4}$ ). The red and blue point series represent experimental nanowire taper angles at varied  $T$  and  $\text{P}_{\text{GeH}_4}$ , respectively. Error bars denote one standard deviation from the average; in most cases, the error bars are contained within the averaged values. The colored surface plot represents the calculated taper angles based on a kinetic model for radial and axial growths. Right, Ge nanowire grown at the extreme growth conditions specified by “\*”. Scale bar, 500 nm. (B) Plan view SEM image of a Ge nanowire with modulated taper grown by decreasing

**Figure 4.3 (Continued):** growth temperature ( $T$ ) in situ from 350 (20 min, I) to 260 °C (20 min, III) over a 40 min ramp time (II) with constant  $\text{GeH}_4$  partial pressure at 8 Torr. Scale bar: 2  $\mu\text{m}$ . (C) Plan view SEM image of a Ge nanowire with modulated taper grown by decreasing  $\text{GeH}_4$  partial pressure ( $P_{\text{GeH}_4}$ ) from 8 (20 min, I) to 1 Torr (30 min, III) over a 1.5 min ramp time (II) with constant growth temperature at 345 °C. Scale bar, 2  $\mu\text{m}$ .

Synthetic control and modulation of taper angle is general and achievable with other types of VLS-grown nanowires. For example, taper angle of Si [111] nanowires is also a function of growth temperature and  $\text{SiH}_4$  partial pressure and can be similarly controlled. The Si nanowire taper angle increases as the growth temperature increases, whereas it decreases as the precursor partial pressure increases (**Fig. 4.4A**). Similarly, we can synthesize Si [111] nanowires with axially modulated taper angle by in-situ variation of these growth conditions (**Fig. 4.4B**). The average taper angles as function of growth temperature and  $\text{SiH}_4$  partial pressure are shown in **Fig. 4.4C and D**. We note that epitaxially grown Si [111] nanowires were chosen for the taper studies in order to avoid additional effects introduced by different growth directions and surface faceting.

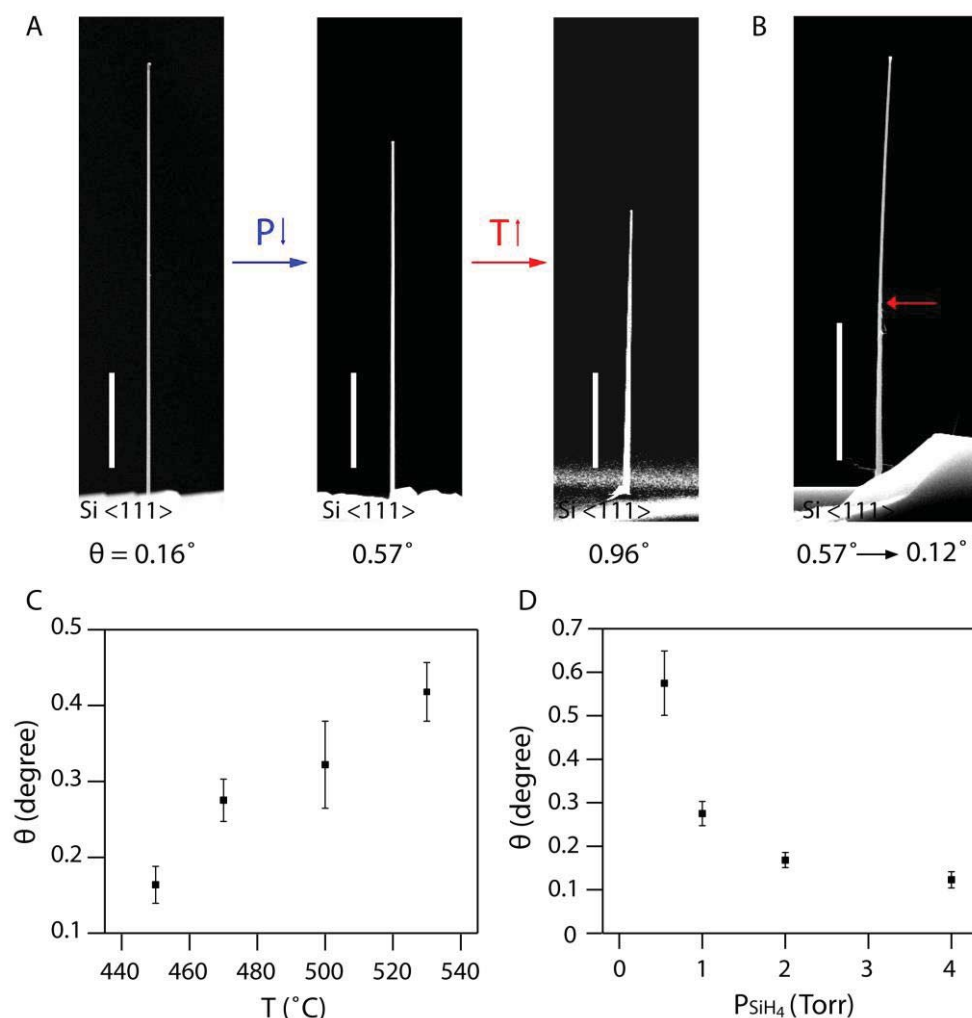


**Figure 4.4 Synthetic control and modulation of Si <111> nanowire taper angles.** (A) Tilted view SEM images (horizontal to Si <111> substrates) of tapered Si nanowires (left to right: growth temperature 470 °C, 470 °C and 530 °C; SiH<sub>4</sub> partial pressure 2 Torr, 0.5 Torr and 0.5 Torr). Scale bars, 2  $\mu$ m. (B) Tilted view SEM images (horizontal to Si <111> substrates) of Si nanowires with modulated taper grown by increasing SiH<sub>4</sub> partial pressure ( $P_{SiH_4}$ ) from 0.5 (10 min) to 4 Torr (1.5 min) over a 40 s ramp time with constant growth temperature at 470 °C. The arrow shows where the taper modulation starts. Scale bar, 2  $\mu$ m (C) Plot of taper angle vs. growth temperature ( $T$ ) of Si nanowires grown epitaxially on Si <111> substrates. Error bars denote one standard deviation from the average. The SiH<sub>4</sub> partial

**Figure 4.4 (Continued):** pressure was maintained constant at 1 Torr. **(D)** Plot of taper angle vs.  $\text{SiH}_4$  partial pressure ( $P_{\text{SiH}_4}$ ) of Si nanowires grown epitaxially on Si  $\langle 111 \rangle$  substrates. Error bars denote one standard deviation from the average. The growth temperature was maintained constant at 470 °C.

Tapered nanowires can serve as a template for synthesis of tapered core/shell nanowire structures for a wide range of electrical and optical applications. For example, highly crystalline Si can be grown epitaxially on the tapered Ge core, forming a conformal tapered Si shell (**Fig. 4.5A and B**). HRTEM characterization reveals an epitaxial relationship at the Ge/Si core/shell interface (**Fig. 4.5C**). As previously reported (24), misfit dislocations are observed to relax stress from lattice mismatch near the interfaces. Importantly, selective area electron diffraction (SAED) studies confirm the single crystalline nature of the Ge core and the epitaxial relationship between the Ge core and Si shell (**Fig. 4.5D**). In particular, SAED patterns from both the Ge core and Si shell show that the diffraction patterns of the core and the shell match in zone axis and crystal orientation, confirming the epitaxial relationship. The diffraction patterns from the shell-only region, which was prepared by partial etching of the Ge core, confirm that the crystal orientation from the Ge core is maintained throughout the Si shell. The observed  $[211]$  zone axis for the horizontally oriented nanowire confirms a  $[111]$  growth direction for the Ge (on a Si/SiO<sub>2</sub> substrate). We note that the transferred nanowire is likely to lie on one of its faceted surfaces which are approximately parallel to  $\{211\}$  planes (with few degrees of deviation caused by the tapering).

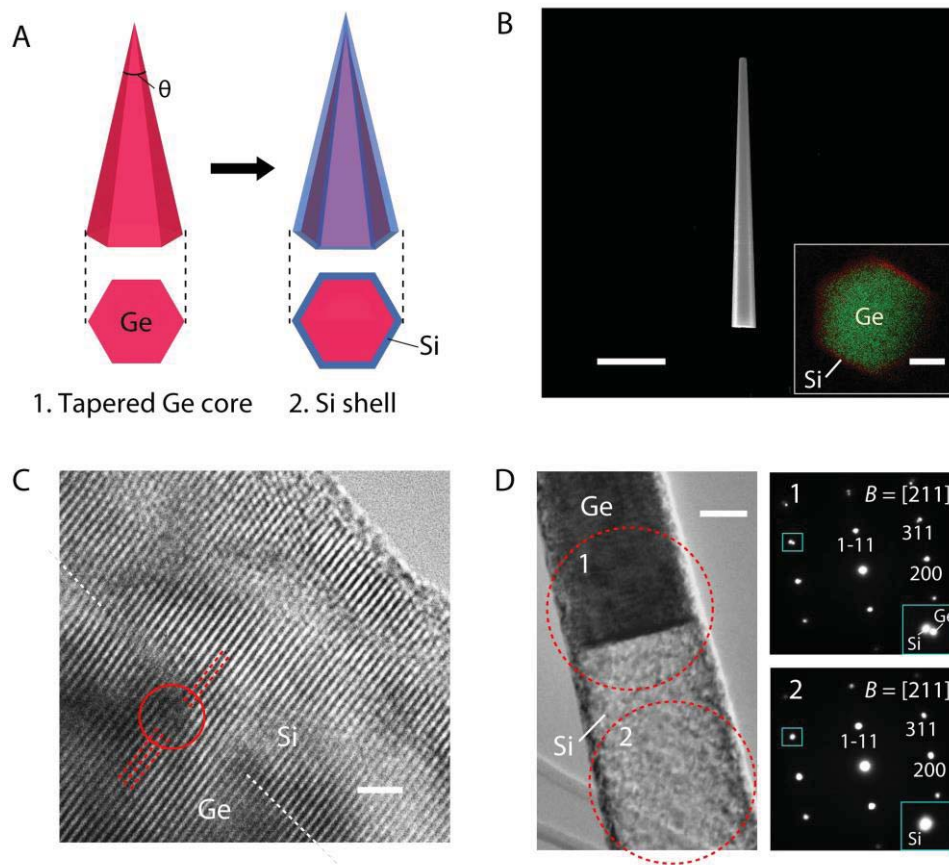


**Figure 4.5 Synthesis of tapered Ge/Si core/shell nanowires.** (A) Schematic illustration of the design and synthesis of the tapered Ge/Si core/shell nanowires (with taper angle  $\theta$ ). (B) Plan view SEM image of a tapered Ge/Si core/shell nanowire shear transferred to a Si/SiO<sub>2</sub> substrate. Scale bar, 2  $\mu$ m. Inset, energy dispersive spectrometry (EDS) elemental mapping of the tapered Ge/Si core/shell nanowire cross-section. Green: Ge K line, red: Si K line. Scale bar, 200 nm. (C) High magnification, aberration-corrected TEM image of the Si shell grown on the tapered Ge core and the Ge/Si interface. The red circle shows a misfit dislocation near the interface due to the Ge-Si lattice mismatch. Scale bar, 2 nm. (D) TEM image of a tapered Ge/Si nanowire with Ge core partially etched with H<sub>2</sub>O<sub>2</sub> aqueous solutions. Scale bar, 50 nm. Insets, SAED pattern of the circled Ge/Si core/shell (top) and Si shell (bottom) regions. The diffraction insets show an enlarged view of the boxed [311] spots.



#### 4.3.2 Electrical properties of the nanocone field-effect transistors

We further fabricated Ge/Si core/shell nanowires into hollow nanocone field effect transistors (NC-FETs) and investigated the device performance dependence on the taper angle. NC-FETs were fabricated by transferring tapered Ge/Si core/shell nanowires to Si/SiO<sub>2</sub> substrates and definition of two metal contacts (Ti/Pd) (3). The S/D contacts and the nanowire region in between the contacts are passivated with SU-8 resist for electrical isolation. The Ge core is then etched in H<sub>2</sub>O<sub>2</sub> solution, which is exchanged to electrolyte (1× PBS) after the etching. The gate voltage ( $V_{wg}$ ), which was applied to the electrolyte through a Ag/AgCl reference electrode, gates the inner wall of the tapered hollow Si nanotube (**Fig. 4.6A**).

After the Ge core etching, the NC-FET devices show a ~130 times increase in sensitivity, as the gate voltage can reach the region between the S/D contacts (**Fig. 4.6B**). In a detailed analysis of pulsed water-gate responses, a NC-FET with a taper angle of 3.33° achieves better device performance compared with its non-tapered counterpart. Of eight devices fabricated with the same process, the tapered NC-FETs consistently show higher bandwidths as well as better S/N ratio compared with non-tapered devices (**Fig. 4.6C and D**) (3). The better temporal resolution of NC-FET in response to the applied pulse is most likely due to that the tapered geometry reduces the RC effect of the electrolyte inside the tube, which effectively functions as a low-pass filter (2). Importantly, the NC-FET device bandwidth increases from <1 kHz to 12 kHz as the taper angle is increased from 0.05° to 5.03° (**Fig. 4.6E**). On the other hand, the smaller noise level of the tapered NC-FET device is likely due to the higher crystallinity of the Si shells compared with the poly-crystalline Si shells on non-tapered core (3). We hypothesize

that higher crystallinity decreases fluctuations of mobility and carrier numbers near the grain boundaries and therefore reduces the low frequency noise (25).

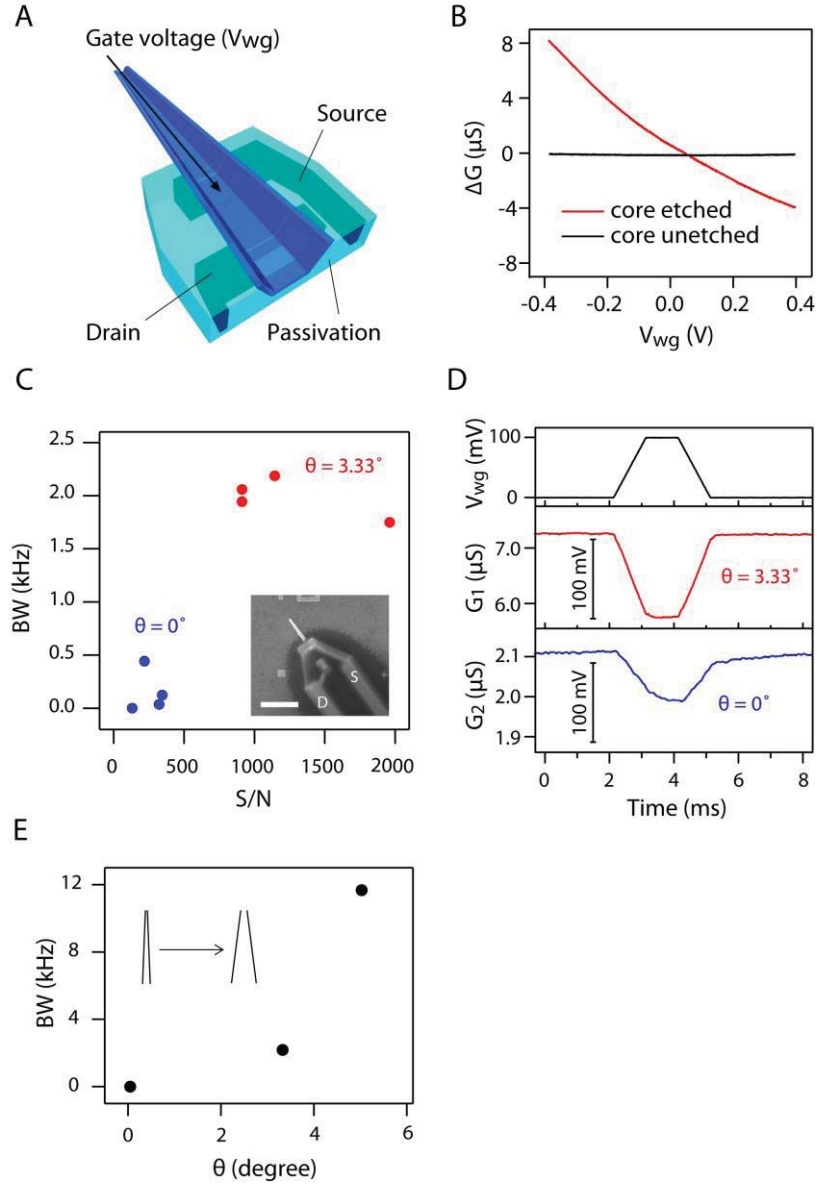


**Figure 4.6 Electrical characterizations of nanocone-FETs (NC-FETs).** (A) Tiled view schematic illustration of the NC-FET device structure fabricated from a tapered Ge/Si core/shell nanowire. (B) Change of device conductance ( $\Delta G$ ) before and after the Ge core

**Figure 4.6 (Continued):** etching. (C) Device bandwidth (BW) and signal-to-noise (S/N) ratio of NC-FETs and non-tapered counterparts. The tip inner diameters for the NC-FETs and non-tapered devices are 65/69/90/106 and 64/68/86/123 nm, respectively. The nanotube length is 4.5  $\mu\text{m}$  for all the devices. Inset, SEM image of a representative NC-FET. Scale bar, 5  $\mu\text{m}$ . (D) Pulsed water-gate response (1 ms rise time) of a tapered NC-FET ( $G_1$ ) and a non-tapered device ( $G_2$ ) with similar nanowire tip size (inner diameter 65 nm) and nanotube length (4.5  $\mu\text{m}$ ). (E) Device bandwidths (BW) of NC-FETs for varied taper angles. The size of the opening at the tip (inner diameter) is 130-140 nm for all the three devices measured.

### 4.3.3 Optical properties of tapered Ge/metal core/shell nanowires for guidance and concentration of light

In order to couple in light to the tapered nanowire structure, a Ag shell was deposited on the as-synthesized tapered Ge nanowire by sputtering as described earlier (**Fig. 4.7A and B**). For optical characterization, a laser spot was focused to the base end of the tapered Ge/Ag core/shell nanowires which were shear-transferred to a Si/SiO<sub>2</sub> substrate (**Fig. 4.7C, left**). Upon illumination, a bright spot was observed at the nanowire tip, suggesting that light can be coupled in and waveguided to the nanowire tip in the tapered Ge/Ag core/shell nanowires (**Fig. 4.7C, right**). Consistent with the previously reported device for nanofocusing, the incident laser is expected to be focused at nanowire tip with enhanced amplification due to the tapered structure (26). We are currently investigating the enhancement factor as a function of the nanowire taper angle with both experiments and simulations.

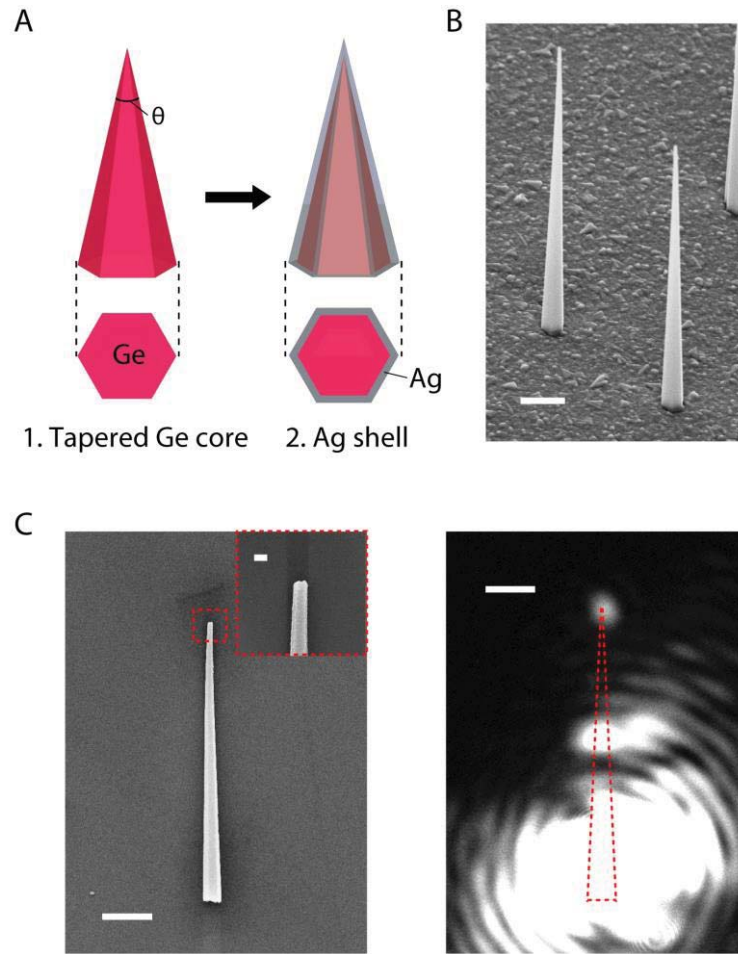


**Figure 4.7 Synthesis and optical characterizations of tapered Ge/Ag core/shell nanowires.** (A) Schematic illustration of the design and synthesis of the tapered Ge/Ag core/shell nanowires (with taper angle  $\theta$ ). (B) Tilted SEM image (45 degree tilt) of the as-synthesized tapered Ge/Ag core/shell nanowires. Scale bar, 2  $\mu\text{m}$ . (C) SEM image of the tapered Ge/Ag nanowire transferred to Si/SiO<sub>2</sub> substrate (left) and the optical image of the same nanowire with a laser spot (670 nm; spot size  $\sim 3.8 \mu\text{m}$ ) focused on the base end (right). Scale bars, 2  $\mu\text{m}$ . Inset, SEM image of the nanowire tip (red box). Scale bar, 200 nm.

## 4.4 Conclusion and outlook

In this report, we carried out a systematic study to synthetically control Ge and Si nanowire taper angles. By depositing Si and Ag shells to tapered nanowire cores, we achieved novel electrical and optical functionalities which have potential applications in sensing, waveguiding and nanofocusing. Future work remains in using, for example, the NC-FETs for high spatio-temporal resolution intracellular recordings from biological cells. In addition, the tapered Ge/Ag nanowires can be used to guide and concentrate light for optical applications such as nanofocusing, plasmonic sensors and waveguides. Furthermore, tapered nanowires also find applications in, for example, mechanical sensors (27), photodetectors (28), and thermoelectric power generations (29).

## 4.5 Bibliography

1. B. Z. Tian, T. Cohen-Karni, Q. Qing, X. J. Duan, P. Xie, C. M. Lieber, Three-dimensional, flexible nanoscale field-effect transistors as localized bioprobes. *Science* **329**, 830-834 (2010).
2. X. J. Duan, R. X. Gao, P. Xie, T. Cohen-Karni, Q. Qing, H. S. Choe, B. Z. Tian, X. C. Jiang, C. M. Lieber, Intracellular recordings of action potentials by an extracellular nanoscale field-effect transistor. *Nat. Nanotechnol.* **7**, 174-179 (2012).
3. R. X. Gao, S. Strehle, B. Z. Tian, T. Cohen-Karni, P. Xie, X. J. Duan, Q. Qing, C. M. Lieber, Outside looking in: Nanotube transistor intracellular sensors. *Nano Letters* **12**, 3329-3333 (2012).
4. T. J. Kempa, J. F. Cahoon, S. K. Kim, R. W. Day, D. C. Bell, H. G. Park, C. M. Lieber, Coaxial multishell nanowires with high-quality electronic interfaces and tunable optical cavities for ultrathin photovoltaics. *Proc. Natl. Acad. Sci. U.S.A.* **109**, 1407-1412 (2012).
5. S. K. Kim, R. W. Day, J. F. Cahoon, T. J. Kempa, K. D. Song, H. G. Park, C. M. Lieber, Tuning light absorption in core/shell silicon nanowire photovoltaic devices through morphological design. *Nano Lett.* **12**, 4971-4976 (2012).
6. R. Gao, S. Strehle, B. Tian, T. Cohen-Karni, P. Xie, X. Duan, Q. Qing, C. M. Lieber, Outside looking in: Nanotube transistor intracellular sensors. *Nano Lett.* **12**, 3329-3333 (2012).
7. L. Y. Cao, P. Y. Fan, E. S. Barnard, A. M. Brown, M. L. Brongersma, Tuning the color of silicon nanostructures. *Nano Lett.* **10**, 2649-2654 (2010).
8. H. Schmid, M. T. Bjork, J. Knoch, H. Riel, W. Riess, P. Rice, T. Topuria, Patterned epitaxial vapor-liquid-solid growth of silicon nanowires on si(111) using silane. *J. Appl. Phys.* **103**, 024304 (2008).
9. N. J. Quitoriano, M. Belov, S. Evoy, T. I. Kamins, Single-crystal, si nanotubes, and their mechanical resonant properties. *Nano Lett.* **9**, 1511-1516 (2009).
10. J. H. Jung, H. S. Yoon, Y. L. Kim, M. S. Song, Y. Kim, Z. G. Chen, J. Zou, D. Y. Choi, J. H. Kang, H. J. Joyce, Q. A. Gao, H. H. Tan, C. Jagadish, Vertically oriented epitaxial germanium nanowires on silicon substrates using thin germanium buffer layers. *Nanotechnology* **21**, 295602 (2010).
11. Y. L. Chueh, Z. Y. Fan, K. Takei, H. Ko, R. Kapadia, A. A. Rathore, N. Miller, K. Yu, M. Wu, E. E. Haller, A. Javey, Black ge based on crystalline/amorphous core/shell nanoneedle arrays. *Nano Lett.* **10**, 520-523 (2010).

12. S. A. Dayeh, A. V. Gin, S. T. Picraux, Advanced core/multishell germanium/silicon nanowire heterostructures: Morphology and transport. *Appl. Phys. Lett.* **98**, 163112 (2011).
13. C. Yang, Z. H. Zhong, C. M. Lieber, Encoding electronic properties by synthesis of axial modulation-doped silicon nanowires. *Science* **310**, 1304-1307 (2005).
14. I. Kimukin, M. S. Islam, R. S. Williams, Surface depletion thickness of p-doped silicon nanowires grown using metal-catalysed chemical vapour deposition. *Nanotechnology* **17**, S240-S245 (2006).
15. J. H. Kim, S. R. Moon, H. S. Yoon, J. H. Jung, Y. Kim, Z. G. Chen, J. Zou, D. Y. Choi, H. J. Joyce, Q. Gao, H. H. Tan, C. Jagadish, Taper-free and vertically oriented ge nanowires on ge/si substrates grown by a two-temperature process. *Cryst. Growth Des.* **12**, 135-141 (2012).
16. B. S. Kim, M. J. Kim, J. C. Lee, S. W. Hwang, B. L. Choi, E. K. Lee, D. Whang, Control of lateral dimension in metal-catalyzed germanium nanowire growth: Usage of carbon sheath. *Nano Lett.* **12**, 4007-4012 (2012).
17. L. J. Lauhon, M. S. Gudiksen, C. L. Wang, C. M. Lieber, Epitaxial core-shell and core-multishell nanowire heterostructures. *Nature* **420**, 57-61 (2002).
18. B. P. Timko, Semiconductor nanowire devices: Novel morphologies and applications to electrogenic biological systems. Harvard University (2009).
19. M. Ben Ishai, F. Patolsky, Shape- and dimension-controlled single-crystalline silicon and sige nanotubes: Toward nanofluidic fet devices. *J. Am. Chem. Soc.* **131**, 3679-3689 (2009).
20. J. H. Woodruff, J. B. Ratchford, I. A. Goldthorpe, P. C. McIntyre, C. E. D. Chidsey, Vertically oriented germanium nanowires grown from gold colloids on silicon substrates and subsequent gold removal. *Nano Letters* **7**, 1637-1642 (2007).
21. J.-H. Park, T. S. Sudarshan, *Chemical vapor deposition*. (ASM International, 2001).
22. H. Z. Zhao, S. Zhou, Z. Hasanali, D. W. Wang, Influence of pressure on silicon nanowire growth kinetics. *Journal of Physical Chemistry C* **112**, 5695-5698 (2008).
23. F. Dhalluin, T. Baron, P. Ferret, B. Salem, P. Gentile, J. C. Harmand, Silicon nanowires: Diameter dependence of growth rate and delay in growth. *Appl. Phys. Lett.* **96**, 133109 (2010).
24. M. Y. Gutkin, I. A. Ovid'ko, A. G. Sheinerman, Misfit dislocations in wire composite solids. *J. Phys. -Condens. Mat.* **12**, 5391-5401 (2000).

25. M. Rahal, M. Lee, A. P. Burdett, Flicker noise in gate overlapped polycrystalline silicon thin-film transistors. *IEEE T. Electron. Dev.* **49**, 319-323 (2002).
26. H. Choo, M.-K. Kim, M. Staffaroni, T. J. Seok, J. Bokor, S. Cabrini, P. J. Schuck, M. C. Wu, E. Yablonovitch, Nanofocusing in a metal-insulator-metal gap plasmon waveguide with a three-dimensional linear taper. *Nat. Photon.* **6**, 838-844 (2012).
27. O. Malvar, E. Gil-Santos, J. J. Ruz, D. Ramos, V. Pini, M. Fernandez-Regulez, M. Calleja, J. Tamayo, A. San Paulo, Tapered silicon nanowires for enhanced nanomechanical sensing. *Appl. Phys. Lett.* **103**, 033101 (2013).
28. C. J. Kim, H. S. Lee, Y. J. Cho, K. Kang, M. H. Jo, Diameter-dependent internal gain in ohmic ge nanowire photodetectors. *Nano Lett.* **10**, 2043-2048 (2010).
29. J. Moon, J. H. Kim, Z. C. Y. Chen, J. Xiang, R. K. Chen, Gate-modulated thermoelectric power factor of hole gas in ge-si core-shell nanowires. *Nano Lett.* **13**, 1196-1202 (2013).



# Chapter 5 Tip-modulated nanowire structures for localized electrical and optical functionalities

## 5.1 Introduction

Structural diversity and synthetic tunability of nanowires have enabled diverse functionalities to be encoded in the one-dimensional nanostructure (1). As described in Chapter 1, a handful of fundamental nanowire structural motifs, including the axial, radial and kinked modulations, have been reported (2-5). These basic modulations have enabled incorporate electrical and optical device elements in the nanowire structure (6-18). For example, an axial p-n junction nanowire can function as a nanoscale photon source for optoelectronic circuits (2). A radially modulated p-i-n core/shell nanowire can serve as an efficient photovoltaic energy conversion element to power nanoelectronic sensors and logic gates (10). A nanoFET localized near a nanowire kink can protrude into a biological cell to record intracellular signals when configured into a three-dimensional device geometry (6). However, in all these structures, the encoded functionalities either extend through the whole nanowire or require additional electrical contacts in proximity, which geometrically prevents the functional elements from locally accessing physical, chemical and biological systems. Consequently, ultra-high spatial resolution and ultra-sensitive inputs or outputs to the device are perturbed by geometrical hindrance and additional signals from other parts of the device. In this chapter, to address these issues, a new nanowire structural motif, which is optimally designed for localization of electrical and optical functionalities at one end of the nanowire, is demonstrated. With spatially resolved electrical and optical characterizations,

we show that this new nanowire structural motif has a wide range of applications in physical, chemical and biological sciences.

## 5.2 Experimental

### 5.2.1 Synthesis of tip-modulated Si p-n junction nanowires

We first explored bottom-up synthesis of a Si tip-modulated nanowire with a tip p-n junction. For the first step, the epitaxial p-type Si nanowire cores were grown by Au nanocluster catalyzed VLS process on Si <111> substrates (p-type, 3-5  $\Omega\cdot\text{cm}$ , Nova Electronic Materials). Next, 50 nm diameter Au nanoclusters (Ted Pella) were suspended in 10% aqueous HF solution and were dispersed on Si <111> substrates, which were pretreated with BHF (BOE 7:1, J.T. Baker) for 10 s. The VLS growth was carried out using  $\text{SiH}_4$  (1-2 sccm),  $\text{B}_2\text{H}_6$  (14 sccm), and  $\text{H}_2$  (4-5 sccm) at total pressure and temperature of 10 Torr and 500  $^\circ\text{C}$ , respectively. Subsequently, a conformal  $\text{SiO}_2$  insulation layer ( $\sim 50$  nm) was deposited with atomic layer deposition (ALD, Savannah-S200, Cambridge NanoTech) at 250  $^\circ\text{C}$ . The growth substrate was then spin-coated with a protective resist layer (SU-8 2005 or 2010, MicroChem Corp., prebaked at 95  $^\circ\text{C}$  for 3 min), which was etched down using oxygen plasma stripper (PJ-II, AST Products Inc., 50 W for 1-2 h) to expose the nanowire tips. Ultrasonication (500D, Crest Ultrasonics) in isopropanol at 120 W for 1 min removed the nanowire tips. The protective resist layer was then removed by rinsing in acetone and the additional cleaning with oxygen plasma stripper (150 W for 1 h). Following the tip removal, the growth substrate was treated with BHF for 4 s and immediately transferred to the CVD chamber. The n-type Si shell growth was carried out by uncatalyzed shell deposition process using  $\text{SiH}_4$  (0.15 sccm),  $\text{PH}_3$  (0.15-0.75 sccm), and  $\text{H}_2$  (60 sccm) at total pressure and temperature of 25 Torr and 775  $^\circ\text{C}$ , respectively.

### 5.2.2 Fabrication of tip-modulated nanowire devices

As-synthesized Si p-n junction tip-modulated nanowires were shear-transferred to SiN<sub>x</sub> substrates (100 nm thermal SiO<sub>2</sub>, 200 nm SiN<sub>x</sub>, n-type, 0.005 V·cm, Nova Electronic Materials). SU-8 (2000.5, MicroChem Corp.) etch mask was defined with electron-beam lithography (EBL) to protect the shell on the tip end of the nanowire. After 6 s etch with BHF to remove the native oxide, the nanowires were etched for 40–60 s with KOH (20 vol.% in water, 60 °C) to remove the n-type Si shell. The SU-8 etch mask was subsequently removed by UV-ozone stripper (300 °C, 40 min). MMA/PMMA resists (MicroChem Corp.) were spin-coated and patterned by EBL for core and shell contacts. The nanowires were etched for 50 s with BHF to remove the SiO<sub>2</sub> layer before thermal evaporation to metalize the contacts (Ti/Pd, 3/450 nm).

### 5.2.3 Generality of tip-modulated nanowire synthesis

The aforementioned synthetic method is general for different combinations of materials for the core, shell and the insulation layer. As an example, we explored synthesis of p-type Si core, SiO<sub>2</sub> insulation layer and CdS shell tip-modulated nanowires. In detail, highly doped Si nanowire cores were epitaxially grown by 50 nm Au nanocluster catalyzed VLS process using SiH<sub>4</sub> (1-2 sccm), B<sub>2</sub>H<sub>6</sub> (14 sccm), and H<sub>2</sub> (4-5 sccm) at total pressure and temperature of 10 Torr and 500 °C on Si <111> substrates (p-type, 3-5 Ω cm, Nova Electronic Materials), as previously described in the synthesis of tip-modulated nanowires with a tip Si p/n junction. The SiO<sub>2</sub> insulation layer (~50 nm) was conformally deposited with atomic layer deposition (ALD, Savannah-S200, Cambridge NanoTech) at 250 °C and the nanowire tip was subsequently removed by ultrasonication as described. Before the SU-8 protection layer removal, the substrate

was briefly treated with BHF for about 30 s to etch back the SiO<sub>2</sub> insulation for 500 nm-1 μm. The CdS shell growth was carried out with physical vapor deposition (PECVD) in a three-zone furnace immediately after brief treatment in BHF (10 s) to remove the nanowire tip oxide. CdS was evaporated at 710 °C from zone one and deposited on the substrate in zone two at 550 °C for 20 minutes.

#### **5.2.4 Electrical and optical characterizations of tip-modulated nanowires**

I-V characteristics of the tip-modulated nanowire devices were measured with a probe station (TTP-4, Desert Cryogenics) and a DAC card (PCI-6030E, National Instruments, Inc.) under computer controls and with a semiconductor parameter analyzer (4156 C, Agilent Technologies). Water-gate experiments were carried out with devices submerged in 1× PBS solution with a Ag/AgCl reference electrode to apply gate voltage ( $V_{wg}$ ). The tip-modulated nanowire devices were passivated with PMMA resists (950 C5, 2 layers, MicroChem Corp.). The source-drain current of the device was amplified by a current preamplifier (1211, DL Instruments) at sensitivity of  $10^{-6}$  or  $10^{-7}$  A/V, filtered (60 kHz, CyberAmp 380, Molecular Devices, Inc.), and digitized at 250 kHz sampling rate (Axon Digidata 1440A Data Acquisition System, Molecular Devices, Inc.).

For the scanning photocurrent experiments, a Si p-n junction tip-modulated nanowire device was mounted on a piezo-controlled movable stage (Digital PI PZT flexure stage) to spatially control the nanowire tip position. The device was optically pumped at room temperature by a 488 nm Ar-ion CW laser, which was focused to a spot of ~1.6 μm in diameter using a ×40 microscope objective lens with a numerical aperture (N.A.) of 0.65. The photocurrent was measured under

laser illumination or in the dark using a semiconductor parameter analyzer (4156 C, Agilent Technologies) as the laser spot was aligned to or spatially scanned through the nanowire tip. The device responsivity was obtained from dividing the measured photocurrent by the incident power. The incident power was measured by considering the area fraction of the nanowire within the laser spot as the tip was aligned at the center of the spot.

### **5.2.5 Top-down synthesis and fabrication of tip-modulated nanowires and device arrays**

SU-8 (2002, MicroChem Corp.) resist masks were defined on Si <111> substrate (p-type, 0.001-0.005  $\Omega$  cm, Nova Electronic Materials) by EBL and hard-baked at 180 °C for 20 min. After deep reactive ion etching (DRIE, SPTS Technologies), the substrate was cleaned with oxygen plasma stripper at 150 W for 30 min and the nanowires were thinned down to ~300 nm in diameter with KOH (20 vol.% in water, 60 °C). Subsequent conformal ALD growth of the SiO<sub>2</sub> insulation layer, ultrasonication removal of the nanowire tips, and the conformal n-type Si shell growth, similar to the procedures described in the bottom-up synthesis, yielded tip-modulated nanowire arrays.

To fabricate the chip into the tip-modulated nanowire device array, part of the n-shell was removed by 20 s etch in KOH (20 vol.% in water, 60 °C). The tip-modulated nanowire arrays were protected by a SU-8 (2 layers of 2010) etch mask, which was defined by photolithography, during the etching. The core and shell contact pads were then patterned by EBL or photolithography and the chip was etched locally for 50 s with BHF to remove the SiO<sub>2</sub> layer on the core contact before thermal evaporation (Ti/Pd, 3/120 nm) to metalize both the contact pads. Water-gate measurements were carried out with a probe station (TTP-4, Desert Cryogenics) and

a DAC card (PCI-6030E, National Instruments, Inc.), at a typical ramp rate of 2 mV/s. The gel pH measurements were carried out using 1% agarose gel prepared from phosphate buffers of pH 6, 7 and 8. The device conductance changes were measured with the same set-ups as the water-gate measurements at 2 Hz sampling rate.

## 5.3 Results and discussion

### 5.3.1 Nanowire synthesis and material characterization

In our design of the tip-modulated nanowires, instead of a uniform axial or radial modulation, material compositions and dopant profiles are modulated at the nanowire tip (**Fig. 5.1A**). In particular, the nanowire core and shell, which are insulated from each other by a dielectric layer that extends along the rest of the nanowire, form a tip-localized nanoscale junction. Notably, our structure combines merits of both the axial and radial modulated nanowires: a localized junction, similar to that of an axial junction, and an extended core/shell structure allowing geometrical freedom to define electrical contacts, similar to that of a radial nanowire device, are realized in the same nanowire structure. Further, by selecting different materials for the core, shell and the insulation layer, we can encode different device functionalities at the nanowire tip. In this Chapter, we first focus on rational synthesis and device characterizations of tip-modulated nanowires with a Si p-n junction.



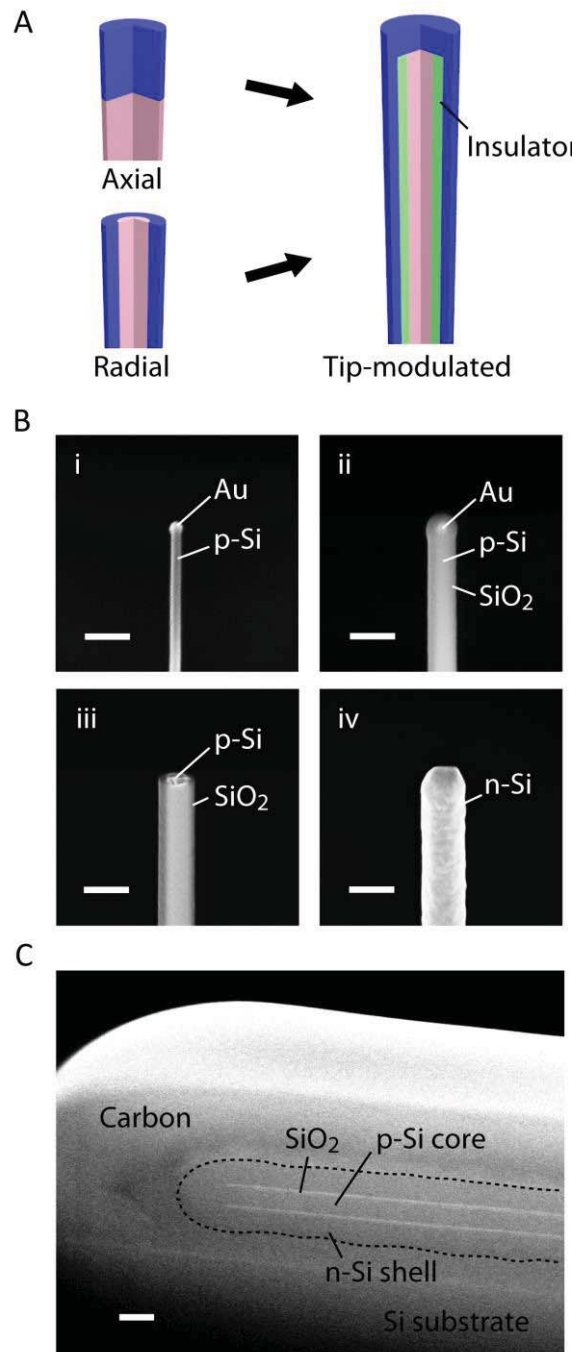


**Figure 5.1 Synthesis of tip-modulated nanowires and material characterizations.** (A) Schematics illustration of the axially, radially modulated (left) and tip-modulated (right) nanowire structures. (B) Synthesis of a tip-modulated nanowire with a Si p-n junction. SEM

**Figure 5.1 (Continued):** images (45 degree tilt) of the same nanowire were taken for each synthetic step: (i) Au nanocluster catalyzed VLS epitaxial nanowire growth of p-type core on Si <111> substrate; (ii) conformal deposition of SiO<sub>2</sub> insulation layer by ALD; (iii) removal of the nanowire tip containing the Au nanocluster by ultrasonication; (iv) conformal growth of n-type shell to form the tip junction. Scale bars, 200 nm. (C) SEM characterizations of the tip junction. The nanowire was longitudinally cross-sectioned by a focused ion beam to show the inner structure after the protective carbon layer deposition. The contour of the nanowire is specified by the broken line. Scale bar, 100 nm.

A two-step chemical vapor deposition (CVD) process consisting of VLS (19) core growth and uncatalyzed shell growth was used to rationally synthesize nanowires with a tip Si p-n junction. First, p-type Si nanowire cores were epitaxially grown on a Si <111> substrate with Au nanocluster catalyzed VLS growth (20, 21) (**Fig. 5.1B, i**). The as-synthesized nanowires were then conformally coated with SiO<sub>2</sub> by atomic layer deposition (ALD) (**Fig. 5.1B, ii**). The growth substrate was spin-coated with a protective resist layer, which was thinned in oxygen-plasma to expose the nanowire tip. After ultrasonication to mechanically remove the nanowire tips protruding from the resist, the protective resist layer was removed by dissolution in acetone and subsequent oxygen-plasma cleaning (**Fig. 5.1B, iii**). Immediately before the transfer of the growth substrate to the CVD chamber, the native oxide on the truncated tip was etched in BHF in order to form a clean tip junction. Finally, a conformal n-type Si shell was deposited in CVD with uncatalyzed shell growth (**Fig. 5.1B, iv**). We note that dopant concentrations and physical dimensions of the core and shell can be finely controlled by tuning the synthetic conditions. In addition, the tip junction area and morphology can be tuned by, for

example, introducing a BHF etching step after the tip-ultrasonication to partially remove the  $\text{SiO}_2$  layer surrounding the nanowire sidewalls near the tip (**Fig. 5.2**).

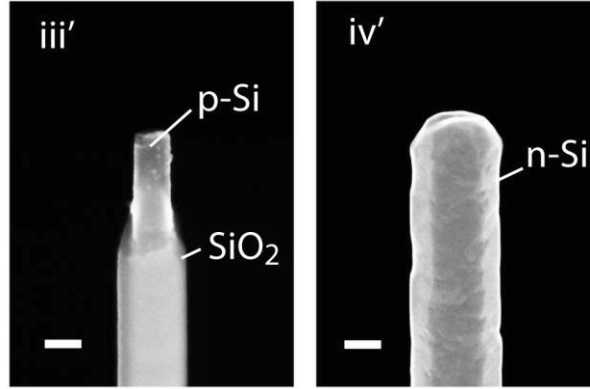


**Figure 5.2 Synthetic variations for the tip-modulated nanowire structure.** The  $\text{SiO}_2$  layer was etched back (for 300-400 nm) with BHF after the tip removal (iii'). Growth of the n-type Si shell yielded the tip-modulated nanowire structure with a different junction morphology (iv'). Scale bars, 100 nm.

The as-synthesized nanowires with the tip Si p-n junction were shear-transferred to a Si substrate and cross-sectioned along the nanowire axis with a focused ion beam for material characterizations. SEM imaging of the cross-section shows that the nanowire core and shell are connected at the tip and that the  $\text{SiO}_2$  insulation layer extends along the rest of the nanowire except for the tip junction (**Fig. 5.1C**). There is no visible interface or contrast difference between the core and shell at the nanowire tip, suggesting a clean and continuous junction. In addition, high resolution transmission electron microscopy (HRTEM) imaging of the junction interface shows that the lattice fringes are continuous from the core to the shell (**Fig. 5.3**). Taken

together, these results suggest that the synthesized tip-modulated nanowires follow our structural design.

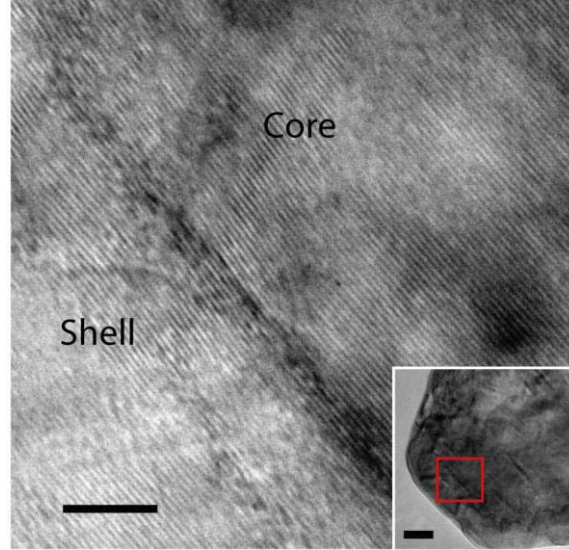


**Figure 5.3 High resolution transmission electron microscope (HRTEM) characterizations of the tip Si p-n junction.** Bright-field HRTEM image of the tip junction interface. Scale bar, 5 nm. Inset, low magnification bright-field TEM image of the nanowire tip area (red box specifying the area of the HRTEM image). The shell thickness is 20-25 nm. Scale bar, 20 nm.

### 5.3.2 Electrical properties of the tip-modulated nanowires

To characterize the electrical properties of the tip p-n junction, tip-modulated nanowire devices were fabricated by defining separate contacts to the core and the shell (**Fig. 5.4**). First, a section of the n-Si nanowire shell was removed by potassium hydroxide (KOH) aqueous solution while the nanowire tip end was protected in SU-8 resist as the etch mask (12). After removing the SU-8 resist mask, core and shell contacts were patterned with EBL. The SiO<sub>2</sub> insulation layer was then

removed in BHF to expose the core, and the contacts were immediately metalized with thermal evaporation. We emphasize that the chemical selectivity for the  $\text{SiO}_2$  insulation layer in the etching steps is essential to the success of the device fabrication. In the first KOH etching step, the etch rate of Si is much faster ( $> 70$  times) than that of  $\text{SiO}_2$  so that the  $\text{SiO}_2$  insulation layer serves as etch top for the nanowire core (22). On the other hand, in the BHF etching, the Si shell is preserved during the  $\text{SiO}_2$  removal as the etch rate of Si is negligible compared to that of  $\text{SiO}_2$ .

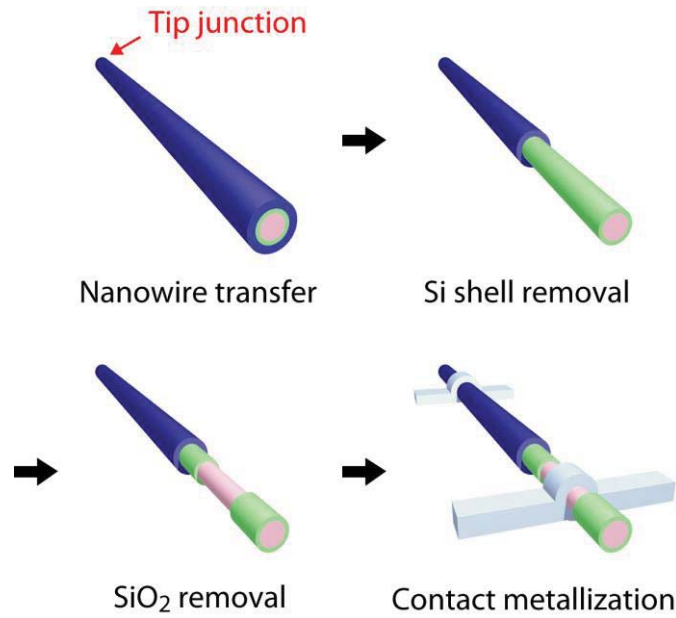


**Figure 5.4 Fabrication of tip-modulated nanowire devices.** Schematic illustration of the step-by-step fabrication of a tip-modulated nanowire device.

To closely study whether the p-n junction is localized at the nanowire tip, we defined one common core contact and two shell contacts—one close to the tip end and the other close to the broken base end, on the same tip-modulated nanowire (p1, n1 and n2 in **Fig. 5.5A**, respectively). We first measured the device I-V characteristics with different combinations of the core and shell

contacts. The device with the common core and the tip end shell contacts (p1-n1) showed diode-like behavior while the control device with the common core and the broken end shell contacts (p1-n2) showed significantly smaller current for the same voltage sweep (**Fig. 5.5B**). This result demonstrates that a p-n junction exists on the tip side and no p-n junction is formed on the broken base side of the nanowire. In addition, we measured the current between the tip end and the broken end shell contacts (n1-n2) with the same voltage sweep. Negligible leakage currents were observed, which further confirms our device structure. Furthermore, a linear fitting to a semi-log device I-V curve yielded an ideality factor of 2.16 and dark saturation current of 0.21 pA for a typical tip p-n junction nanowire device (**Fig. 5.6**). The fitted ideality factor is comparable to that of previously reported axial p-n junction nanowire devices (23) and lower than that of radial p-n junction nanowire devices (10). This suggests that the tip-modulated p-n junction functions as a diode of better or comparable quality to the p-n junctions formed in other nanowire structures.

We further carried out a selective-area water-gate experiment, in which part of the tip-modulated nanowire device was exposed to the electrolyte that served as the top-gate, while the rest of the device was passivated from the solution (**Fig. 5.5C**). At forward bias voltage, the device showed a transconductance of 79.7 nS/V with the quasi-static water-gate sweep. To quantitatively verify the localization of device sensitivity at the nanowire tip, we repeatedly measured the water-gate transconductance of a single device with different exposed nanowire tip lengths (**Fig. 5.5D**). The measurements show that about 90% of the total transconductance (defined as the device transconductance with an exposed tip length of 9.5  $\mu\text{m}$ ) is localized at the 0.5  $\mu\text{m}$  long tip and nearly 100% of the total transconductance is localized at the 1.2  $\mu\text{m}$  long tip. This result is

consistent with previous reports of localized device sensitivity near the p-n junction of a kinked nanowire device (24). We further characterized the device temporal resolution by applying a fast water-gate voltage pulse (rise time down to 0.1 ms) (**Fig. 5.5E**). As a result, the conductance change followed well the applied pulse, suggesting the device can record potential changes with time resolution of at least 0.1 ms (device bandwidth > 3.5 kHz). To summarize, the p-n junction of our tip-modulated nanowire device shows a clear diode-like electrical characteristics and can function as a potentiometric sensor with the device sensitivity localized at the nanowire tip.

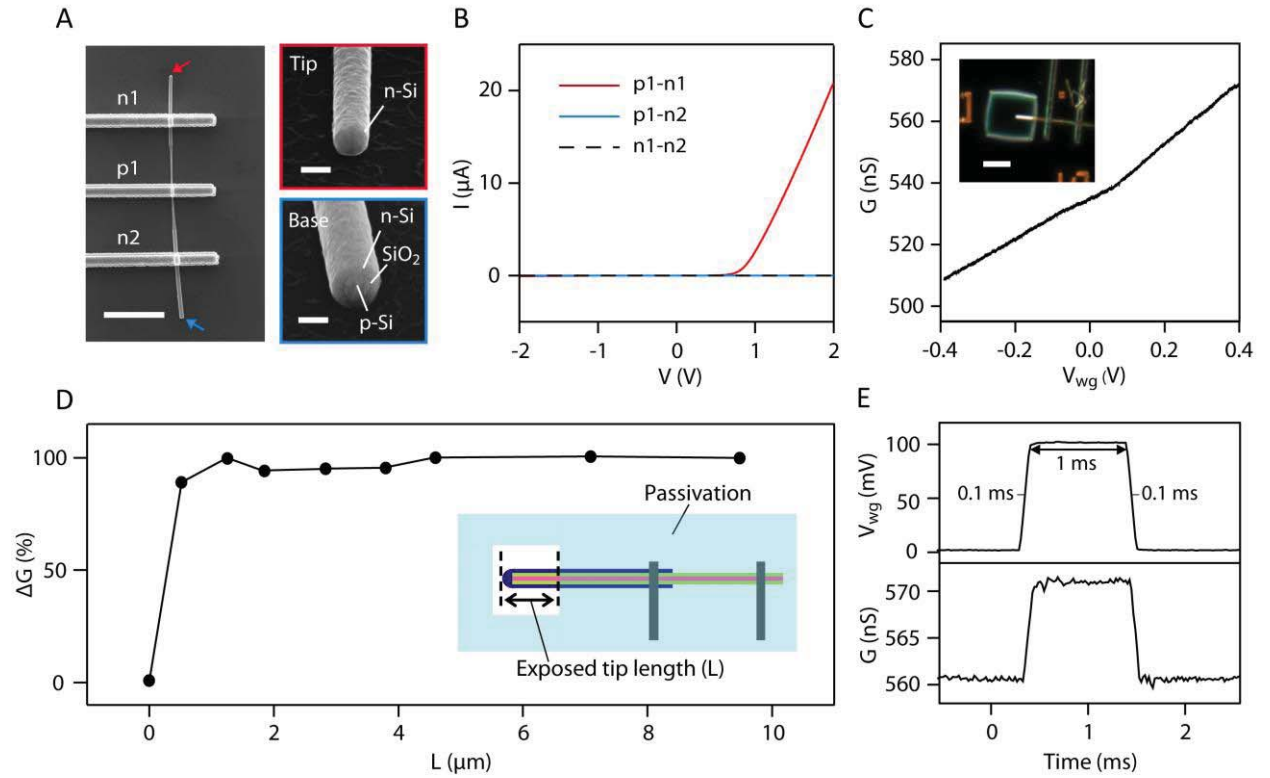


**Figure 5.5 Electrical characterizations of a tip-modulated nanowire device.** (A) SEM characterizations of the tip-modulated nanowire device. Left: SEM image of a tip-modulated nanowire device with one core contact (p1) and two shell contacts (n1 and n2). Scale bar, 5  $\mu\text{m}$ . Right top: high magnification SEM image of the tip end with the p-n junction (red arrow). Scale

**Figure 5.5 (Continued):** bar, 200 nm. Right bottom: high magnification SEM image of the base end with no p-n junction (blue arrow). Scale bar, 200 nm. **(B)** I-V curves were measured between the core-tip end shell (p1-n1), core-base end shell (p1-n2) and tip end shell-base end shell (n1-n2) contacts. **(C)** Water-gate (top-gate) response of the tip-modulated nanowire device. Change of the device conductance ( $G$ ) was recorded while the applied water-gate ( $V_{wg}$ ) was swept from -0.4 to 0.4 V. The devices were forward biased at 1.5 V in all the water-gate measurements. Inset, dark-field optical microscope image of the device with the passivation window. The unpassivated tip length was  $\sim 3.2 \mu\text{m}$ . Scale bar,  $5 \mu\text{m}$ . **(D)** Localized water-gate response from the nanowire tip. Water-gate transconductance ( $\Delta G$ ) of a tip-modulated nanowire device was measured repeatedly while the exposed nanowire tip length ( $L$ ) was changed. The transconductance values were normalized with respect to that from the  $9.5 \mu\text{m}$  nanowire tip ( $28.0 \text{ nS/V} = 100\%$ ). Inset: schematic illustration of the exposed nanowire tip length and passivation configuration. **(E)** Pulsed water-gate response of a tip-modulated nanowire device. The applied water-gate voltage was swept with 0.1 ms rise time (top) while the corresponding device conductance change was recorded (bottom). The unpassivated tip length was  $\sim 3.2 \mu\text{m}$ .

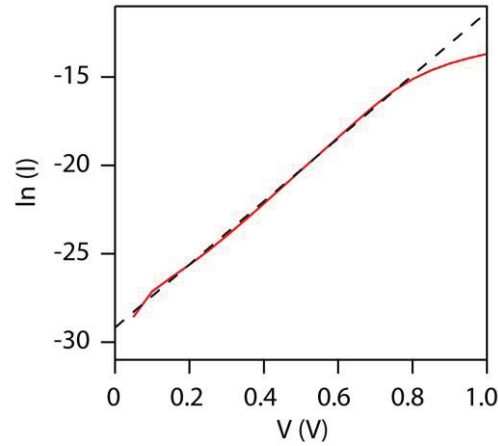


**Figure 5.6 Dark state semi-log ( $\log(I)$ -V) plot of a tip-modulated nanowire device.** The  $\log(I)$ -V plot (red line) is linearly extrapolated (broken black line) to estimate the ideality factor ( $n = 2.16$ ) and the dark saturation ( $I_0 = 0.21 \text{ pA}$ ) current of the device.



### 5.3.3 Optical properties of the tip-modulated nanowires

To show that our tip-modulated nanowire device can function as a localized and highly-sensitive diode photodetector, we carried out scanning photocurrent measurements. The photocurrent was measured with varying incident laser power, incident laser position and device bias voltage. The device mounted on a piezo-controlled movable stage was excited using the Ar-ion laser with a wavelength of 488 nm and a spot size of  $\sim 1.6 \mu\text{m}$  (**Fig. 5.7A**). First, dark and light I-V curves of the device were measured when the laser beam was focused on the nanowire tip where the p-n junction was formed. As a result of light absorption and carrier generation and separation at the tip junction, the illuminated I-V curve showed an open-circuit voltage ( $V_{\text{OC}}$ ) of 0.730 V and short-circuit current ( $I_{\text{SC}}$ ) of 436 nA at an incident power of  $\sim 29.3 \mu\text{W}$  (**Fig. 5.7B**). We also obtained the photocurrent from the I-V curves as functions of different incident power and applied reverse bias voltages (**Fig. 5.7C**). The measured photocurrent reveals several important device features, which are consistent to the previous observations in the axially and radially modulated p-n and p-i-n junction nanowire devices (10, 23): (1) the photocurrent showed a linear dependence on the incident power; (2) the photocurrent increased with the increasing reverse bias voltage. In addition, we estimated the responsivity of the tip-modulated nanowire device (**Fig. 5.7D**). As the incident power decreased, the device responsivity increased up to  $\sim 0.15 \text{ A/W}$ , which is consistent with the trend observed in the previously reported nanowire photodetectors (25). We note that the responsivity of our tip-modulated nanowire photodetector is comparable or larger than the reported values of axially modulated Si p-i-n junction nanowire avalanche

photodetector (typically in the range of mA/V) (25) and is comparable to commercially available p-n diode photodetectors.

Next, we performed spatially resolved photocurrent measurements to investigate spatial dependence of the generated photocurrent. The incident laser spot was line-scanned across the tip-modulated nanowire device with different distances from the tip (step size 300 nm) along the nanowire axis (**Fig. 5.7E**). In the scan going through the nanowire tip, the photocurrent reached maximum when the focused spot was on the tip (**Fig. 5.7F**). As the scan was carried out more distant to the nanowire tip, we observed a sharp decrease of the maximum photocurrent. In particular, the maximum photocurrent measured 2.4  $\mu\text{m}$  away from the tip was >11 times smaller than that measured for the scan going through the tip. Furthermore, the laser spot was scanned on the core/shell or core only regions between the two contacts, in which we observed negligible photocurrents (**Fig. 5.7G**). Taken together, the spatially resolved photocurrent measurement suggests that the photocurrent generation is strongly localized near the nanowire tip, where the localized p-n junction is formed.

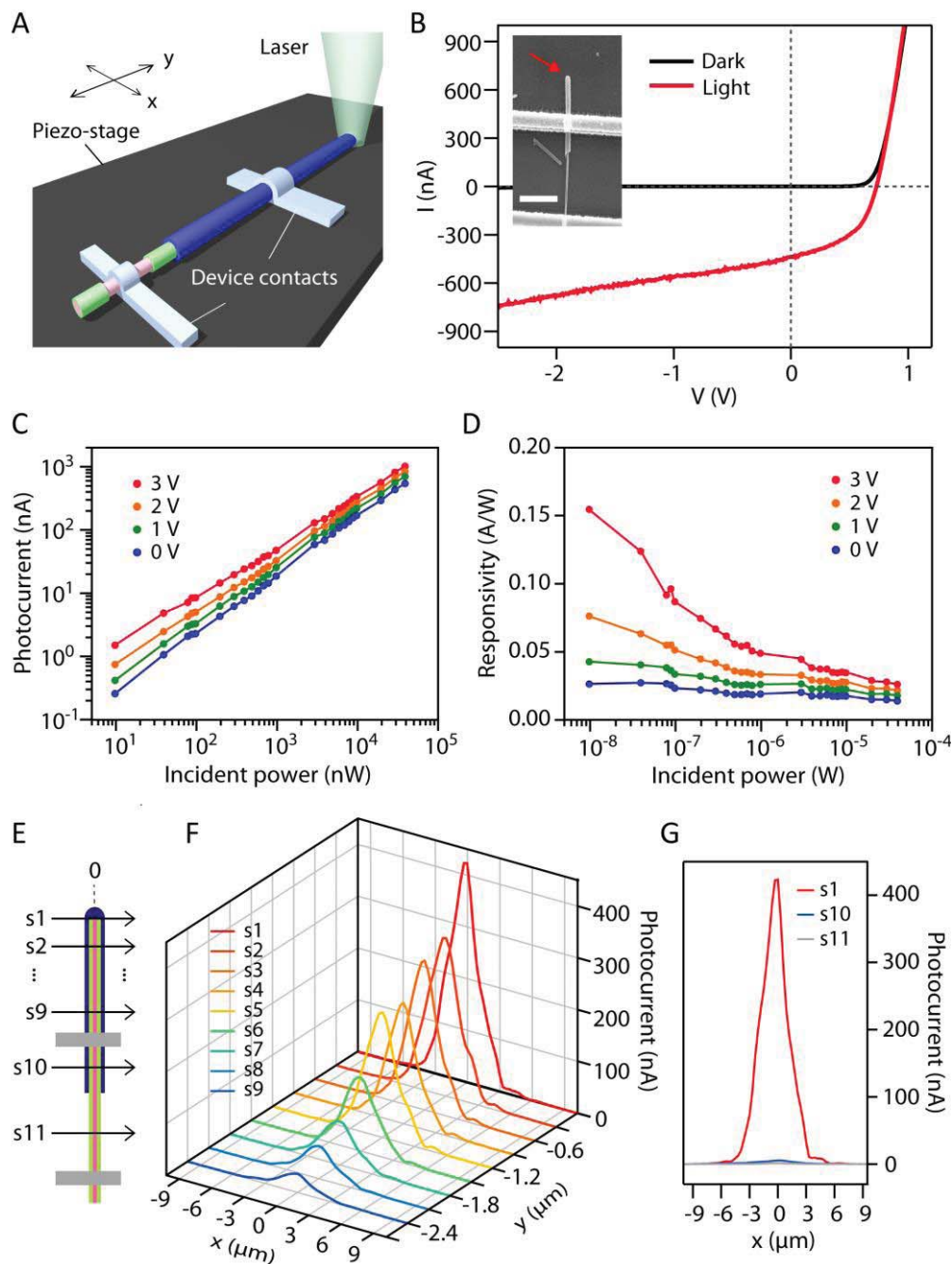


**Figure 5.7 Optical characterizations of a tip-modulated nanowire device.** (A) Schematic illustration of the tip-modulated nanowire device with the tip Si p-n junction mounted on a piezo-controlled movable stage with the laser focused on the device (wavelength 488 nm, spot

**Figure 5.7 (Continued):** size  $\sim 1.6 \mu\text{m}$ ). **(B)** Dark and light I-V curves of the tip-modulated nanowire device with the laser spot focused on the nanowire tip. The incident laser power on the nanowire was  $\sim 29.3 \mu\text{W}$ . Inset, SEM image of the device with the tip p-n junction specified by the red arrow. Scale bar,  $2 \mu\text{m}$ . **(C)** Measured photocurrent as a function of incident power at reverse bias voltages of 0 V (blue), 1 V (green), 2 V (orange), and 3 V (red). **(D)** Measured device responsivity as a function of incident power at reverse bias voltages of 0 V (blue), 1 V (green), 2 V (orange), and 3 V (red). **(E, F, G)** Spatially-resolved photocurrent measurements. **(E)** Schematic illustration of the multiple line-scans in the x-direction carried out at different crossing points of the nanowire (s1-s11): (s1) line-scan through the nanowire tip; (s2-s9): line-scans through the core/shell section with 300 nm increments from the tip along the nanowire axis (y-direction); (s10) line-scan through the core/shell section between the core/shell contacts ( $4.2 \mu\text{m}$  in the y-direction from the tip); (s11) line-scan through the core-only section between the core/shell contacts ( $6.6 \mu\text{m}$  in the y-direction from the tip). **(F)** Measured scanning photocurrents near nanowire tip (s1-s9). The nanowire tip is defined as the origin of the x and y coordinates. **(G)** Measured scanning photocurrents through the tip (s1), the core/shell (s10) and core-only (s11) sections between the core/shell contacts. The incident power was  $\sim 29.3 \mu\text{W}$  for all the line-scans.

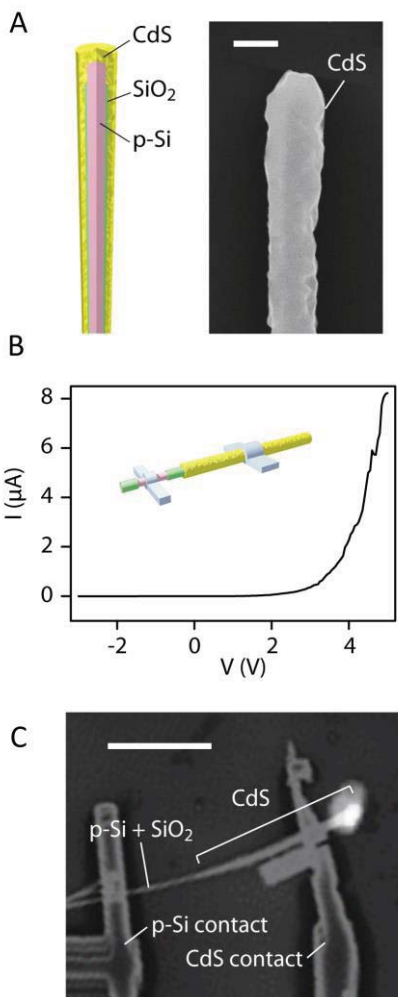


**Figure 5.8 Localized light emission in tip-modulated nanowires with a tip p-Si/CdS heterojunction.** (A) Synthesis of p-Si/CdS heterojunction tip-modulated nanowires. Left: schematic illustration of a tip-modulated nanowire with a tip p-Si/CdS heterojunction. Right: SEM image of a tip-modulated nanowire with the p-Si/CdS heterojunction transferred to SiNx substrate. Scale bar, 500 nm. (B) I-V curves of a p-Si/CdS heterojunction tip-modulated nanowire device. Inset: schematic illustration of the device structure. (C) Overlay of SEM and electroluminescence images of the p-Si/CdS heterojunction tip-modulated nanowire device. Localized light emission was observed from near the tip p-Si/CdS heterojunction. Injected current was  $\sim 7 \mu\text{A}$ . Scale bar, 5  $\mu\text{m}$ .

As described earlier, a tip-modulated nanowire with a tip p-Si/CdS heterojunction (p-type Si core, SiO<sub>2</sub> insulation layer and CdS shell) can be rationally synthesized (**Fig. 5.8A**). First, the p-type Si cores were synthesized following the same epitaxial growth conditions as mentioned previously. Instead of an n-Si shell, a conformal CdS shell was grown in a three-zone furnace with physical vapor deposition (PVD) after the deposition of SiO<sub>2</sub> and removal of the nanowire tip. To explore optical properties of the p-Si/CdS tip-modulated nanowires, independent core and shell contacts were defined to fabricate the p-Si/CdS heterojunction tip-modulated nanowire device after the partial etching of the CdS shell toward the base end. The I-V curve of the device shows a diode-behavior, consistent with the formation of a Si/CdS junction at the nanowire tip (**Fig. 5.8B**). Furthermore, with pulsed current injection to the nanowire core and shell, we observed and recorded electroluminescence image of the device (**Fig. 5.8C**). The light emission from the device was localized toward the nanowire tip, suggesting that the electron-hole recombination is more likely to occur near the tip heterojunction.

#### **5.3.4 Top-down synthesis and vertical nanowire sensor arrays**

Lastly, we explored a top-down approach to synthesize vertical arrays of tip-modulated nanowires to scale up synthesis and fabrication (**Fig. 5.9A**). The tip-modulated nanowire array synthesis starts with definition of arrayed masks, which were patterned by EBL or photolithography on a highly doped p-Si wafer. For this step, other nanopatterning techniques such as colloidal lithography and roll-to-roll nanoimprint lithography can be used alternatively for further low-cost and high-yield scale-up (26). Next, vertical nanowire arrays were formed via

deep reactive ion etching (**Fig. 5.9A, I**) and were subsequently wet-etched in KOH aqueous solution to reduce the diameter (**Fig. 5.9A, II**). After conformal deposition of SiO<sub>2</sub> on the nanowire array by ALD (**Fig. 5.9A, III**), tips of the nanowire arrays were removed, similar to the bottom-up synthesis. Finally, the highly doped n-Si shell was deposited in CVD to yield the vertical tip-modulated nanowire arrays (**Fig. 5.9A, IV**). We note that a synthetic yield close to 80% was achieved with only nanowires longer than 10  $\mu\text{m}$  being counted (**Fig. 5.9B**). Additionally, the as-synthesized nanowire arrays can be easily patterned by shear-transfer, contact-printing (27) and nanocombing (28) to a planar substrate.

The tip-modulated nanowire device array was fabricated by defining contacts to the p-Si substrate and the n-Si shell. To measure the collective transconductance of the nanowire device array, we performed the water-gate experiment by using the electrolyte as the top-gate, similar to the single device measurement (**Fig. 5.9C**). The collective transconductance of 132.3 nS/V shows the arrayed device can also function as a potentiometric sensor. In addition, to further exploit the unique three-dimensional geometry of our device array, we carried out a proof-of-concept sensing measurements with agarose gels of different pHs serving as the top-gate (**Fig. 5.9D**). When the gels were gently placed on top of the tip-modulated nanowire device array, the device conductance showed clear baseline changes, of which the value depends on the pH of the gel. The device sensitivity, calibrated by the device transconductance, was measured  $\sim 58$  mV/pH, which is comparable to the best sensitivity reported for nanowire FET devices (6). This result suggests our nanowire device array can protrude into soft materials and serve as a highly-sensitive potentiometric and chemical sensor.

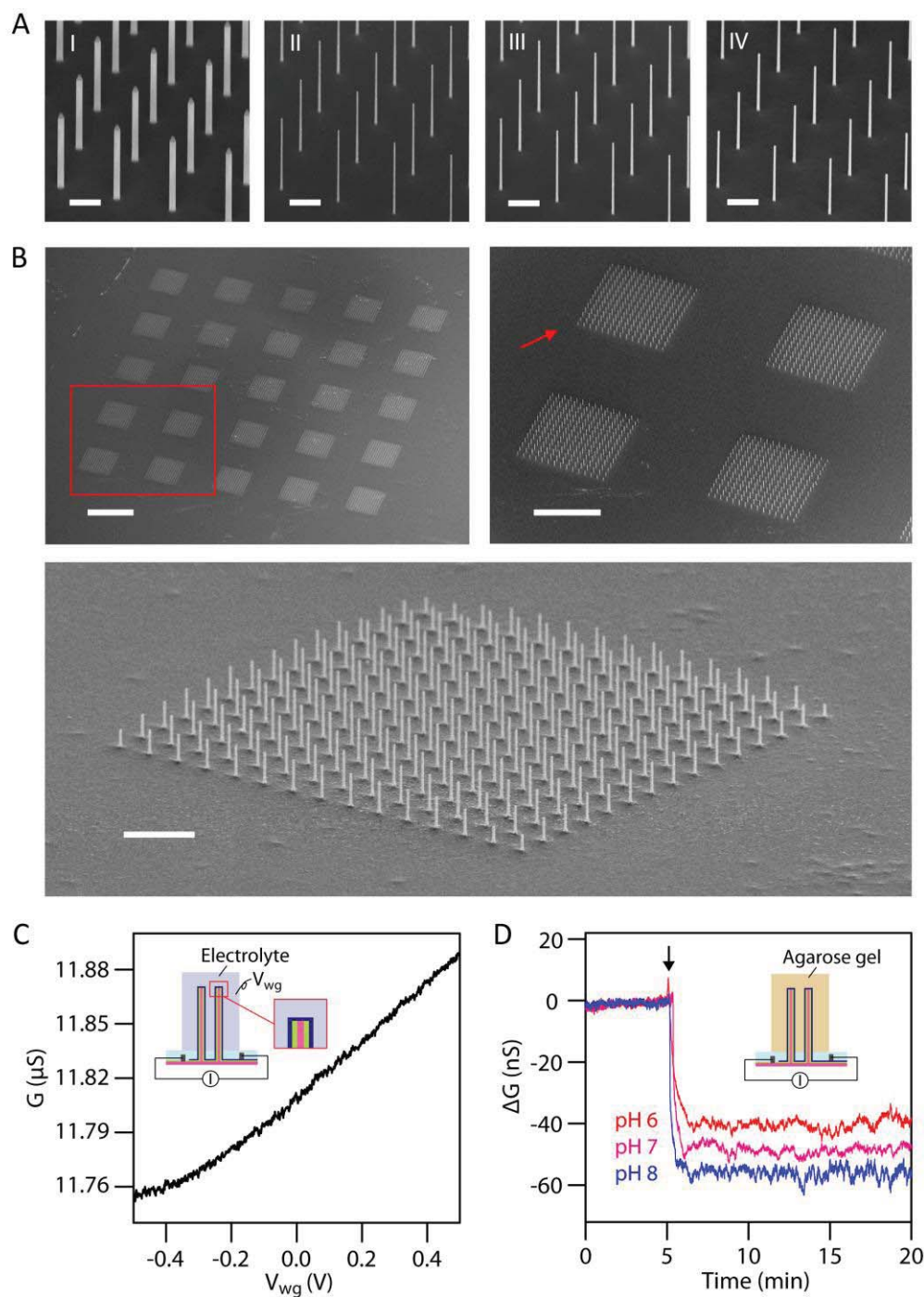


**Figure 5.9 Top-down synthesis and fabrication of vertical tip-modulated nanowires and nanowire device arrays. (A)** Top-down synthesis of tip-modulated nanowire arrays: (I) DRIE of p-Si <111> wafer; (II) KOH wet etching to thin down p-Si nanowire arrays; (III) conformal



**Figure 5.9 (Continued):** deposition of SiO<sub>2</sub> insulation layer by ALD; (IV) removal of the tip and conformal n-Si shell growth in CVD. Scale bars, 5  $\mu$ m. **(B)** SEM images of as-synthesized tip-modulated nanowire arrays. Top left: low magnification SEM image (45 degree tilt) of 25 tiles of 15  $\times$  15 tip-modulated nanowire arrays. Scale bar, 200  $\mu$ m. Top right, high magnification SEM image of the nanowire tiles in the red box. Scale bar, 100  $\mu$ m. Bottom, high-angle SEM image (70 degree tilt) of a 15  $\times$  15 nanowire tile (view angle specified by the red arrow). Scale bar, 20  $\mu$ m. **(C)** Measured water-gate response of 70 vertical tip-modulated nanowires (0.7 V forward bias). Inset, schematic illustration of the vertical tip-modulated nanowire device array structure and the water-gate measurement setup. The p-type Si wafer, SiO<sub>2</sub> layer, n-Si shell, passivation layer are specified by pink, green, blue and light blue, respectively. **(D)** Measured conductance changes of 70 vertical tip-modulated nanowires (0.7 V forward bias) when agarose gels of pH 6 (red), 7 (purple) and 8 (blue) were placed on the nanowire array. The gel placement is specified by the black arrow. Inset, schematic illustration of the gel pH sensing measurement setup with the gel on the nanowire array.

## 5.4 Conclusion and outlook

In this chapter, we demonstrated the design principle, synthetic strategy and device fabrication of a novel nanowire structural motif, termed tip-modulated nanowires. The new nanowire structure can be further generalized to combinations of different materials for the core, the shell and the insulation layer. For example, similar to the tip Si p-n junction, a Si p-i-p junction can be formed at the tip to function as a nanoFET device. Semiconductor heterojunctions, such as Si/III-V (29, 30) and Si/II-VI junctions can be encoded at the nanowire tip as localized LED devices. In addition, Ge/Si (31) and GaAs/AlGaAs (32) junctions can be formed to encode an Esaki diode or a quantum dot for quantum electronics and photonics applications. The vertical tip-modulated nanowire device array also provides a platform for chemical and biological sensing *in vitro* or *in vivo*, allowing large-scale and multiplexed detection of electrical and chemical potentials at the nanowire array tips. We believe that our novel nanowire and device structures will open up promising applications in nanoelectronics, optoelectronics, as well as chemical and biological sciences.

## 5.5 Bibliography

1. C. M. Lieber, Semiconductor nanowires: A platform for nanoscience and nanotechnology. *MRS Bulletin* **36**, 1052-1063 (2011).
2. M. S. Gudiksen, L. J. Lauhon, J. Wang, D. C. Smith, C. M. Lieber, Growth of nanowire superlattice structures for nanoscale photonics and electronics. *Nature* **415**, 617-620 (2002).
3. M. T. Bjork, B. J. Ohlsson, T. Sass, A. I. Persson, C. Thelander, M. H. Magnusson, K. Deppert, L. R. Wallenberg, L. Samuelson, One-dimensional heterostructures in semiconductor nanowhiskers. *Applied Physics Letters* **80**, 1058-1060 (2002).
4. L. J. Lauhon, M. S. Gudiksen, C. L. Wang, C. M. Lieber, Epitaxial core-shell and core-multishell nanowire heterostructures. *Nature* **420**, 57-61 (2002).
5. B. Z. Tian, P. Xie, T. J. Kempa, D. C. Bell, C. M. Lieber, Single-crystalline kinked semiconductor nanowire superstructures. *Nat. Nanotechnol.* **4**, 824-829 (2009).
6. B. Z. Tian, T. Cohen-Karni, Q. Qing, X. J. Duan, P. Xie, C. M. Lieber, Three-dimensional, flexible nanoscale field-effect transistors as localized bioprobes. *Science* **329**, 830-834 (2010).
7. X. J. Duan, R. X. Gao, P. Xie, T. Cohen-Karni, Q. Qing, H. S. Choe, B. Z. Tian, X. C. Jiang, C. M. Lieber, Intracellular recordings of action potentials by an extracellular nanoscale field-effect transistor. *Nat. Nanotechnol.* **7**, 174-179 (2012).
8. R. Gao, S. Strehle, B. Tian, T. Cohen-Karni, P. Xie, X. Duan, Q. Qing, C. M. Lieber, Outside looking in: Nanotube transistor intracellular sensors. *Nano Lett.* **12**, 3329-3333 (2012).
9. Q. Qing, Z. Jiang, L. Xu, R. X. Gao, L. Q. Mai, C. M. Lieber, Free-standing kinked nanowire transistor probes for targeted intracellular recording in three dimensions. *Nat. Nanotechnol.* **9**, 142-147 (2014).
10. B. Z. Tian, X. L. Zheng, T. J. Kempa, Y. Fang, N. F. Yu, G. H. Yu, J. L. Huang, C. M. Lieber, Coaxial silicon nanowires as solar cells and nanoelectronic power sources. *Nature* **449**, 885-U888 (2007).
11. L. Cao, J. S. White, J. S. Park, J. A. Schuller, B. M. Clemens, M. L. Brongersma, Engineering light absorption in semiconductor nanowire devices. *Nat Mater* **8**, 643-647 (2009).

12. T. J. Kempa, J. F. Cahoon, S. K. Kim, R. W. Day, D. C. Bell, H. G. Park, C. M. Lieber, Coaxial multishell nanowires with high-quality electronic interfaces and tunable optical cavities for ultrathin photovoltaics. *Proc. Natl. Acad. Sci. U.S.A.* **109**, 1407-1412 (2012).
13. S. K. Kim, R. W. Day, J. F. Cahoon, T. J. Kempa, K. D. Song, H. G. Park, C. M. Lieber, Tuning light absorption in core/shell silicon nanowire photovoltaic devices through morphological design. *Nano Lett.* **12**, 4971-4976 (2012).
14. J. Wallentin, N. Anttu, D. Asoli, M. Huffman, I. Aberg, M. H. Magnusson, G. Siefer, P. Fuss-Kailuweit, F. Dimroth, B. Witzigmann, H. Q. Xu, L. Samuelson, K. Deppert, M. T. Borgstrom, Inp nanowire array solar cells achieving 13.8% efficiency by exceeding the ray optics limit. *Science* **339**, 1057-1060 (2013).
15. P. Krogstrup, H. I. Jorgensen, M. Heiss, O. Demichel, J. V. Holm, M. Aagesen, J. Nygard, A. Fontcuberta i Morral, Single-nanowire solar cells beyond the shockley-queisser limit. *Nat. Photon.* **7**, 306-310 (2013).
16. V. Mourik, K. Zuo, S. M. Frolov, S. R. Plissard, E. P. A. M. Bakkers, L. P. Kouwenhoven, Signatures of majorana fermions in hybrid superconductor-semiconductor nanowire devices. *Science* **336**, 1003-1007 (2012).
17. K. Storm, F. Halvardsson, M. Heurlin, D. Lindgren, A. Gustafsson, P. M. Wu, B. Monemar, L. Samuelson, Spatially resolved hall effect measurement in a single semiconductor nanowire. *Nat. Nanotechnol.* **7**, 718-722 (2012).
18. K. Tomioka, M. Yoshimura, T. Fukui, A iii-v nanowire channel on silicon for high-performance vertical transistors. *Nature* **488**, 189-193 (2012).
19. R. S. Wagner, W. C. Ellis, Vapor-liquid-solid mechanism of single crystal growth ( new method growth catalysis from impurity whisker epitaxial + large crystals si e ). *Appl. Phys. Lett.* **4**, 89-90 (1964).
20. H. Schmid, M. T. Bjork, J. Knoch, H. Riel, W. Riess, P. Rice, T. Topuria, Patterned epitaxial vapor-liquid-solid growth of silicon nanowires on si(111) using silane. *J. Appl. Phys.* **103**, 024304 (2008).
21. J. H. Woodruff, J. B. Ratchford, I. A. Goldthorpe, P. C. McIntyre, C. E. D. Chidsey, Vertically oriented germanium nanowires grown from gold colloids on silicon substrates and subsequent gold removal. *Nano Letters* **7**, 1637-1642 (2007).
22. K. R. Williams, K. Gupta, M. Wasilik, Etch rates for micromachining processing - part ii. *J. Microelectromech. Syst.* **12**, 761-778 (2003).
23. T. J. Kempa, B. Z. Tian, D. R. Kim, J. S. Hu, X. L. Zheng, C. M. Lieber, Single and tandem axial p-i-n nanowire photovoltaic devices. *Nano Lett.* **8**, 3456-3460 (2008).

24. Z. Jiang, Q. Qing, P. Xie, R. X. Gao, C. M. Lieber, Kinked p-n junction nanowire probes for high spatial resolution sensing and intracellular recording. *Nano Lett.* **12**, 1711-1716 (2012).
25. C. Yang, C. J. Barrelet, F. Capasso, C. M. Lieber, Single p-type/intrinsic/n-type silicon nanowires as nanoscale avalanche photodetectors. *Nano Lett.* **6**, 2929-2934 (2006).
26. M. L. Brongersma, Y. Cui, S. H. Fan, Light management for photovoltaics using high-index nanostructures. *Nature Materials* **13**, 451-460 (2014).
27. A. Javey, S. Nam, R. S. Friedman, H. Yan, C. M. Lieber, Layer-by-layer assembly of nanowires for three-dimensional, multifunctional electronics. *Nano Letters* **7**, 773-777 (2007).
28. J. Yao, H. Yan, C. M. Lieber, A nanoscale combing technique for the large-scale assembly of highly aligned nanowires. *Nat. Nanotechnol.* **8**, 329-335 (2013).
29. M. Hocevar, G. Immink, M. Verheijen, N. Akopian, V. Zwiller, L. Kouwenhoven, E. Bakkers, Growth and optical properties of axial hybrid iii-v/silicon nanowires. *Nat. Commun.* **3**, 1266 (2012).
30. D. B. Turner-Evans, C. T. Chen, H. Emmer, W. E. McMahon, H. A. Atwater, Optoelectronic analysis of multijunction wire array solar cells. *J. Appl. Phys.* **114**, 014501 (2013).
31. L. Chen, W. Y. Fung, W. Lu, Vertical nanowire heterojunction devices based on a clean si/ge interface. *Nano Letters* **13**, 5521-5527 (2013).
32. M. Heiss, Y. Fontana, A. Gustafsson, G. Wust, C. Magen, D. D. O'Regan, J. W. Luo, B. Ketterer, S. Conesa-Boj, A. V. Kuhlmann, J. Houel, E. Russo-Averchi, J. R. Morante, M. Cantoni, N. Marzari, J. Arbiol, A. Zunger, R. J. Warburton, A. F. I. Morral, Self-assembled quantum dots in a nanowire system for quantum photonics. *Nat. Mater.* **12**, 439-444 (2013).

## **Part III Nanowire structures for free-standing nanodevices**

### **Chapter 6 Multi-terminal nanowire structures for self-powered, free-standing nanodevices**

#### **6.1 Introduction**

In this chapter, I would like to introduce a novel free-standing and self-sustained nanodevice structure based on semiconductor nanowires. Self-sustained nanodevices, or “nanorobots” have been the long pursuit of scientists and engineers for various applications. With their nanoscopic sizes, nanodevices can, for example, flow in the blood stream and release loaded drugs at certain regions (1). Moreover, with their unique electrical and optical properties, self-powered and self-controlled nanorobots can help to detect, for example, the existence of cancerous cells (2, 3).

There have been reports on synthesis of “nanorobots” based on DNA origami for drug delivery (4). Also, there have been reports on bottom-up assembly of nanodots and nanorods for nanocatalysis (5). A top-down approach of shrinking the substrate size of a free-standing nanocircuit so that it can be uptaken by cells via endocytosis has been previously reported (6). Although these works remain as the pioneers of the field, the potential for complex and highly-integrated nanorobots remain unexplored due to (1) limited optical and electrical properties of nanomaterials and (2) limited structural variations and difficulty in rational synthesis of complicated nanostructures.

We have learned so far that various device functionalities can be localized in the nanowires or near the nanowire tips of nanowires: potentiometers (FETs), photodetectors (7), solar cells (8), and LEDs (9). A natural extension of the conventional single nanowire structure is a network of localized device functionalities connected by the wiring of nanowire structures, which is illustrated in **Fig. 6.1**. In this free-standing nanodevice, nanowires serve multiple functions: (1) localization of device functionalities at the tips and (2) physical and electrical connection between device functionalities.

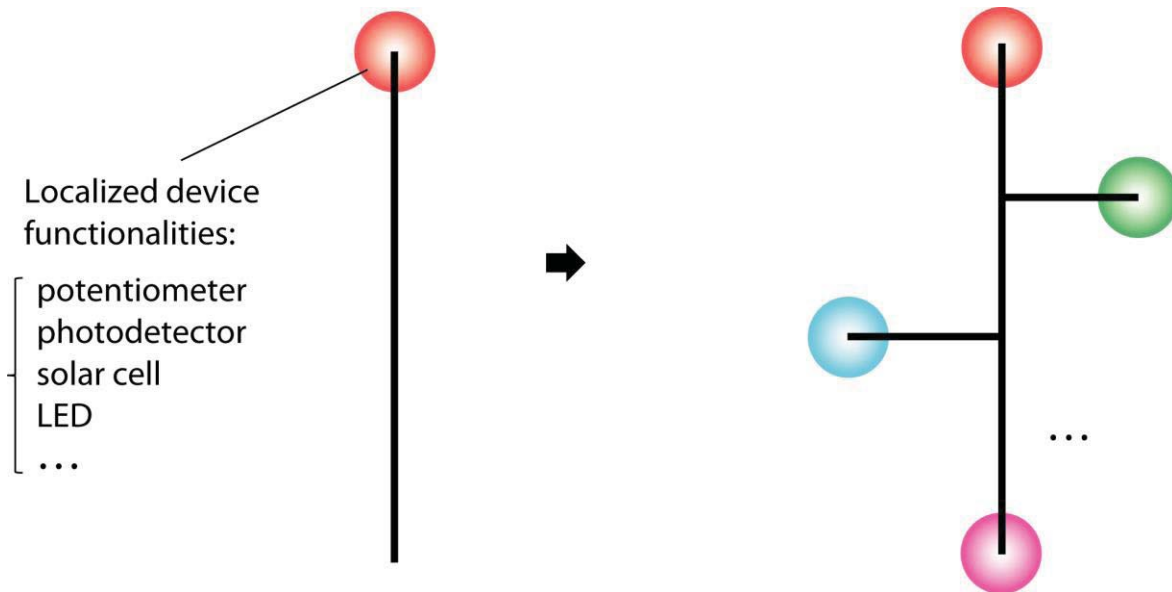


**Figure 6.1 Free-standing, self-powered nanodevices.** Schematic illustration of the concept of free-standing, self-powered nanodevices based on nanowire structures. The nanowire connections between different functionalities can be either planar or three-dimensional.

By combining different types of nanowire structural motifs, we can achieve such a complex structure and function (**Fig. 6.2**). For example, a tip-modulated nanowire structure with two

localized tip-junction, termed two-terminal nanowire, is the simplest free-standing nanowire device. The nanoscale junctions localized at the two ends of the nanowire are electrically connected by the highly doped core and shell. In another example, a combination of branched and tip-modulated nanowire structures can yield a three-terminal device, in which three tip-localized junctions are electrically connected.

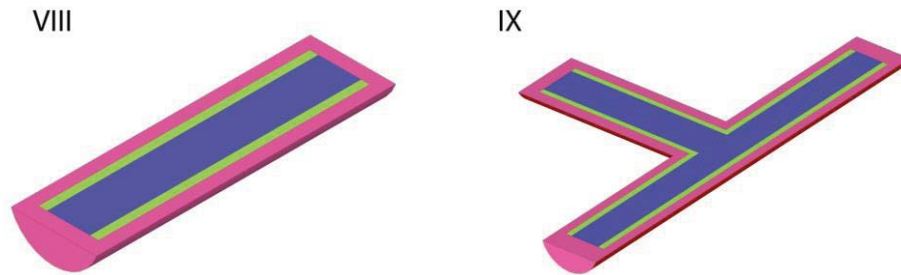


**Figure 6.2 Multi-terminal nanowires for free-standing nanodevices.** (VIII) Two-terminal nanowire structures with localized junctions at both ends. (IX) Three-terminal nanowire structures with localized junctions at the three ends.



## 6.2 Experimental

### 6.2.1 Synthesis of two-terminal nanowires

Rational synthesis of two-terminal nanowires was explored using bottom-up approach based on VLS and conformal shell growth mechanism (**Fig. 6.3**). First, tips of p-Si/SiO<sub>2</sub> core/shell nanowires were mechanically removed similar to the synthetic steps of tip-modulated nanowires. In detail, p-type Si nanowire cores were epitaxially grown by Au nanocluster catalyzed VLS process on Si <111> substrates (p-type, 3-5  $\Omega\cdot\text{cm}$ , Nova Electronic Materials). The VLS growth was carried out with 50 nm Au nanocluster using SiH<sub>4</sub> (1-2 sccm), B<sub>2</sub>H<sub>6</sub> (14 sccm), and H<sub>2</sub> (4-5 sccm) at total pressure and temperature of 10 Torr and 500 °C, respectively. Subsequently, the conformal SiO<sub>2</sub> insulation layer (~50 nm) was deposited with atomic layer deposition (ALD, Savannah-S200, Cambridge NanoTech) at 250 °C. Nanowire tips were then removed by ultrasonication as described in the previous chapter. Following the tip-removal and a brief BHF etch (4s), the nanowires were shear-transferred to two different types of substrates for the shell growth: (1) SiN<sub>x</sub> substrate for on-chip definition of contacts (**Fig. 6.3A**) and (2) periodically patterned SiO<sub>2</sub> substrate for further nanowire transfer (**Fig. 6.3B**). The periodically patterned SiO<sub>2</sub> substrate was fabricated by patterned etching of SiO<sub>2</sub> using SU-8 (2002) as the etch mask and subsequent BHF etching (5 min). Immediately after the shear-transfer of the tip-removed p-Si/SiO<sub>2</sub> core/shell nanowires, the substrate was transferred to the CVD and the n-type Si shell growth was carried out by uncatalyzed deposition using SiH<sub>4</sub> (0.15 sccm), PH<sub>3</sub> (0.3 sccm), and H<sub>2</sub> (60 sccm) at total pressure and temperature of 25 Torr and 775 °C, respectively.

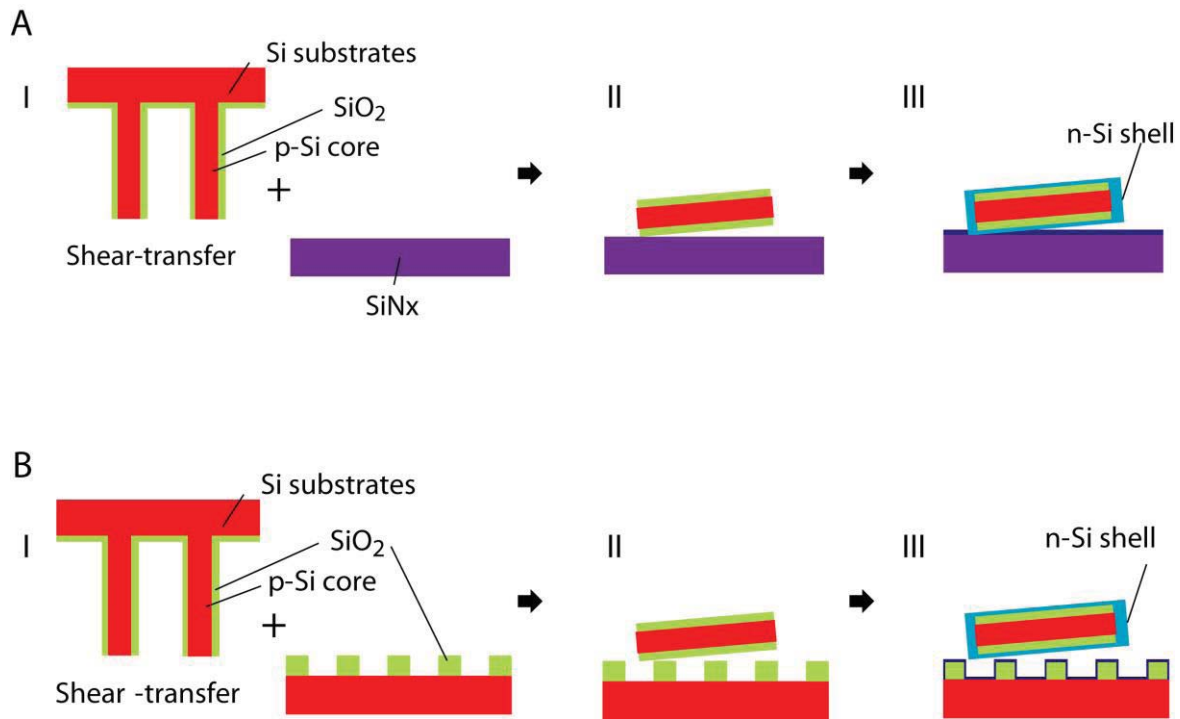


**Figure 6.3 Rational synthesis of two-terminal nanowires.** (A) Synthetic steps of two-terminal nanowire devices on SiNx substrates. (I) Epitaxially grown p-type Si nanowire cores were conformally coated with SiO<sub>2</sub> insulation layer. Similar to synthesis of the tip-modulation nanowire structures, the nanowire tips are removed by ultrasonication. (II) Transfer of nanowires to a SiNx substrate. (III) Conformal growth of n-type Si shell. (B) Synthetic steps of two-terminal nanowire devices on patterned substrates. (I) Epitaxially grown p-type Si nanowire cores were conformally coated with SiO<sub>2</sub> insulation layer. Similar to synthesis of the tip-modulation nanowire structures, the nanowire tips are removed by ultrasonication. (II) Transfer of nanowires to a SiNx substrate. (III) Conformal growth of n-type Si shell. The synthesized nanowires can be further transferred to another substrate.

### 6.2.2 Fabrication of two-terminal nanowire devices

Metal contacts can be defined to the as-synthesized two-terminal nanowires using one of the following fabrication steps: (1) definition of contacts on the growth substrate or (2) transfer of nanowires and the subsequent definition of contacts on a different substrate. For the direct definition of contacts on the growth substrate, SU-8 (2000.5, MicroChem Corp.) etch mask was defined with EBL to protect the shell on both ends of the nanowire. After 6 s etch with BHF to remove the native oxide, the nanowires were etched for 40–60 s with KOH (20 vol.% in water, 60 °C) to remove the n-type Si shell. The SU-8 etch mask was subsequently removed by UV-ozone stripper (300 °C, 40 min). MMA/PMMA resists (MicroChem Corp.) were spin-coated and patterned by EBL for core and shell contacts. The nanowires were etched for 50 s with BHF to remove the SiO<sub>2</sub> layer before thermal evaporation (Ti/Pd, 3/450 nm) to metalize the contacts. For the nanowire transfer and subsequent contact definition, the two-terminal nanowires were synthesized using the periodically patterned SiO<sub>2</sub> substrate. After the n-shell growth, two layers of resist polymers, AZ 4110 and PMMA (C2). Microchem, Corp.) were spin-coated and baked (10). After etching in HF solution for 2 min, resist flakes containing the two-terminal nanowires were detached from the substrate, and transferred to a SiNx substrate (100 nm thermal SiO<sub>2</sub>, 200 nm SiNx, n-type, 0.005 V·cm, Nova Electronic Materials). The resist flakes were then dissolved by acetone and cleaned with oxygen-plasma stripper to attach the nanowires to the SiNx substrate.

### 6.2.3 Electrical and optical characterizations of two-terminal nanowire devices

Electrical and optical characterizations of the two-terminal nanowire devices were carried out following similar procedures of the tip-modulated nanowire devices. I-V characteristics of the two-terminal nanowire devices were measured with a probe station (TTP-4, Desert Cryogenics) and a DAC card (PCI-6030E, National Instruments, Inc.) under computer controls and with a semiconductor parameter analyzer (4156 C, Agilent Technologies). Water-gate experiments were carried out with devices submerged in  $1\times$  PBS solution with a Ag/AgCl reference electrode to apply gate voltage ( $V_{wg}$ ). The two-terminal nanowire devices were passivated with PMMA resists (950 C5, 2 layers, MicroChem Corp.). The source-drain current of the device was amplified by a current preamplifier (1211, DL Instruments) at sensitivity of  $10^{-6}$  or  $10^{-7}$  A/V, filtered (60 kHz, CyberAmp 380, Molecular Devices, Inc.), and digitized at 250 kHz sampling rate (Axon Digidata 1440A Data Acquisition System, Molecular Devices, Inc.).

For the self-powered single-nanowire chemical sensor experiment, a two-terminal nanowire device was mounted on a piezo-controlled movable stage (Digital PI PZT flexure stage) to spatially control the nanowire tip position. One end of the device was optically pumped at room temperature by a 488 nm Ar-ion CW laser, which was focused to a spot of  $\sim 1.6\ \mu\text{m}$  in diameter using a  $\times 40$  microscope objective lens with a numerical aperture (N.A.) of 0.65. The photocurrent was amplified by a current preamplifier (1211, DL Instruments) at sensitivity of  $10^{-6}$  or  $10^{-7}$  A/V and digitized at 250 kHz sampling rate as a function of time.

## 6.3 Results and discussion

### 6.3.1 Nanowire synthesis and material characterizations

Each synthetic step of two-terminal nanowires was characterized by SEM (**Fig. 6.4**). After the transfer to the SiNx substrate and the subsequent shell growth, a conformal shell around both nanowire ends was observed. In the other synthetic route using the patterned SiO<sub>2</sub> substrate, most of the transferred nanowires stayed on the top of the trenches and similarly had both ends coated with the shell. SEM characterization of the two-terminal nanowires transferred from the patterned substrate showed successfully transfer of two-terminal nanowires without significant breaking. However, we also note that a fraction of the transferred nanowires were broken or had peeled off shells around the regions that were in touch with the trenches.

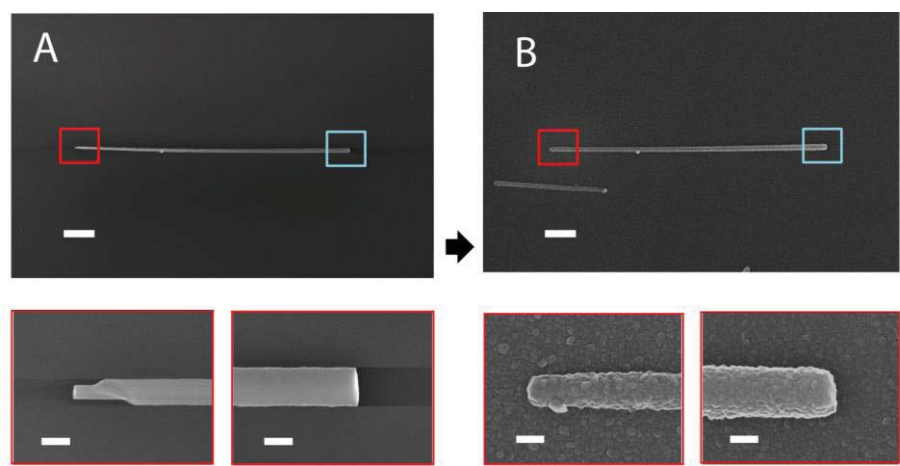


**Figure 6.4** Synthesis and SEM characterizations of two-terminal nanowires. (A) SEM images of a transferred nanowire with the conformal SiO<sub>2</sub> insulation layer (removed at both ends) to a SiNx substrate. Scale bars, 2  $\mu\text{m}$  (top) and 200 nm (bottom). (B) SEM images of the two-terminal nanowire after growth of n-type Si shell. Scale bars, 2  $\mu\text{m}$  (top) and 200 nm (bottom).

### 6.3.2 Electrical and optical properties of two-terminal nanowire devices

I-V characterization of a two-terminal nanowire device with one core contact and two shell contacts (fabricated by process shown in **Fig. 6.3A**) showed diode I-V behavior for both the tip devices (**Fig. 6.5A-C**). In a different device geometry, one core contact and one shell contact were defined to a two-terminal nanowire using a thin SU-8 spacer ( $\sim 170$  nm) to insulate the core contact from the half-etched nanowire shell (about  $\sim 130$  nm high from the substrate). The half-etched device showed diode I-V behavior with higher conductance, consistent with the I-V characteristics of two tip p-n junctions connected in parallel (**Fig. 6.5D and E**). Finally, I-V characterization of a two-terminal nanowire device fabricated on the receiving substrate for the transferred nanowire (fabricated by process shown in **Fig. 6.3B**) also showed diode I-V behavior for both the tip devices (**Fig. 6.5F and G**). In summary, I-V measurements show that the two-terminal nanowires have p-n junctions localized at both tips of the nanowires, which is distinct from the I-V characteristics of tip-modulated nanowire structures in which only a single tip has the p-n junction (**Fig. 5.5B**).

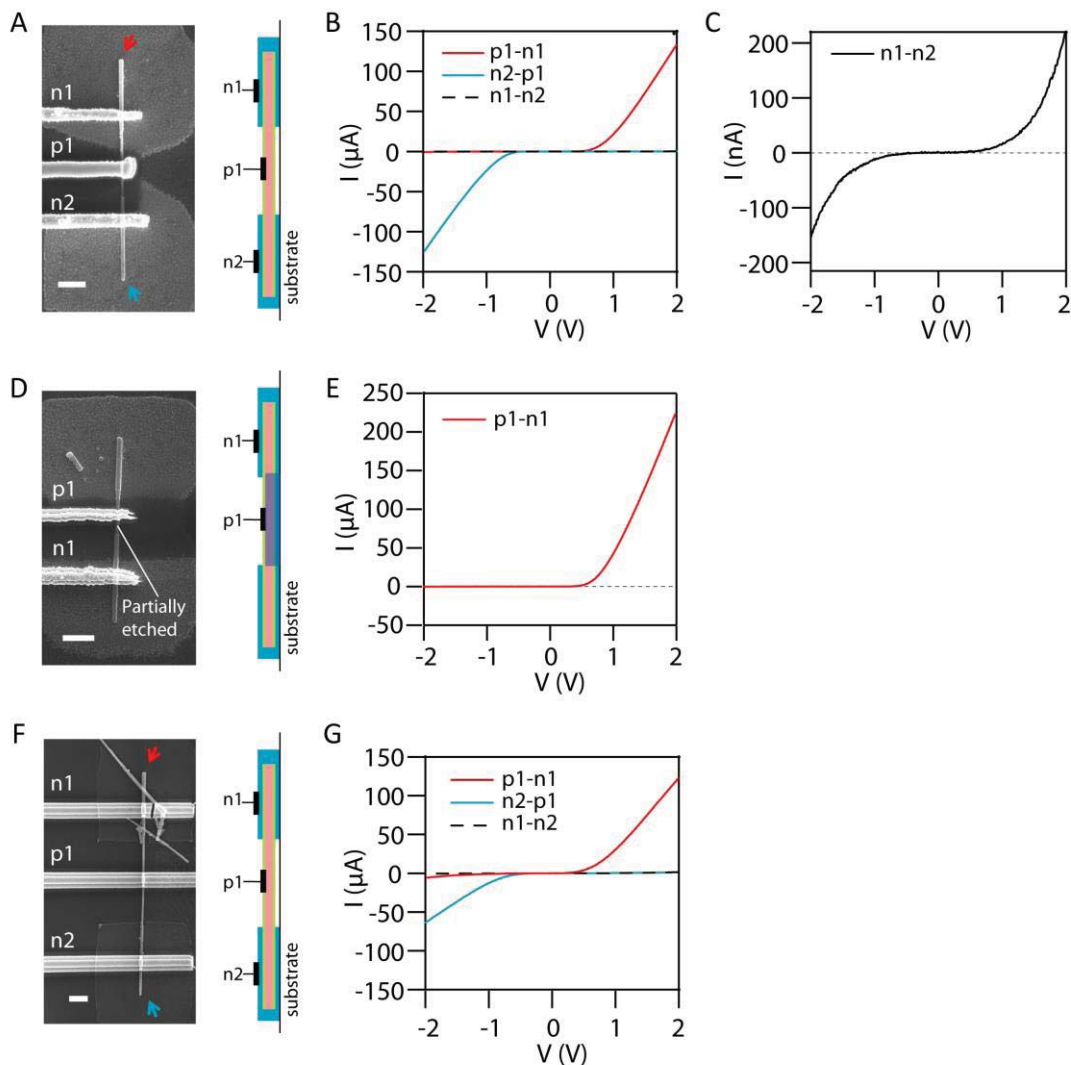


**Figure 6.5 Electrical characterizations of two-terminal nanowires.** (A-E) Two-terminal nanowire devices defined directly on the SiN<sub>x</sub> substrate after the shell growth. (A) SEM image of a two-terminal nanowire device with one core contact (p1) and two shell contacts (n1 and n2). The nanowire shell is fully removed near the core contact region of the nanowire. Scale bar, 2  $\mu\text{m}$ . (B) I-V curves measured between the p1-n1, p1-n2 and n1-n2 contacts. (C) An enlarged plot of the I-V curve for device n1-n2. (D) SEM image of a two-terminal nanowire device with one core contact (p1) and one shell contact (n1). The upper half of the nanowire shell is removed near the core contact region by masking the nanowire with a  $\sim 130$  nm thick SU-8 resist mask

**Figure 6.5 (Continued):** and the subsequent KOH etching. The core contact was then defined on a  $\sim 170$  nm thick SU-8 spacer to avoid contact with the half-cut shell. Scale bar, 2  $\mu\text{m}$ . **(E)** I-V curve measured between the core and shell contacts (p1-n1). **(F-G)** Two-terminal nanowire device defined on the receiving SiNx substrate for the transferred nanowire. **(F)** SEM image of a two-terminal nanowire device with one core contact (p1) and two shell contacts (n1 and n2). The nanowire shell is fully removed near the core contact region of the nanowire. Scale bar, 2  $\mu\text{m}$ . **(G)** I-V curves measured between the p1-n1, p1-n2 and n1-n2 contacts.

The two-terminal nanowire can function as a self-powered single-nanowire chemical sensor. When a core contact and a single shell contact is defined on the nanowire (with the middle shell section only half-etched and thus physically and electrically connecting shells at both ends), both tips of the two-terminal device, forming a p-n junction diode, can function as, for example, a potentiometer or a solar cell. We used a focused laser spot with constant power to pump one tip of the nanowire to generate photocurrent and observed the change of the output voltage (the voltage between the two contacts) while chemically gating the other tip of the nanowire by changing the pH of the solution (**Fig. 6.6A and B**). We note that the nanowire device was fully passivated with resist except for the tip which was used for the chemical sensing. As result, the output voltage showed strong dependence on the pH of the solution, demonstrating that the single nanowire device serves as a single-nanowire self-powered chemical sensor (**Fig. 6.6C**). We note that by tuning the dopant concentration and nanowire dimensions, the device sensitivity can be further improved. In addition, surface modification of the exposed nanowire tip enables detection of other chemical species such as proteins and neurotransmitters.



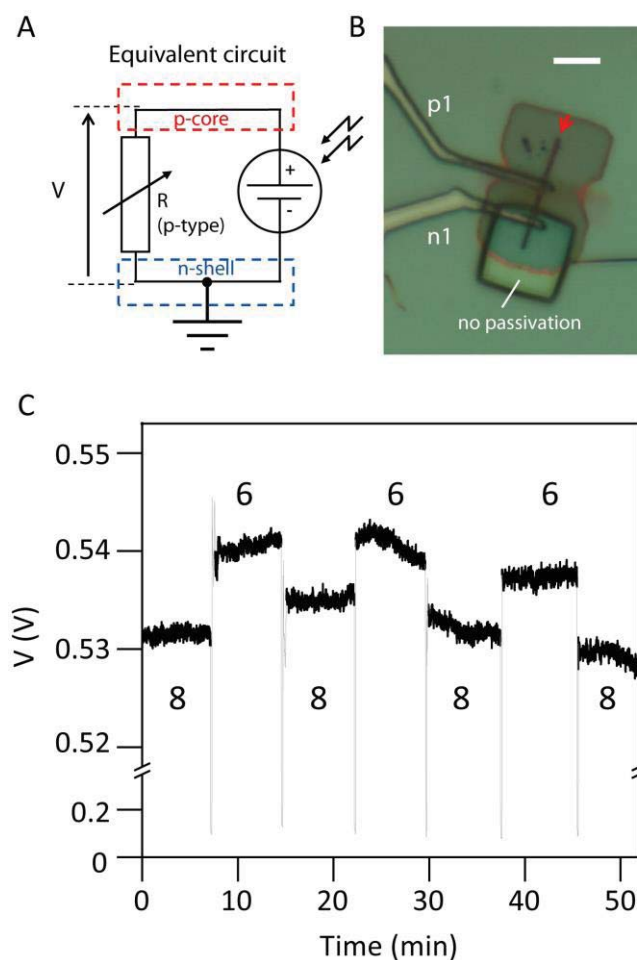


**Figure 6.6 Self-powered single-nanowire chemical sensors.** (A) Equivalent circuit diagram of two-terminal Si p-n junction nanowire device with one tip functioning as the photovoltaic unit and the other tip functioning as a chemical sensor. (B) Optical image of a two-terminal nanowire device with a passivation window. The core and shell contacts are defined to measure the voltage different between the core and the shell ( $V$ ). The exposed tip length is  $3.7\ \mu\text{m}$ . Scale bar,  $5\ \mu\text{m}$ . (C) Change of voltage recorded between the core and shell contacts ( $V$ ) as the pH of the solution was changed between 6 and 8. The photovoltaic end of the device (red arrow in B) was pumped with 488 nm laser spot ( $\sim 90\ \mu\text{W}$  incident power).

## 6.4 Conclusions and outlook

Future work remains to explore rational synthesis of three-terminal nanowires as well as multi-terminal three-dimensional nanowire networks. Further electrical and optical characterizations of different terminal ends and how they affect other terminal ends need to be carried out. In addition, chemical sensing experiments with more complex targets such as neurotransmitters and cancer markers should be carried out with the multi-terminal nanowire devices while optically pumping the power on the other tip. Finally, interfacing with biological cells and tissues, which needs further optimization of the device geometry and advancements in surface modification, remains as the future goal.

## 6.5 Bibliography

1. S. Ganta, H. Devalapally, A. Shahiwala, M. Amiji, A review of stimuli-responsive nanocarriers for drug and gene delivery. *J. Control. Release* **126**, 187-204 (2008).
2. S. J. Park, S.-H. Park, S. Cho, D.-M. Kim, Y. Lee, S. Y. Ko, Y. Hong, H. E. Choy, J.-J. Min, J.-O. Park, S. Park, New paradigm for tumor theranostic methodology using bacteria-based microrobot. *Sci. Rep.* **3** (2013).
3. Y. Li, T. Y. Lin, Y. Luo, Q. Liu, W. Xiao, W. Guo, D. Lac, H. Zhang, C. Feng, S. Wachsmann-Hogiu, J. H. Walton, S. R. Cherry, D. J. Rowland, D. Kukis, C. Pan, K. S. Lam, A smart and versatile theranostic nanomedicine platform based on nanoporphyrin. *Nat. Commun.* **5**, 4712 (2014).
4. S. M. Douglas, I. Bachelet, G. M. Church, A logic-gated nanorobot for targeted transport of molecular payloads. *Science* **335**, 831-834 (2012).
5. L. Amirav, A. P. Alivisatos, Photocatalytic hydrogen production with tunable nanorod heterostructures. *J. Phys. Chem. Lett.* **1**, 1051-1054 (2010).
6. R. Gomez-Martinez, P. Vazquez, M. Duch, A. Muriano, D. Pinacho, N. Sanvicens, F. Sanchez-Baeza, P. Boya, E. J. de la Rosa, J. Esteve, T. Suarez, J. A. Plaza, Intracellular silicon chips in living cells. *Small* **6**, 499-502 (2010).
7. C. Yang, C. J. Barrelet, F. Capasso, C. M. Lieber, Single p-type/intrinsic/n-type silicon nanowires as nanoscale avalanche photodetectors. *Nano Lett.* **6**, 2929-2934 (2006).
8. B. Z. Tian, X. L. Zheng, T. J. Kempa, Y. Fang, N. F. Yu, G. H. Yu, J. L. Huang, C. M. Lieber, Coaxial silicon nanowires as solar cells and nanoelectronic power sources. *Nature* **449**, 885-889 (2007).
9. F. Qian, S. Gradečak, Y. Li, C.-Y. Wen, C. M. Lieber, Core/multishell nanowire heterostructures as multicolor, high-efficiency light-emitting diodes. *Nano Lett.* **5**, 2287-2291 (2005).
10. S. Kwangsoo, L. Dong Hyun, Y. Jaeseok, L. Won Woo, P. Won Il, Synthesis and transfer of si nanowire arrays embedded in photo-sensitive polymer films for non-planar electronics. *J. Phys. D: Appl. Phys.* **44**, 015501 (2011).